

**INSTABILITY DRIVEN RECONFIGURABLE SOFT MATERIALS:
MECHANICS AND FUNCTIONALITY**

A Dissertation
Submitted to
the Temple University Graduate Board

In Partial Fulfillment
of the Requirements for the Degree
DOCTOR OF PHILOSOPHY

by
Gaojian Lin
May 2018

Examining Committee Members:

Dr. Jie Yin, Advisory Chair, Mechanical Engineering
Dr. Haijun Liu, Mechanical Engineering
Dr. Harsh Chopra, Mechanical Engineering
Dr. Yugang Sun, Chemistry
Dr. Andrew Spence, External Member, Bioengineering

ABSTRACT

Mechanical instability, a deformation mode involving abrupt switching between two distinct equilibrium structural configurations, has historically been viewed as a failure mechanism in engineering and materials science. Since the pioneering work in harnessing spontaneous buckling for surface micro-patterning in 1998, tremendous research interest has focused to utilize, rather than avoid, buckling instability in soft materials at small scale for achieving unique properties and multifunctionality. The benefit of small-scale buckling instability in soft materials and structures lies in the reversible dynamic tunability of the buckled structural or surface configuration in response to different external stimuli, which enables the coupling of structural or surface reconfiguration with dynamically tunable properties, such as mechanical, optical, wetting, and electrical properties. In this dissertation, I explore the fundamental mechanics and functionality of surface-based buckling and hierarchical wrinkling on substrates in multifunctional opto-electronic devices and smart windows.

I will first explore the benefits of classical plate buckling in soft materials. The challenge lies in the intrinsic indeterminate characteristics of buckling in terms of its buckling orientation, which could lead to geometric frustration and random global structures. To address this challenge, I introduce cuts-based geometrical imperfection to guide the deterministic buckling in arrays of parallel active polymeric plates on rigid substrates. After introducing patterned cuts, the originally random phase-shifted buckling transits to a prescribed buckling with controllable phases. The design principle for cut-directed deterministic buckling in plates is revealed through both mechanics model and

finite element simulation. By harnessing cut-directed buckling for controllable contacts and interactions in buckled parallel plates, I demonstrate the array of parallel plates as a multifunctional platform for selectively steering the electronic and optical pathways on demand, as well as the potential application in design of mechanical logic gates.

I then explore the hierarchical wrinkling of thin films on soft substrates via sequential wrinkling for design of a potential multifunctional smart window with combined structural color and water droplet transport control. The self-similar hierarchical wrinkles with both nanoscale and microscale features are generated on a pre-strained poly(dimethylsiloxane) (PDMS) elastomer through sequential strain release and multi-step oxygen plasma treatment. I exploit the criteria for generating self-similar hierarchical wrinkles through both simplified theoretical model and experiments. I show that the hierarchically wrinkled elastomer displays both opaqueness and iridescent structural color. I further show its ability in control of water droplet transport on demand through mechanical stretching and release.

I further extend the study of self-similar hierarchical wrinkling to the dynamic wetting behavior of multiscale self-similar hierarchical wrinkled surfaces on PDMS substrates through combined plasma and ultraviolet ozone (UVO) treatment. The generated surface structure shows an independently controlled dual-scale roughness with level-1 small-wavelength wrinkles resting on level-2 large-wavelength wrinkles, as well as accompanying orthogonal cracks. By tuning the geometry of hierarchical wrinkles, I explore the small degree of wetting anisotropy in hierarchical wrinkled surfaces, defined as the contact angle difference between the parallel and perpendicular directions to the

wrinkle grooves through both experimental characterization (confocal fluorescence imaging) and theoretical analyses. I find that the measured larger apparent contact angle than the theoretically predicted Wenzel contact angle is attributed to the three-phase contact line pinning effect of both wrinkles and cracks, which generates energetic barriers during the contact line motion. I reveal that the observed small degree of wetting anisotropy in the hierarchical wrinkled surfaces arises from the competition between orthogonal wrinkles and cracks in the contact line pinning.

ACKNOWLEDGMENTS

I would like to express my special appreciation to my advisor Dr. Jie Yin for his continuous guidance and support of my study and research. The passion and enjoyment he showed during the research was contagious and inspiring for me.

I would like to thank the advisory committee members Drs. Haijun Liu, Harsh Chopra, Yugang Sun and Andrew Spence for their helpful advice and willingness to serve on my dissertation advisory committee.

Dozens people have helped me with my research and study at Temple. I truly appreciate Dr. Dmitriy Dikin for his help with SEM throughout my five years of research. I am grateful to Mr. James Gannon and Mr. John Jemison for their assistance in machine shop, to Dr. Joel Sheffield for the assistance with fluorescence confocal imaging and to Dr. Hiromichi Yamamoto for the assistance in Sigh center. I am also grateful to Drs. Dengteng Ge, Gaoxiang Wu and Yu Xia for the help with soft lithography. I would like to thank Dr. Fei Ren and Dr. Shenqiang Ren for their useful suggestions as my dissertation proposal committee. I also appreciate Dr. Shu Yang for generous share of research equipment in her lab at University of Pennsylvania. I would like to thank Dr. Shriram Pillapakkam and Dr. Parsaoran Hutapea for their help as graduate coordinators.

I also wish to express my thanks to my lab members, Yichao and Qiuting, as well as other fellow graduate students Yao, Haoqi and Bosen for their kindness and friendship. I have met some good friends during these 5 years, Ethan, Lirong, Frank, Weiran, Peiyi, Fan and Fengcheng. Without them the time I spent in Philly would not be this much fun.

Most importantly, I would like to thank my dearest parents for supporting me spiritually during tough times in the Ph.D. pursuit. Their love and encouragement have always been important to me.

TABLE OF CONTENTS

ABSTRACT	ii
ACKNOWLEDGMENTS	v
LIST OF FIGURES	x
LIST OF TABLES	xv
CHAPTER 1 INTRODUCTION	1
1.1 Mechanical Instabilities.....	1
1.1.1 Pattern transformation	2
1.1.2 Wrinkling.....	4
1.1.3 Creasing.....	5
1.1.4 Folding.....	6
1.1.5 Delamination	7
1.2 Reconfigurable Soft Materials	8
1.3 Outline of This Thesis	9
CHAPTER 2 CUTS GUIDED DETERMINISTIC BUCKLING IN ARRAYS OF SOFT ACTIVE PARALLEL PLATES FOR MULTIFUNCTIONALITY	11
2.1 Introduction	11
2.2 Cuts Guided Deterministic Buckling	13
2.2.1 Buckling behaviors of discrete thin plates without cuts.....	13
2.2.2 Buckling behaviors of discrete thin plates with cuts	15
2.2.3 Buckling behavior of discrete thin plates with only partially periodic cuts ...	18
2.3 Design of Cuts Guided by Modeling and Simulation	20
2.3.1 Theoretical model of bottom constrained plate	20
2.3.2 FEM simulation	24
2.4 Applications of Cuts Guided Deterministic Buckling.....	28
2.4.1 Switchable electrical conductive pathway.....	28
2.4.2 Mechanical logic gates	32
2.4.3 Switchable optical properties.....	36
2.5 Experimental Methods	40
2.5.1 Fabrication of microstructured hydrogel plates.....	40
2.5.2 Swelling-induced buckling.....	41
2.5.3 Sample characterization.....	41
2.5.4 Activation of the electrical conductive pathways.....	41
2.5.5 Finite element method simulation	42
2.6 Conclusion.....	44

CHAPTER 3 : SELF-SIMILAR HIERARCHICAL WRINKLES AS A POTENTIAL MULTIFUNCTIONAL SMART WINDOW.....	45
3.1 Introduction	45
3.2 Generation of Different Self-similar Hierarchical Wrinkles.....	49
3.3 Tunable Optical Transparency and Non-vanishing Structural Color.....	53
3.4 Modeling and Simulation of Hierarchical Wrinkle Formation and Evolution...	58
3.4.1 FEM simulation	58
3.4.2 Theoretical model	60
3.5 Controllable Water Droplet Transport via Mechanical Strain	63
3.6 Experimental Methods	69
3.6.1 Fabrication of hierarchical surface wrinkling.....	69
3.6.2 Surface topography characterization	70
3.6.3 Optical property characterization	70
3.6.4 Contact angle and sliding angle measurement	70
3.6.5 Finite element method simulation	70
3.7 Conclusion.....	72
CHAPTER 4 SMALL DEGREE OF ANISOTROPIC WETTING ON SELF- SIMILAR HIERARCHICAL WRINKLED SURFACES	73
4.1 Introduction	73
4.2 Experimental Methods	76
4.2.1 Generation of hierarchical wrinkled surfaces.....	76
4.2.2 Surface topography characterization	78
4.2.3 Confocal imaging	79
4.2.4 Contact angle (CA) measurements.....	79
4.3 Tunable Dimensions of Multiscale Hierarchical Wrinkles	80
4.4 Cracks in Hierarchical Wrinkles	84
4.5 Effect of Wrinkles' Dimension on Anisotropic Wetting Behavior.....	87
4.6 Wetting state of hierarchical wrinkles: theoretical and experimental analysis..	91
4.6.1 Thermodynamic model.....	92
4.6.2 Directly observation through confocal imaging	96
4.7 Anisotropic Wetting Behavior: Theoretical and Experimental Analysis.....	97
4.7.1 Failure of Wenzel model	97
4.7.2 Experimental evidence of contact line pinning	100
4.7.3 Thermodynamic model predicting the dynamic contact angles	102
4.8 Calculation of Volume Fraction and Roughness Factor of Cracks.....	108
4.9 Some Remarks on Coexistence of Orthogonal Wrinkles and Cracks.....	109
4.10 Conclusion.....	111

CHAPTER 5 FUTURE WORK	113
5.1 2D Hierarchical Wrinkling Surfaces	113
5.2 Water Condensation on Wrinkling Surfaces	115
5.3 Assembly of Colloidal Particles by Evaporation on Wrinkling Surface with Anisotropic Wettability	121
5.4 Swell Induced Buckling of Top and Bottom Constrained Lattice Structure....	123
REFERENCES.....	125
APPENDIX.....	143

LIST OF FIGURES

Figure 1.1: Mechanical instability with characteristic length. (a) Wrinkling (b) Creasing (c) Folding (d) Delamination	2
Figure 1.2: Pattern transformation of circular holes in square lattice	3
Figure 2.1: Cut-guided reversible peak-valley contacts in 1-D soft reconfigurable mechanical metamaterials via buckling. (a-b) Schematic illustration of a simple metamaterial without cuts (a) and with identical patterned V-shaped cuts (b) (c-d) Left column: tilted view of SEM images of a hydrogel mechanical metamaterial with vertical micro-plates without cuts (c) and with identical patterned V-shaped cuts (d). Each plate has height $H = 60 \mu\text{m}$, thickness $t = 20 \mu\text{m}$, and space between plates $s = 40 \mu\text{m}$. Right column: corresponding top view of optical images of buckled hydrogel mechanical metamaterials after swelling. Insets are the magnified top view of plates with V-shaped cuts before (left) and after buckling (right), showing cuts right locating at wave trough or peak. (e) Schematic illustration of applying opposite orientations of patterned V-cuts to two neighboring plates to enable cut-guided peak-valley contacts after buckling; (f) Left: corresponding top view of optical images of well-controlled peak-valley contacts guided by patterned opposite cuts in a swelling-driven buckled hydrogel mechanical metamaterials over large area; right: magnified optical images showing the occurrence of valley-peak contacts is right at cut locations.	14
Figure 2.2: Demonstration of transition from the disordered buckled configuration to the ordered one in an array of macroscale PDMS plates with bottoms attached to the acrylics sheet upon swelling in hexane. (a) Plates without cuts before deformation (left) and after swelling-induced buckling (right), showing randomly distributed phase angles between plates. (b) Plates with the patterned V-shaped cuts on every plate before deformation (left) and after swelling-induced buckling (right). Cuts are right located at wave troughs or valleys to direct the buckling	15
Figure 2.3: FEM shows the highest contact pressure at the valley-peak contact between two buckled plates without sliding in the post-buckling process.	17
Figure 2.4: Time lapse optical images of the deswelling process of an array of hydrogel micro-plates with patterned cuts upon solvent evaporation, showing the fully reversible contact and dis-contact process despite the adhesion between hydrogel micro-plates when in contact.	18
Figure 2.5: Effect of a single cut (a-b) and partially periodic cuts (c-d) on the buckling of an array of hydrogel micro-plates. (a) and (c): Optical images of arrays of hydrogel plates before swelling. (b) and (d): The corresponding optical images of random phase-shifted buckling (b), as well as a combination of prescribed ordered buckling and phase-shifted buckling (d) after swelling. The cut and non-cut regions are highlighted in green and pink colors to facilitate visualization, respectively.	20
Figure 2.6: Comparison of the theoretically assumed deflection mode with the numerically simulated deflection profile, showing good agreement.....	22
Figure 2.7: Engineering the geometry and patterning of V-cuts to direct the buckling direction right at the cuts in 1-D mechanical metamaterials via predictive mechanics model and FEM simulation. (a-c) Comparison between theoretical models, simulation, and experiments on the critical buckling strain (a), wavelength (b), and amplitude (c) in buckling of a bottom-constrained plate without cuts. (d-f) FEM simulation results on directing the buckling through patterned cuts in plates with $H/t = 4$ by engineering the periodicity of cut patterning l/λ (d), the normalized cut depth d/t (e), and opening angle Θ (f). (f) Also shows the evolution process of representative structural reconfigurations and von	

Mises stress contours in plates with different θ as the swelling ratio increases from 0 to 0.2. Stress unit is in kPa.	25
Figure 2.8: Schematic illustration of beam bending at a triangular cut.	27
Figure 2.9: Zoom-in figure shows the conductive coating and V-shaped cuts on macroscale PDMS plates.	30
Figure 2.10: Demonstration of cuts-guided peak-valley contacts via directional buckling for activating switchable electrical conductive pathways. (a-d) Mechanically activating the Domino-like in-series (a-b) and parallel (c-d) electric circuits via cuts-guided peak-valley contacts driven by buckling of macroscale PDMS plates with conductive coatings. Buckling-induced contacts in plates occur and thus LED lights are on either by transversely stretching (b) or by longitudinally bending (d) the attached substrates. (e) Change of conductance after cycles of stretching-unstretching in (b).....	31
Figure 2.11: Swelling induced activation of the switchable electrical conductive pathway through buckling induced contact in array of PDMS plates coated with black carbon-based black conductive grease without cuts.	31
Figure 2.12: Designs of mechanical logic gate-like switchable conductive pathway via cut-guided directional buckling for functions of AND (a), OR (b), and NOT (c) operations demonstrated in a unit of two parallel bottom constrained plates. The buckled state is “1”, unbuckled state is “0”. The red LED light is on when the output of corresponding logic gate is “1” (“11” for AND, “10, 11” for or, and “0” for NOT).	32
Figure 2.13: FEM simulations of complex conductive pathways with cut-directed controlled contacts via buckling. (a) A hierarchically branched pathway. Top: undeformed configuration. Bottom: buckled and connected configuration. Right: corresponding schematic illustration of a hierarchical branched electrical circuit. (b) Design of a confined polyline conductive pathway connecting vertical, oblique, and horizontal directions embedded in discrete rectangular-centered patterned plates via localized buckling in the highlighted area. Top: undeformed configuration. Bottom: localized buckled configuration shows the generation of polyline conductive pathway.....	35
Figure 2.14: Demonstration of cuts-guided peak-valley contacts via directional buckling for multifunctional reconfigurable 1-D mechanical metamaterials with switchable optical properties. (a-b) Reconfiguration of laser light propagation pathways (a) and optical transparency (b) in the hydrogel mechanical metamaterials same as that in Fig. 1f through swelling-induced buckling. (c-e) Schematic illustration of the processes of “writing”, displaying, and “erasing” patterned conductive pathways such as letters “N” and “S” in a centered rectangular arrangement. Letters are displayed through localized buckling in the selective region. (d-e) Experimental demonstration of “writing” and “erasing” letters “N” and “S” with oblique and curved conductive pathways, respectively. (d) Top-view optical images of the layout of the hydrogel mechanical metamaterial before deformation. Bottom-left inset shows the opposite patterned cuts between two neighboring micro-plates; top-right inset shows the optical image of the transparent hydrogel mechanical metamaterial on a black background. (e) Optical image of interconnected oblique pathway through cuts-guided peak-valley contacts in the oblique segment of letter “N” after localized buckling. Top-right inset shows the appearance of letters of “S” and “N” in millimeter size after localized swelling. Upon water evaporation, the buckled regions return to the original state, thus, erasing the displayed letters.	39
Figure 2.15: Optical images of the reversible buckling of an array of discrete hydrogel micro-plates, leading to the “write” of macroscopic letters upon swelling induced buckling and “erase” of letters upon deswelling.....	40

Figure 3.1: The schematic illustration for the fabrication process of generating hierarchical wrinkles on PDMS through two-step strain release and two-step oxygen plasma treatment.49

Figure 3.2: (a) SEM images of hierarchical wrinkles with different large to small wave number ratios generated on a pre-strained PDMS elastomer ($\varepsilon_{pre}=\varepsilon_1+\varepsilon_2$) through sequential strain release of ε_1 first and ε_2 second and two-step oxygen plasma treatment with time of T_1 and T_2 . (i) 3 small waves on top of one large wave, i.e. ratio of 1:3, generated with $(\varepsilon_1, T_1, \varepsilon_2, T_2) = (25\%, 360s, 25\%, 3000s)$, (ii) ratio of 1:4 with $(25\%, 270s, 25\%, 3000s)$, (iii) ratio of 1:5 with $(25\%, 200s, 25\%, 3000s)$, and (iv) ratio of 1:6 with $(25\%, 120s, 25\%, 2400s)$. Scale bar is $5\mu m$. (b) AFM 3D image of hierarchical wrinkles with a ratio of 1:4 with cross sectional profile shown in (c).52

Figure 3.3: (a) Tunable transmittance of a hierarchically wrinkled PDMS elastomer (ratio of 1:4) with different levels of applied stretching strains. (b) Intensity spectrum of the wrinkled elastomer at different angles with the applied stretching strain of 0%. (c-f) the corresponding optical images showing the transparency (i) and structural color (ii) at a fixed angle of 30° and SEM images (iii) at different stretching strain of 0%, 15%, 30%, and 50%. Scale bar is $10\mu m$53

Figure 3.4: The combined tunable optical transparency and structural color of hierarchically wrinkled PDMS elastomer with different wave number ratios with mechanical strains (the initial pre-stretched strain was set to be 50% for all samples). (a-c) The optical images of samples with different wave number ratio (1:3 for (a), 1:5 for (b), and 1:6 for (c)) show the combined opacity (i) and iridescent structural color (ii) at stretching strain of 0%, as well as the combined transparency (iii) and iridescent structural color (iv) at stretching strain of 50%. The optical images for structural color were taken at a fixed angle of 30° . The remained structural color was observed in all the samples after re-stretching to their initial pre-stretched strain of 50%. (d) Intensity spectrum of the wrinkled elastomer at different angles with the applied stretching strain of 0% and 50% for different wave number ratios. (e) Corresponding measured tunable transmittance of the samples at different levels of applied stretching strains from 0% to 30%. (f) The comparison of the measured tunable transmittance of the sample with wave number ratio of 1:4 before and after 100 cycles of mechanical strain stretch and release at different strains. (g) The corresponding large-area SEM images at the same spot before and after 100 cycles with a strain rate of $0.15s^{-1}$56

Figure 3.5: FEM simulation on the formation of hierarchical wrinkles through sequential wrinkling (i-iii), as well as the evolution of wrinkles with applied stretching strain (iii-v).59

Figure 3.6: Comparison between theory and experiments on the normalized amplitude of the small wrinkles in the hierarchical wrinkles as a function of second released strain ε_2 with the first released strain $\varepsilon_1=20\%$ fixed. Inset: AFM images and cross sectional profiles at different strains of ε_262

Figure 3.7: The optical images show the Young contact angle ($\sim 110^\circ$) on flat PDMS (a) and the static apparent static contact angle ($\sim 125^\circ$) on hierarchically wrinkled PDMS elastomer (b) with the wave number ratio of 1:4 without further treatment of superhydrophobic coatings, respectively.65

Figure 3.8: (a) Schematic illustration of controlling the motion of water droplets on inclined hierarchically wrinkled surfaces with tilted angle of α_t from pinned to sliding through applied mechanical stretching and release. (b) Corresponding experimental demonstration with optical images taken from a video showing the control of water droplet's movement on an inclined hierarchically wrinkled PDMS surface (tilted angle of $\alpha_t = 45^\circ$) from pinned to sliding through applied stretching strain, and vice versa through strain release. The camera was set at an angle of 35° with respect to the sample to obtain a larger field of view, showing a captured side view at 10° . (c) Sliding angle α of hierarchically

wrinkled PDMS surfaces with different wave-number ratios for different water droplet volumes as a function of applied stretching strain ϵ	66
Figure 4.1: Schematics of the process of generating multiscale self-similar hierarchical wrinkles on PDMS elastomers through combined plasma and UVO treatment and two-step strain release.	78
Figure 4.2: (a) SEM images of hierarchical wrinkles generated with $\epsilon_1 = \epsilon_2 = 25\%$, $T_1=5\text{min}$, $T_2=40\text{min}$. left: magnified view. (b) Corresponding AFM images of hierarchical wrinkles with measured horizontal and vertical cross-sectional profiles along the white dashed line shown to the bottom and to the right, respectively. (c) Corresponding optical profilometer images of level-2 large-wavelength wrinkles in the hierarchical wrinkle with measured cross-sectional profile along the white dashed line shown to the bottom.	81
Figure 4.3: (a) Measured wavelength and amplitude of the generated small-wavelength wrinkles as a function of the plasma treatment duration. (b) Measured wavelength and amplitude of the generated large-wavelength wrinkles as a function of the UVO treatment duration. All the pre-strain is set to be 25%.....	83
Figure 4.4: (a) The thickness of first layer stiff film generated on first strain release as a function of the Plasma treatment time. (b) The thickness of second layer stiff film generated on second strain release as a function of the UVO treatment time.	84
Figure 4.5: AFM images of hierarchical wrinkling surface with $\epsilon_1 = \epsilon_2 = 25\%$, $T_1=5\text{min}$, $T_2=40\text{min}$. From the cross sectional profile located at the valley of small wrinkles, it can be seen that the wide crack disappears but narrow cracks exist, indicating the wide cracks occur during the first release.	85
Figure 4.6: Dependence of the measured crack densities on (a) 1 st -step released strain, (b) 2 nd -step released strain, (c) plasma treatment duration, and (d) UVO treatment duration.	87
Figure 4.7: (a) SEM image of a hierarchical wrinkled structure with $A_1 \approx 267 \text{ nm}$, $\lambda_1 \approx 750 \text{ nm}$, $A_2 \approx 4.2 \mu\text{m}$, $\lambda_2 \approx 21.4 \mu\text{m}$. Inset: top view optical image of a $5\mu\text{L}$ water droplet resting on the hierarchical wrinkled surface. (b) Side views of the droplet oriented to the parallel (top) and perpendicular (bottom) directions of wrinkles, respectively.	89
Figure 4.8: (a) Dimensionless free energy density curves vs. the normalized penetration depth for hierarchical wrinkles with different wrinkling aspect ratios. Note that the curves have been translated vertically for clarity. (b) Confocal images combined of reflectance scan (grey) and fluorescence signal (green) at different focus lengths on the peak (i), middle (ii), and valley (iii) of the wrinkle grooves as illustrated by the schematic on the bottom. Nanoparticles (green) are seen from the peaks to the valleys of the wrinkles. The hierarchical wrinkled structure has the dimension of $A_1 \approx 267 \text{ nm}$, $\lambda_1 \approx 750 \text{ nm}$, $A_2 \approx 4.2 \mu\text{m}$, $\lambda_2 \approx 21.4 \mu\text{m}$	95
Figure 4.9: Relation between the measured contact angles and Wenzel contact angles.....	99
Figure 4.10: Images of advancing and receding contact line when (a) contact line moves against hierarchical wrinkles (b) contact line moves against cracks. (c) Contact angles in the parallel and perpendicular directions of wrinkles before and after vibration on hierarchical wrinkled surfaces. ...	101
Figure 4.11: Schematic model for the three phase contact line moving against hierarchical wrinkled structure.	102
Figure 4.12: (a) Free energy change as a function of contact angle when the three phase contact line moves against the wrinkles for the hierarchical wrinkled structure with $A_1 \approx 267 \text{ nm}$, $\lambda_1 \approx 750 \text{ nm}$, $A_2 \approx 4.2 \mu\text{m}$, $\lambda_2 \approx 21.4 \mu\text{m}$ (b) Free energy changes as a function of contact angle when the three phase	

contact line moves against the wrinkles for the hierarchical wrinkled samples with different aspect ratios of level-2 micro-wrinkles.	105
Figure 4.13: Schematic illustration of modeling cracks of two levels.....	109
Figure 5.1: (a) Schematic illustration of fabrication process of 2D hierarchical wrinkling surface. (b) Corresponding SEM images of 2D hierarchical wrinkling surface.	115
Figure 5.2: (a) Fabrication process of wrinkling surface. (b) SEM images of representative wrinkling surface.	118
Figure 5.3: SEM images of condensed water on wrinkling surface. The Chamber pressure is 7.2torr, temperature is 4.9°C. Condensation duration is 25mins.....	118
Figure 5.4: Time evolution of water condensation on wrinkling surface showing the coalescence. The Chamber pressure is 5.6torr, temperature is 2.1°C. Condensation time was marked in red, the unit is minute.....	119
Figure 5.5: Time evolution of water condensation on wrinkling surface showing the large droplet growth. The Chamber pressure is 5.6torr, temperature is 2.1°C. Condensation time was marked in red, the unit is minute.	119
Figure 5.6: Time evolution of water condensation on wrinkling surface showing the single droplet growth. The Chamber pressure is 5.6torr, temperature is 2.1°C. Condensation time was marked in red, the unit is minute.	119
Figure 5.7: SEM images of wrinkles with ridges covered by silica nanoparticles.	120
Figure 5.8: SEM image showing the discrete strips of particle distribution after evaporation on wrinkling surface. Insert: zoom in SEM image.....	121
Figure 5.9: (a) FEM simulations of buckling of two edge fixed plates with different width. (b) Schematic illustration of lattice structure.....	123

LIST OF TABLES

Table 4.1: Measured static and dynamic contact angles and degrees of wetting anisotropy on hierarchical wrinkled PDMS substrate.....	90
Table 4.2: Calculated and measured advancing and receding contact angles in the parallel direction of hierarchical wrinkled PDMS substrate	108

CHAPTER 1 INTRODUCTION

1.1 Mechanical Instabilities

It has been a long history on the study of mechanical instability in engineering since late 1700's when Euler developed the classical Euler equation formulating the buckling of elastic column. For centuries, mechanical instabilities have been considered as a major issue in the engineering associated with the large deformations and catastrophic failures of slender structural elements. Thus in engineering, most historical research is related to instabilities fall in the context of preventing structural failure. However, nature has witnessed the power of mechanic instabilities in the growth and evolution in many biological and geological phenomena, including skin wrinkles [1], shape formation of vital organs[2], morphogenesis of leaves[3] and fruits[4], and the formation of mountain ridges[5].

Since the last decade, the research of mechanical instability has shifted to an exciting new area of controlling and harnessing mechanical instabilities in soft materials including pattern transformation[6, 7], wrinkling[8, 9], folding[10, 11], delamination[12], and creasing[13, 14] (Figure 1.1). These intriguing soft structures induced by instability have led to discovery of a wide range of potential applications, including flexible electronics [15, 16], thin film metrologies[17], photonic or phononic devices[18-20], microfluidic channels[21, 22], platform for cell studies[23], and auxetic materials[24].

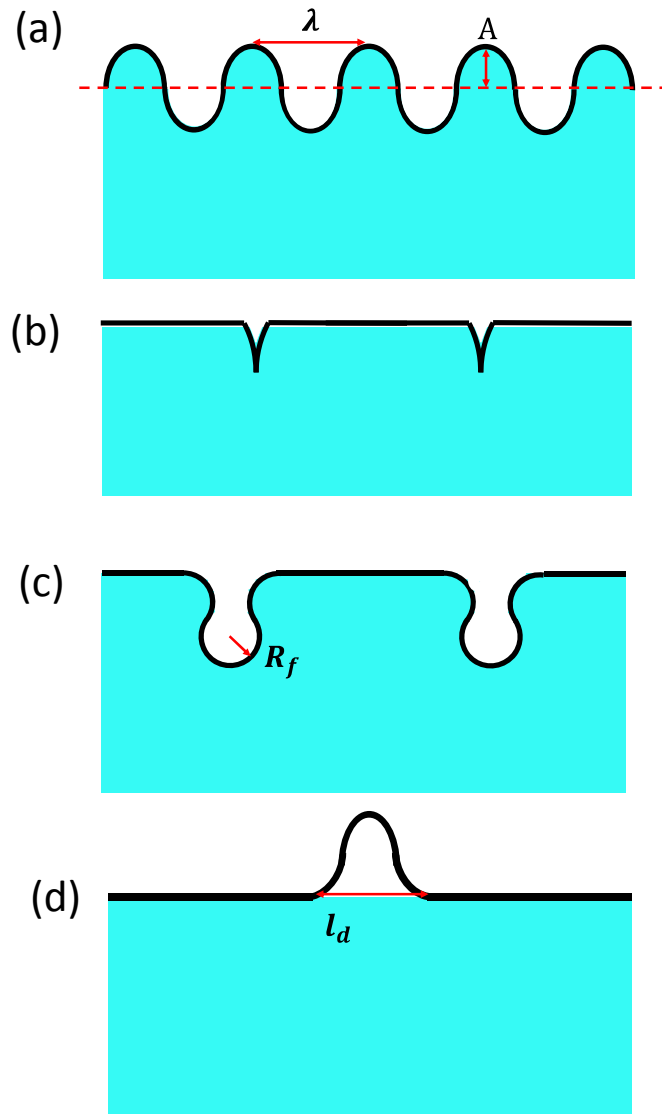


Figure 1.1: Mechanical instability with characteristic length. (a) Wrinkling (b) Creasing (c) Folding (d) Delamination

1.1.1 Pattern transformation

When periodic structures sustain external load that triggers structural instability, it will undergo a large deformation and transform to another periodic structure which differentiates from initial structure. Such a process is called a pattern transformation. Pattern transformation could be initiated by mechanical forces[25], capillary force[26]

and osmotic pressure[20] for applications including directed nanoparticle assembly[7], phononic crystals[20], color switch[25], tunable photonic[27] and auxetic materials[28].

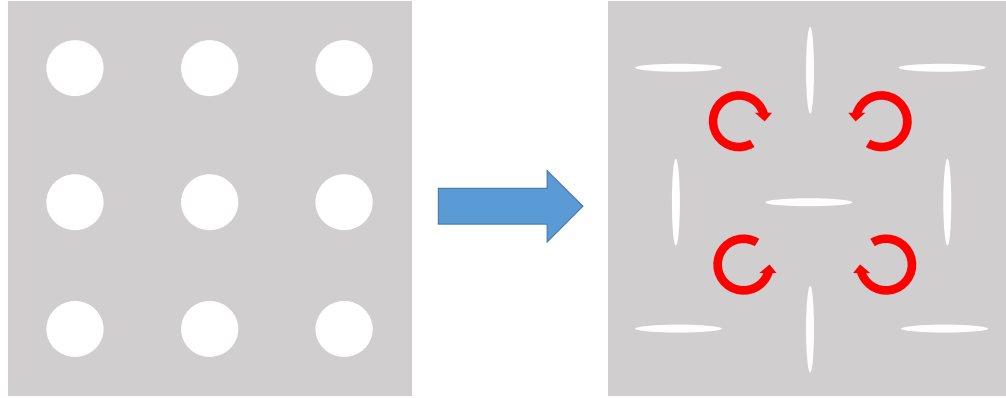


Figure 1.2: Pattern transformation of circular holes in square lattice.

One of most studied structure is a square lattice of circular holes in a soft membrane as shown in Figure 1.2. When such a membrane is under compression, these circular holes deform to mutually orthogonal ellipses and the joints connecting the neighboring holes rotate significantly (red arrow in Figure 1.2). Through finite element simulation, Bertoldi et al. suggested that joints rotation only happens when the porosity is greater than 34%[24]. Otherwise, the poles will simply collapse into slits in response to compression. Mullin et al. changed the circular hole to ellipses and thus changed the resultant transformed pattern[6]. Bertoldi and coworker further studied the pattern transform of square lattice holes but with a series of hole shapes from circle to square to star shape to find the optimal shape for auxetic material[29]. They found a higher compaction ratio larger than that of circle holes could be achieved. They also investigated the pattern transformation on 3D spherical shell which leads to the encapsulation by void closure, which depends on the shell thickness and void density[30]. Kang et al. attached

the membrane to a rigid substrate which constrained the rotation of bottom of interconnected joints, leading to a phenomenon called symmetry breaking[31].

1.1.2 Wrinkling

Surface wrinkling could be commonly observed in nature, such as the wrinkles of raisin and wrinkles of human skin. Surface wrinkling could be generated by compressing a stiff film coated on a thick compliant substrate which could be either planar or curved[4]. For the simplest case, when the thin film is under compression without delamination, it buckles into a sinusoidal shape to release the accumulated stress in the film as shown in Figure 1.1a. The unique surface patterns generated by wrinkling have been harnessed for broad range of applications, including microfluidic devices[32], templates for colloidal assembly[33, 34], stretchable electronics[15, 16], and tunable optical gratings [35, 36]. Surface wrinkling can generate controllable ordered or randomly disordered buckling patterns from the nanometer to millimeter scale depending on the applied strain, material modulus, and film thickness[8, 9, 32]. Energy method is often used for non-linear buckling analysis[37]. If the prestrain is small (less than 5%), small deformation model predicts the wrinkling wavelength and amplitude of sinusoidal wrinkles as[37]

$$\lambda = 2\pi t_f \left(\frac{\bar{E}_f}{3\bar{E}_{sub}} \right)^{\frac{1}{3}} \quad (1.1)$$

$$A = \frac{\lambda}{\pi} \sqrt{(\varepsilon - \varepsilon_{cr})} \quad (1.2)$$

where $\bar{E} = E/(1 - \nu^2)$ is the plane-strain modulus, E is Young's modulus and ν is Poisson's ratio. The subscripts “ f ” and “ sub ” stand for the film and substrate, respectively.

$\varepsilon_{cr} = 0.25\left(\frac{3\bar{E}_{sub}}{\bar{E}_f}\right)^{\frac{2}{3}}$ is defined as the critical buckling strain. Equation (1.1) and (1.2) suggest that both the wavelength and amplitude are linearly proportional to the film thickness and only the amplitude increases with the prestrain quadratically. That means, due to the assumption of small strain, the prestretch strain is released through the increase of the buckling amplitude while the wavelength remains unchanged.

For finite deformation (large than 5%) model, the finite deformation and geometrical nonlinearity of soft substrate must be taken into account, the wrinkling wavelength and amplitude could be related to those of the small strain case as[38]:

$$\lambda = \frac{\lambda_0}{(1+\varepsilon)(1+\xi)^{1/3}} \quad (1.3)$$

$$A = \frac{A_0}{(1+\varepsilon)(1+\xi)^{1/3}} \quad (1.4)$$

Here λ_0 and A_0 are the wrinkling wavelength and amplitude for the small strain case given by Equation (1.1) and (1.2). $(1 + \xi)^{1/3}$ comes from the nonlinearity of finite deformation with $\xi = 5\varepsilon(1 + \varepsilon)/32$.

1.1.3 Creasing

Creasing is similar to wrinkling but requires a thick layer of incompressible soft material attached to a rigid substrate. When the soft part is under compression while the rigid substrate remains undeformed, an elastic instability arises in which free surface deeply folds up on itself to locally release compressive stress (Figure 1.1b). Typically, creases appear as slits or tri-wing shaped. Interestingly, wrinkling which becomes unstable at high strain can transit to creasing due to the existence of small initial

defects[39]. The creasing morphology has been utilized by Kim et al. to reversibly display fluorescein-containing patterns in a thermal-responsive hydrogel film[23]. A surface with dual instabilities, both wrinkles and creases, has also been applied as a patterned substrate for polymeric solar cell to enhance the current density[19].

1.1.4 Folding

Folding is a localized bending which normally originates from the later stage of wrinkling on an elastic substrate (Figure 1.1c) [10, 40]. Pocivavsek et al. have investigated the wrinkling to folding transition for a plastic film on water. They found that when the film displacement is three times larger than the wrinkling wavelength, the wrinkle becomes unstable and energetically unfavorable[10]. Instead, a transition from wrinkling to folding will occur. The amplitude of folds is linearly proportional to the displacement which is in sharp contrast with the wrinkling amplitude that depends on the applied strain. From the scaling law, the radius of fold tip, i.e. the position of the maximum curvature, could be approximated given by[10]

$$R_f \sim \left(\frac{B}{K\Delta^2}\right)^{1/2} \quad (1.5)$$

where B and K are defined in bending stiffness of the film and K is the stiffness of the substrate. Δ is the film displacement with respect to the compression. Brau et al. suggest that the fold forms progressively starting with multiplication of wrinkling wavelength and ending with self-contact[41].

1.1.5 Delamination

When the bonding between a film and its substrate is not strong enough to withstand the tension stress, the film may detach from the substrate which is a typical characteristic of delamination as shown in Figure 1.1d. The delamination typically appears as localized blisters either strip-like[42] or circular shape[43] depending on stress state. Vella et al. have developed the scaling laws for the critical size l_d of the blister which defined as the initial length of strip like blister or the initial diameter of circular blister. For a thin strip on a thin substrate, l_d is

$$l_d \sim \left(\frac{B^2 w}{E_{sub} t_{sub} \Gamma} \right)^{1/5} \quad (1.6)$$

where w is the width of the strip, Γ is the interfacial toughness. Based on Griffith's criterion, Γ equals to the work of separating an interface. For a wide strip on a thick substrate, l_d scales as

$$l_d \sim \left(\frac{B^2}{E_{sub} \Gamma} \right)^{1/5} \quad (1.7)$$

When the stress is beyond the critical threshold, the cracks surrounding the blister grow further. Hutchinson et al. show that in the initial stage of the crack growth, the blister remains nearly circular[43]. As the stress further increases, the crack growth becomes unstable growing to a telephone cord or a varicose structure depending on the Poisson's ratio of the film due to length-wise perturbation. Moon et al. demonstrated that the telephone-cord like delamination patterns can be assembled into microfluidic channel or networks to greatly promote chemical mixing [22, 44]. Edmondson et al. also showed

that delamination can be harnessed to pattern the surface by patterning the adhesion between the polymer film and gold coated silicon substrate[45].

1.2 Reconfigurable Soft Materials

Soft materials such as gels, elastomers, and biological tissues can easily generate and sustain large deformation in response to various external stimuli, such as mechanical forces, PH value, temperature, humidity, electric and magnetic field [46-51]. These stimuli responsive properties make the soft materials widely applied in soft actuators[52, 53], switches[54, 55], sensors[56, 57], artificial muscles[58, 59] and biological scaffolds[60, 61]. The reversible and dramatic shape change induced by elastic instability of soft materials offer unique opportunities for the design of responsive and reconfigurable soft structures over a wide range of length scales. Soft materials with specifically designed structures could significantly change their configuration when instability occurs induced by external stimuli. As a result, a variety of structure dependent physical properties including wettability[62], adhesion [63], optical transmittance[64, 65], structural color[66], stiffness[67] and acoustic band gap[68] will change correspondingly. For example, Lee et al. studied the structure of nanopillars on wrinkled elastomers. The initial prepared sample with wrinkles existence at released state is optical opaque and superhydrophobic. When the wrinkles are stretched back to flat, the sample becomes transparent and hydrophobic simply due to the reconfigured morphology [65]. Rudykh et al. studied the wave propagation in layered media[68]. They found the initially straight interfacial layer could wrinkle when a critical compressive strain is achieved. The

wrinkled interfacial layer forms a system of periodic scatters which reflect and interfere with the incident wave leading to band gaps in wave propagation. These studies have proven that different from static and rigid elements in most conventional materials, instability driven reconfigurable soft material can easily deform and reconfigure its surface or structural configurations, offering a potential multifunctional platform through simple mechanical deformation.

1.3 Outline of This Thesis

In this thesis, I designed the novel instability driven reconfigurable soft materials with tunable properties through a combination of theoretical, numerical and experimental analyses. I reveal the mechanics underneath the mechanical instability of soft structures with certain structure and show the equilibrium configurations before and after instability, which is fundamental and essential for designing reconfigurable soft materials. I also investigated how the desired property could be tuned in response to the reconfigured soft structures, and the corresponding tunable surface or structure related properties, including optical property such as transmittance, color ,and absorption, electric property, wettability, and adhesion, as well as mechanical property such as strength, stiffness, density, Poisson's ratio and stretchability.

This thesis is organized as follows:

In Chapter 2, I discussed the strategy to control buckling direction using introduced cuts. It demonstrates that the buckling direction could be controlled by

specific designed structures and developed potential application of controlled buckling as the conductive pathway.

In Chapter 3, I discuss the design of smart window using hierarchical wrinkling surface. It demonstrates that the hierarchical wrinkling surface could be fabricated through a sequential stretching and oxidation treating method. It showed that such self-similar hierarchical wrinkling surface has tunable optical transmittance and wettability and thus suitable for multifunctional smart window application.

In Chapter 4, I discuss the dynamic wetting property of hierarchical wrinkling surface. Through experiments and theoretical model, it explained the influence of contact line pinning effect on the anisotropic wetting behavior of hierarchical wrinkling surface.

In Chapter 5, I discuss the possible future work related to the work done in this thesis with some preliminary results.

CHAPTER 2 CUTS GUIDED DETERMINISTIC BUCKLING IN ARRAYS OF SOFT ACTIVE PARALLEL PLATES FOR MULTIFUNCTIONALITY

Note: This Chapter was partially adapted and modified from the publication below:

G. Lin, D. Ge, Y. Tang, Y. Xia, G. Wu, L. Han, S. Yang and J. Yin, “Cuts guided deterministic buckling in arrays of soft parallel plates for multifunctionality”, *ACS Appl. Mater. Interfaces*, 9(34), 29345-29354 (2017)

2.1 Introduction

Buckling instability is a deformation mode involving abrupt switching between two distinct equilibrium states under compression. It has historically been considered as structural failure in engineering. In recent years, the benefits of buckling instabilities, including buckling in structures[69], as well as wrinkling, creasing, and delamination in thin film-substrate systems[9, 70, 71], have been realized in soft materials at all scales and found a wide range of applications, including dynamically tunable surface topography related properties such as tunable dry adhesion[72, 73], tunable wetting[62], anti-biofouling[74], microfluidic channels[75], enhanced cell adhesion and alignment[76, 77], smart windows[25, 26], as well as structural reconfiguration related properties in stretchable electronics[16], mechanical metamaterials[78, 79], and energy trapping[80]. The realization of such broad applications highly relies on the controllable buckling behavior of the structures and interfaces. Unlike the extensively studied buckling/wrinkling of thin films on substrates, harnessing plate buckling for functionality receives little attention and remains largely unexplored[81]. The challenge lies in the control of global buckling order in plates. Considering buckling of a vertical freely-standing plate under compression, the plate can buckle to the left or to the right since

both configurations are energetically equivalent. The simple example implies that buckling is intrinsically undetermined in terms of its buckle orientation. Such an uncontrolled buckling could lead to geometrical frustration and undesired, disordered configuration[8, 31, 82-86] in structures at all scales. When it extends to arrays of vertical parallel plates, a typical structure in wave guiding[87-89] and heat transfer[90], a global disorder would be expected after buckling due to the indeterminate buckling orientation in each plate.

Some efforts have been made to manipulate the deformation pathways by breaking symmetry of the whole structures. For example, by controlling the aspect ratios of the swellable 2-D hydrogel microstructures, Kang *et al.*[31] report highly symmetric and ordered structures through pattern transformation. By pre-twisting kagome lattices to introduce a preferred bending direction, Wu *et al.* [91] demonstrate smooth and homogenous structural reconfiguration in a deterministic fashion by avoiding buckling instability. Likewise, single-handed chiral structures are induced in pH-sensitive hydrogel membranes[92]. By imposing nanofibers between one-dimensional (1-D) nanowalls to prevent their recovery from the deformed state to the original state, long-range ordered two-dimensional (2-D) wavy structures are achieved[93].

It is important to point out that these examples all rely on interactions between the interconnected structure units, allowing for control of the global buckling directions. Questions arise for the *discrete* 1-D structures (e.g. vertical plates), where individual structural elements are not interactive before buckling. Can we deterministically and reversibly switch between 1-D and 2-D structures with both local and global ordering?

Can we further control the interaction between discrete 1-D structures after buckling for functionality, e.g. dynamically tuning the “communication” pathways *on demand* for potential applications in adaptive electronic and optic devices?

Here, by introducing cuts with variable size and geometry in arrays of 1-D parallel polymer plates, I demonstrate precise control of the buckling directions in local elements triggered by mechanical stretching, bending, and solvent swelling. The originally disordered buckling configurations transit to a long-range structural ordering after introducing patterned cuts. By harnessing cut-directed buckling for controllable contacts and interactions, I create a wide range of combinations of conductive pathways that can be reconfigured reversibly and locally to guide wave propagation electrically and optically.

2.2 Cuts Guided Deterministic Buckling

2.2.1 Buckling behaviors of discrete thin plates without cuts

Figure 2.1a and 2.1b illustrate the buckling behaviors of an array of discrete thin plates with and without cuts. Experimentally, I demonstrated the buckling in thin plates made of pH responsive hydrogel, poly(2-hydroxyethyl methacrylate-*co*-acrylic acid) (PHEMA-*co*-PAA), whose swelling ratio can be controlled by pH of the buffer solutions[94] as shown in the scanning electron microscopy (SEM) images seen in Figure 2.1c and 2.1d. PAA has pKa of 4.7. When pH value is increased from 2 to 5, the lateral length swelling ratio changed from 1.24 to 1.48. Because the plate is physically constrained to the non-swelling rigid substrate, glass, the plate undergoes compression and buckles laterally when beyond a critical strain. The plates stay in the buckled state until change of pH or upon solvent evaporation to return to the original discrete plates. I

can also use materials that are glassy in the dry state but rubbery upon swelling (e.g. PHEMA) to lock the structure in the dried state[95]. For the soft mechanical metamaterial without cuts (Figure 2.1a and 2.1c), each discrete plate locally buckled into periodic sinusoidal waves, however, globally, it exhibited a disordered array of buckling configurations with randomly shifted phase angles between plates (right of Figure 2.1c). This is because the direction of each buckling wave is undetermined as discussed before (right of Figure 2.1a), depending on the geometrical or materials imperfections in each discrete plate. Such buckling induced disordering is also observed macroscopically in elastomeric polydimethylsiloxane (PDMS) plates upon immersion in hexane (Figure 2.2), as well as in nanoplates[83, 93], demonstrating its scale-independent characteristics.

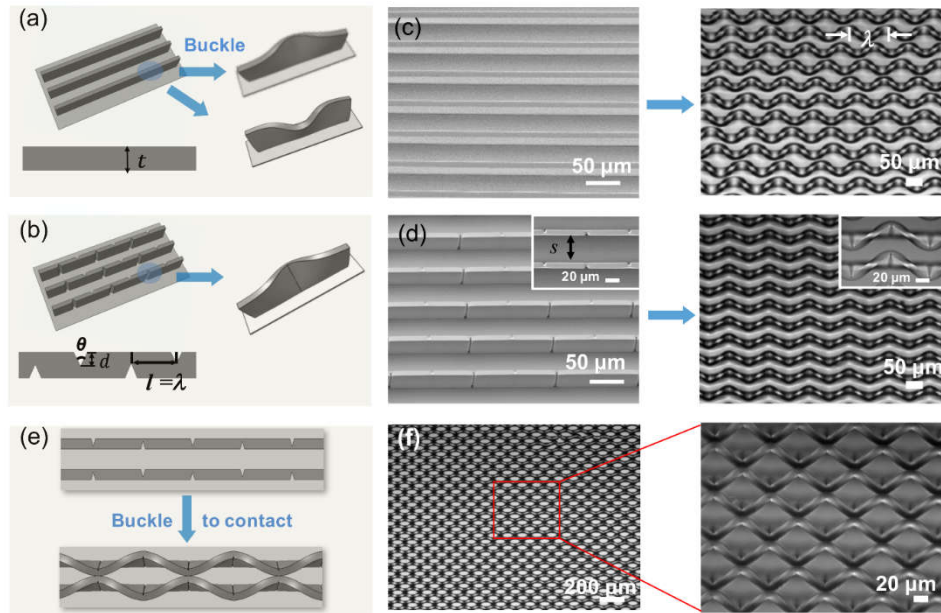


Figure 2.1: Cut-guided reversible peak-valley contacts in 1-D soft reconfigurable mechanical metamaterials via buckling. (a-b) Schematic illustration of a simple metamaterial without cuts (a) and with identical patterned V-shaped cuts (b) (c-d) Left column: tilted view of SEM images of a hydrogel mechanical metamaterial with vertical micro-plates without cuts (c) and with identical patterned V-shaped cuts (d). Each plate has height $H = 60 \mu\text{m}$, thickness $t = 20 \mu\text{m}$, and space between plates $s = 40 \mu\text{m}$. Right column: corresponding top view of optical images of buckled hydrogel mechanical

metamaterials after swelling. Insets are the magnified top view of plates with V-shaped cuts before (left) and after buckling (right), showing cuts right locating at wave trough or peak. (e) Schematic illustration of applying opposite orientations of patterned V-cuts to two neighboring plates to enable cut-guided peak-valley contacts after buckling; (f) Left: corresponding top view of optical images of well-controlled peak-valley contacts guided by patterned opposite cuts in a swelling-driven buckled hydrogel mechanical metamaterials over large area; right: magnified optical images showing the occurrence of valley-peak contacts is right at cut locations.

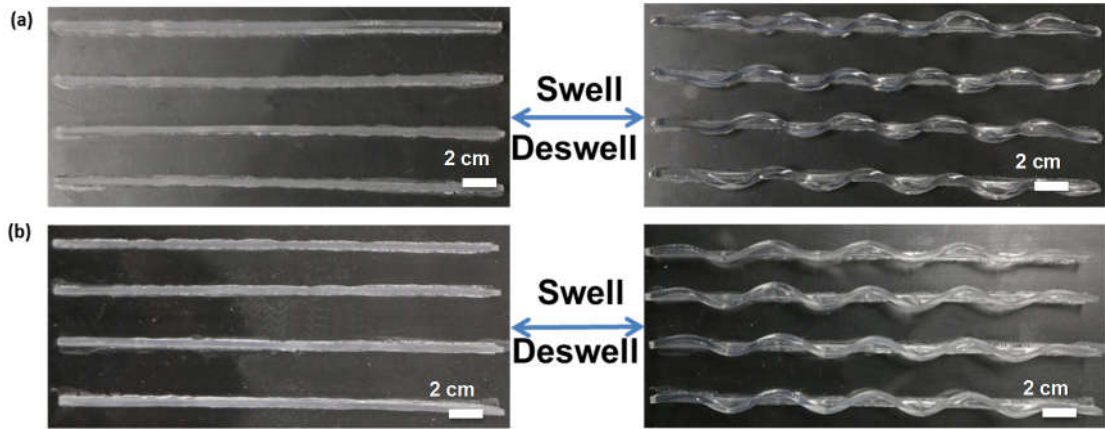


Figure 2.2: Demonstration of transition from the disordered buckled configuration to the ordered one in an array of macroscale PDMS plates with bottoms attached to the acrylics sheet upon swelling in hexane. (a) Plates without cuts before deformation (left) and after swelling-induced buckling (right), showing randomly distributed phase angles between plates. (b) Plates with the patterned V-shaped cuts on every plate before deformation (left) and after swelling-induced buckling (right). Cuts are right located at wave troughs or valleys to direct the buckling.

2.2.2 Buckling behaviors of discrete thin plates with cuts

To direct the buckling direction and thus to control the buckling phase angle, the key is to break the axial symmetry during the out-of-plane buckling of the plate through imposing either material or geometrical imperfection across the plate thickness. As a proof-of-concept, I introduce an array of relatively simple “V”-shaped cuts on the hydrogel micro-plates through pre-fabricated features using photolithography (see experimental section for more details) to direct the buckling right at the cut regions

(Figure 2.1b and 2.1d) and the apex of the “V”-shaped cuts shows a rounded tip with a small radius. More complex cut shapes could be introduced. When the plate is under axial compression, the “V”-shaped cut will generate a bending moment to close the cut right at the tip, and thus directing the buckling direction (right of Figure 2.1c). With the same cut patterns placed on each plate (left of Figure 2.1d), 2-D waves with the same phase angle throughout the entire film are formed, as seen from both the hydrogel micro-plates (right of Figure 2.1d) and the silicone macro-plates (Figure 2.2b). Here, the distance between two neighboring cuts, l (Figure 2.1b and 2.1d), is designed to be equal to the buckling wavelength λ without cuts (right of Figure 2.1c), *i.e.* $l = \lambda$ (See discussion later on the mechanics model and related simulation on this). This way, the “V”-shaped cut induces the formation of a wave trough while the “Λ”-shaped cut forms a wave peak by closing the cuts (inset of right of Figure 2.1d). In principle, the precise control of buckled wave phase angles via cuts in a single element will enable the manipulation of global phase angle distribution in the entire structure. By placing “V”-shaped cuts with opposite orientations in the two adjacent plates (top of Figure 1e and left of Figure 2.1f), I demonstrated the global structural ordering with a 180° phase angle shift between the neighboring buckled hydrogel plates, which enabled the buckling induced valley-peak contacts (bottom of Figure 2.1e and right of Figure 2.1f). To ensure the buckled plates making contacts with each other in a continuous fashion, I set the distance between the parallel plates, s , to be no greater than twice of the amplitude of buckle waves A , *i.e.* $s \leq 2A$. The valley-peak contacts between the adjacent waves (right of Figure 2.1f) offer the highest contact pressure and the most stable contacts (Figure 2.3), whereas the non-valley-peak contacts can slide continuously during the post-buckling process after initial

contacts. Despite the adhesion between hydrogel microplates upon contact, after deswelling, the buckled and contacted hydrogel micro-structures return to their original discrete and non-contacted configuration (Figure 2.4), which is reversible. It should be noted that to guarantee the reversibility, the elastic energy stored in the buckled and bent hydrogel microplates should be large enough to overcome the adhesion to restore to their original uncontacted state, which requires that the hydrogel microplate be not too thin since its bending stiffness is proportional to t^3 with t being the plate thickness, otherwise they will remain stick to each other as observed in the relatively thinner hydrogel stripes ($t=15\mu\text{m}$) in experiments due to their largely reduced bending stiffness.

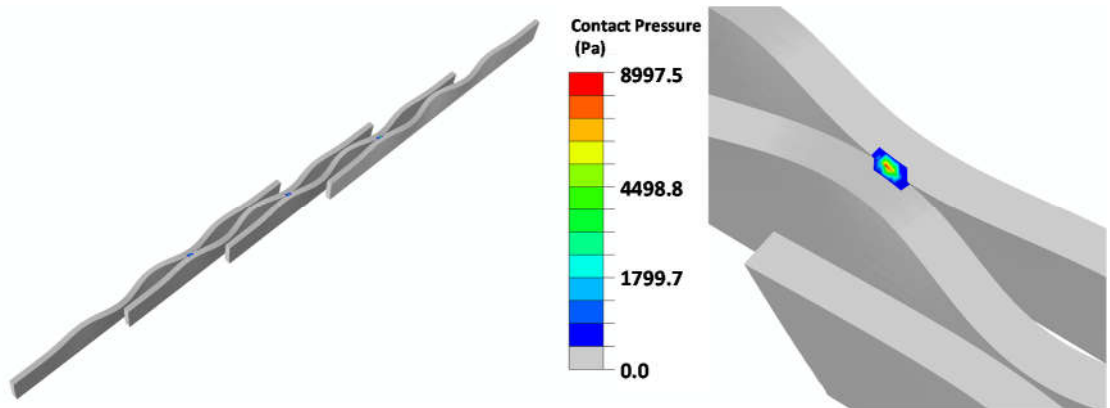


Figure 2.3: FEM shows the highest contact pressure at the valley-peak contact between two buckled plates without sliding in the post-buckling process.

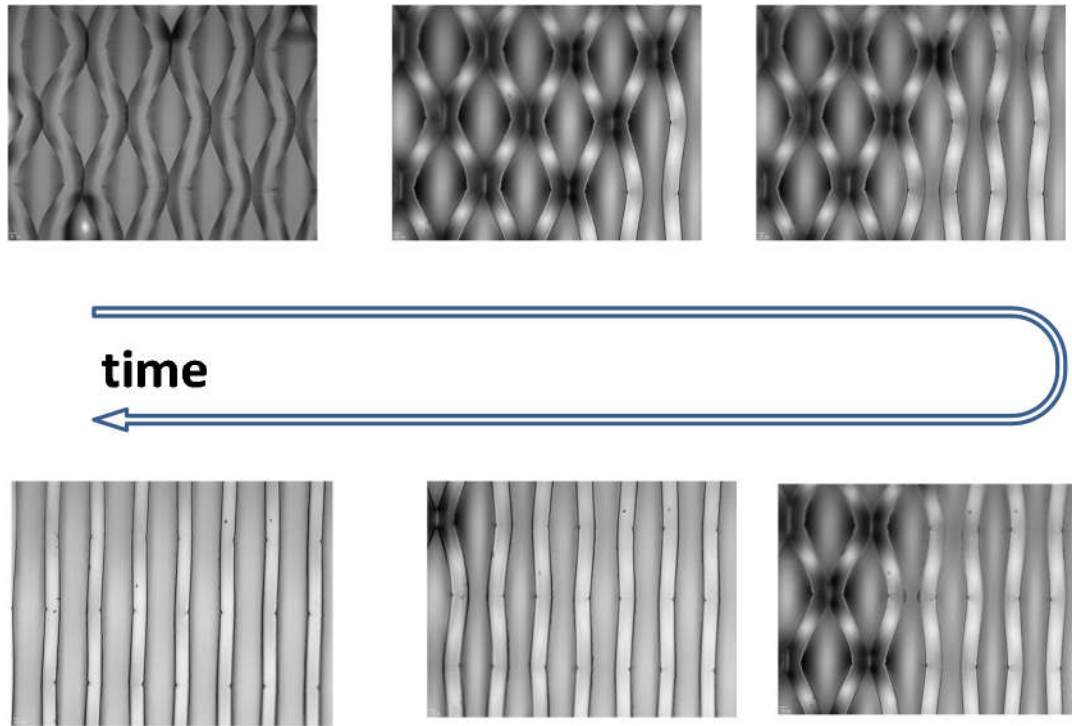


Figure 2.4: Time lapse optical images of the deswelling process of an array of hydrogel micro-plates with patterned cuts upon solvent evaporation, showing the fully reversible contact and dis-contact process despite the adhesion between hydrogel micro-plates when in contact.

2.2.3 Buckling behavior of discrete thin plates with only partially periodic cuts

To show the necessity of periodic patterned cuts for the global ordering of the buckled plates, I examined the buckled structures from those with single cut or partial cuts but identical cut geometries and positions in each plate. It is found that a shallow single cut or partially patterned cuts can help reduce the critical buckling strain and thus a faster response compared to plates without cuts but cannot lead to a globally ordered configuration (Figure 2.5). Introduction of a single cut (Figure 2.5a) can only locally direct the buckling direction right at the cut location, but fail to direct the global phase angle of the plate, leading to a randomly shifted phase angle distribution between plates due to the uncontrollable random fabrication imperfections (Figure 2.5b). When the

identical patterned shallow cuts are applied to part of the hydrogel plates (Figure 2.5c), as expected, well-controlled buckling is observed in the regions with patterned cuts, which are located right at the wave trough or peak with the same phase angle. In the transition regions from patterned cuts to no cuts, however, disordered buckling configuration is observed when the location of the cuts is away from the wave trough or peak (Figure 2.5d, bottom left). In the region without cuts, it shows a disordered buckling configuration with mismatched phase angles between plates possibly due to the intrinsic random geometrical defects during the micro-fabrication (Figure 2.5d, bottom right). Therefore, applying partially patterned cuts also fails to render the long-range structural ordering. Nevertheless, it is clear that the buckling wavelength and amplitude play important roles in guiding the design of cut patterns for controlled peak-valley contacts.

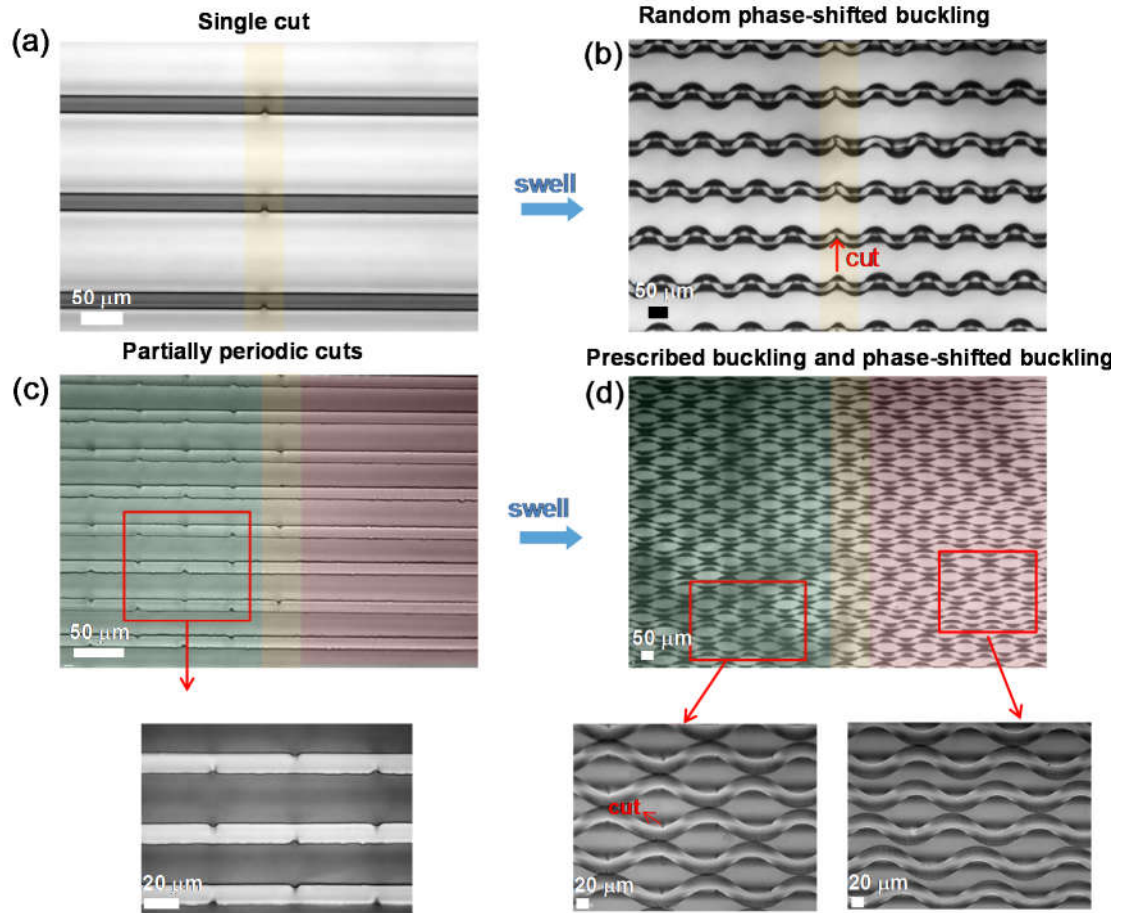


Figure 2.5: Effect of a single cut (a-b) and partially periodic cuts (c-d) on the buckling of an array of hydrogel micro-plates. (a) and (c): Optical images of arrays of hydrogel plates before swelling. (b) and (d): The corresponding optical images of random phase-shifted buckling (b), as well as a combination of prescribed ordered buckling and phase-shifted buckling (d) after swelling. The cut and non-cut regions are highlighted in green and pink colors to facilitate visualization, respectively.

2.3 Design of Cuts Guided by Modeling and Simulation

2.3.1 Theoretical model of bottom constrained plate

First, let us discuss the theoretical prediction of the buckled geometry of the polymer plates. For plates without cuts, we can use the buckling model of bottom clamped elastic plates under side compression force N_x per unit length to predict the critical buckling strain ϵ_b , buckling wavelength λ , and amplitude A through the classical buckling analysis. I use the buckling

model of bottom clamped elastic plates under side compression to understand the buckling behavior in swelling induced constrained buckling in hydrogel or PDMS plates.

The total potential energy of the plate is given by:

$$\Pi = \frac{D}{2} \iint \left\{ \left(\frac{\partial^2 w}{\partial x^2} + \frac{\partial^2 w}{\partial y^2} \right)^2 - 2(1-\nu) \left[\frac{\partial^2 w}{\partial x^2} \frac{\partial^2 w}{\partial y^2} - \left(\frac{\partial^2 w}{\partial x \partial y} \right)^2 \right] \right\} dx dy + \frac{1}{2} \iint \left[N_x \left(\frac{\partial w}{\partial x} \right)^2 + N_y \left(\frac{\partial w}{\partial y} \right)^2 + 2N_{xy} \frac{\partial w}{\partial x} \frac{\partial w}{\partial y} \right] dx dy \quad (2.1)$$

$$N_x = ft \quad (2.2)$$

$$N_y = 0 \quad (2.3)$$

$$N_{xy} = 0 \quad (2.4)$$

where H is the plate height, f is compression force acting on the side, t is the plate thickness, and $D = \frac{Et^3}{12(1-\nu^2)}$ is flexural rigidity with E and ν being the Young's modulus

and Poisson's ratio, respectively. w is the out-of-plane deflection, which is assumed as $w = A \left[6 \left(\frac{y}{H} \right)^2 - 4 \left(\frac{y}{H} \right)^3 + \left(\frac{y}{H} \right)^4 \right] \cos \left(\frac{\pi x}{\lambda} \right)$, where A and λ are the in-plane amplitude and buckling wavelength, respectively. The four-order polynomial here is attributed to the deflection of a cantilever under uniform distribution load. The assumption is verified by comparing to the simulated deflection of buckled plates using FEM simulations as shown in Figure 2.6.

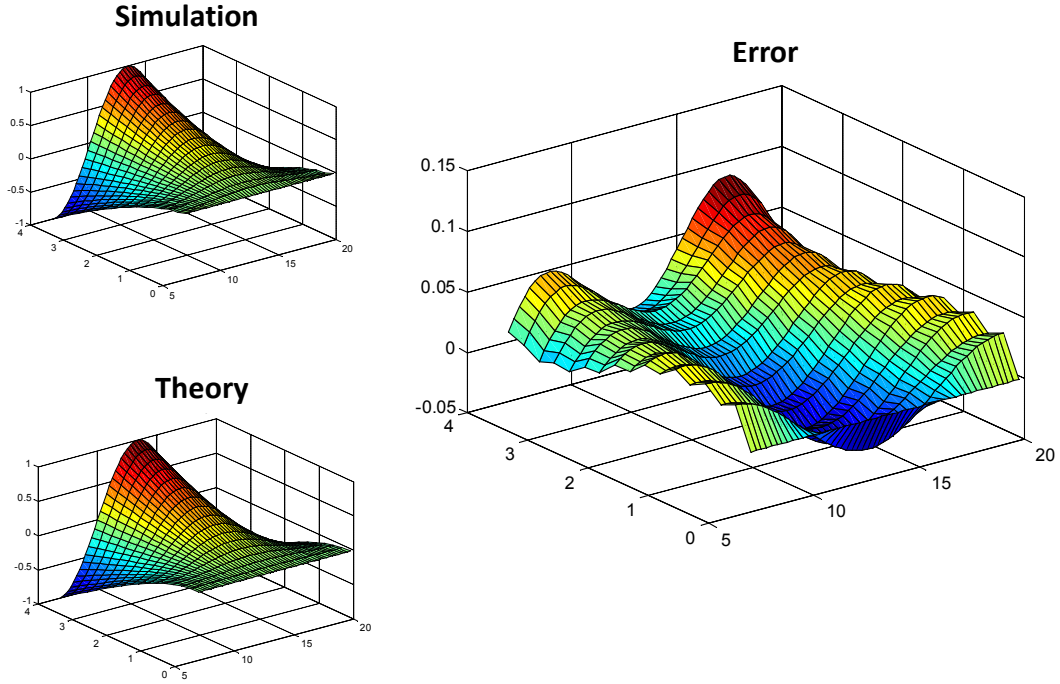


Figure 2.6: Comparison of the theoretically assumed deflection mode with the numerically simulated deflection profile, showing good agreement.

By minimizing the total potential energy with respect to A after substituting w into Equation (2.1), the acting force f can be solved as

$$f = \frac{1}{91} \frac{D(91H\pi^4 + 810H^2\pi^2\lambda^2 + 1134\lambda^4 - 945H^2\pi^2\lambda^2\nu)}{t\pi^2H^4\lambda^2} \quad (2.5)$$

For PDMS and hydrogel, I assume $\nu = 0.5$. The critical buckling force and buckling wavelength can be obtained by minimizing the compression force with respect to wavelength λ , $\frac{\partial f}{\partial \lambda} = 0$, we can obtain

$$\lambda = 1.672H \quad (2.6)$$

Plugging Equation (2.6) into Equation (2.4), the critical buckling force becomes

$$f = \frac{10.769D}{tH^2} = \frac{10.769Et^2}{12H^2(1-\nu^2)} \quad (2.7)$$

I assume that the total plate length does not change during buckling. For a sinusoidal buckling mode $y = A\cos(kx)$, the total length of the sinusoidal wave is

$$L = \int_0^{\frac{2\pi}{k}} \sqrt{1 + \left(\frac{dy}{dx}\right)^2} dx \quad (2.8)$$

It can also be expressed in terms of wavelength λ and amplitude A as

$$L = \frac{A^2\pi^2 + \lambda^2}{\lambda} \quad (2.9)$$

At the onset of buckling, the critical buckling wavelength λ_{cr} can be expressed as

$$\lambda_{cr} = \frac{A^2\pi^2 + \lambda_{cr}^2(1 - \varepsilon + \varepsilon_{cr})^2}{\lambda_{cr}(1 - \varepsilon + \varepsilon_{cr})} \quad (2.10)$$

Rewrite Eq. (2.10),

$$A = \frac{\lambda_{cr}\sqrt{\varepsilon - \varepsilon_{cr}}\sqrt{1 - \varepsilon + \varepsilon_{cr}}}{\pi} \quad (2.11)$$

Assuming the deformation is small, that is, $\varepsilon - \varepsilon_{cr} \ll 1$,

$$A \approx \frac{\lambda_{cr}\sqrt{\varepsilon - \varepsilon_{cr}}}{\pi} \quad (2.12)$$

Equation (2.7) (2.6) and (2.12) show that ε_b and λ are independent of the Young's modulus of plate materials, E . ε_b increases nonlinearly with the aspect ratio of the plate t/H . λ is proportional to H and independent of t . A is proportional to λ and increases nonlinearly with the strain in the plate. The theoretical model is further validated by both

finite element method (FEM) simulations and experiments for macro- and micron-plates with and without cuts, showing good agreement with each other (Figure 2.7a-c).

2.3.2 FEM simulation

Guided by Equation 2.6, I investigate the control over the directional buckling by design of cuts and thus peak-valley contacts in the mechanical metamaterial using FEM simulation. The geometry of the cut patterns as defined in Figure 2.1c, including the cut periodicity l/λ , the normalized cut depth d/t , and the opening angle θ , is varied systematically. FEM simulation shows that the patterned cuts do not always enable the buckling right at the cut location, *e.g.* when l is not set to be the odd number of factor of λ , (*e.g.* $l/\lambda = 0.5$ and 1.5 in Figure 2.7d), or when the cut depth is shallow (*e.g.* $d/t = 0.025$ in Figure 2.7e), or when θ is relatively small (*e.g.* $\theta = 1^\circ$ in Figure 2.7f). As d/t or θ increases, the buckling is directed at the cuts as shown in Figure 2.7e and 2.7f. Despite their large effect on the buckling direction and thus buckling wave phase angles, the patterned cuts show a negligible influence on the buckling wavelength when compared with the pristine plates without cuts.

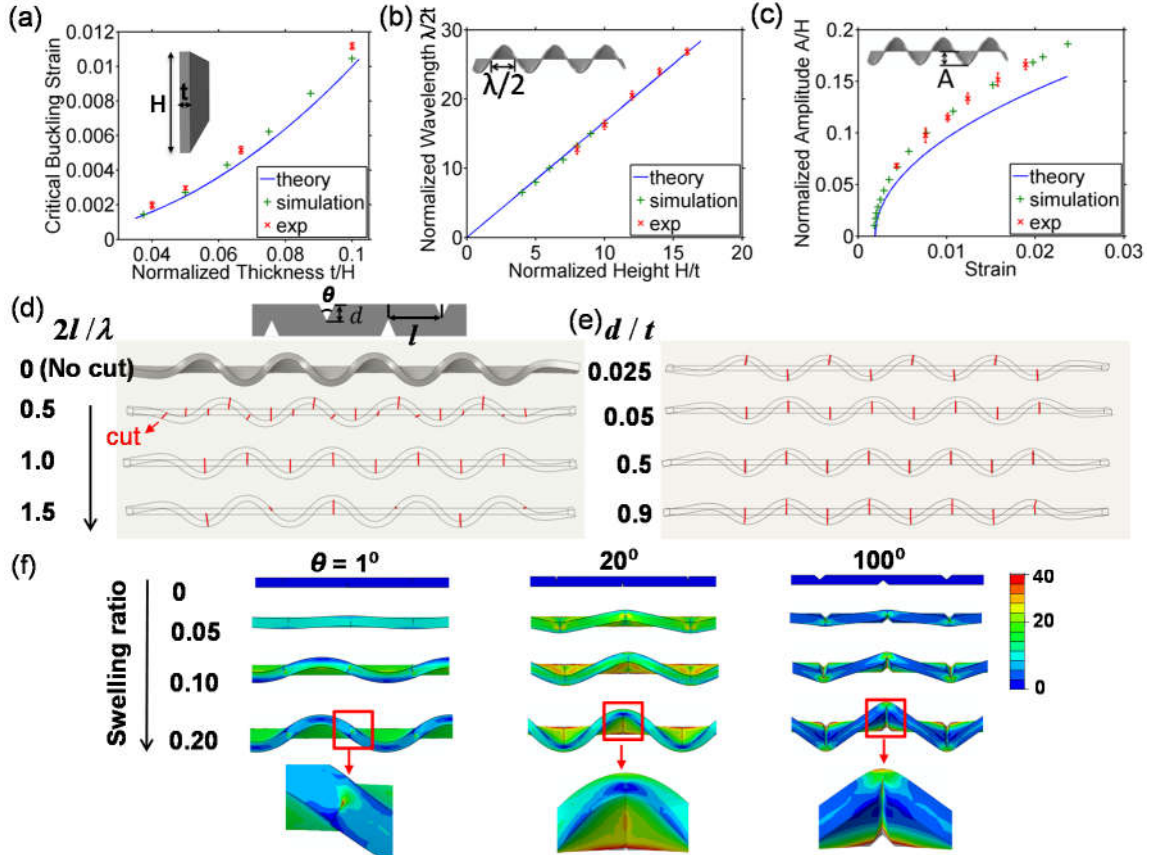


Figure 2.7: Engineering the geometry and patterning of V-cuts to direct the buckling direction right at the cuts in 1-D mechanical metamaterials via predictive mechanics model and FEM simulation. (a-c) Comparison between theoretical models, simulation, and experiments on the critical buckling strain (a), wavelength (b), and amplitude (c) in buckling of a bottom-constrained plate without cuts. (d-f) FEM simulation results on directing the buckling through patterned cuts in plates with $H/t = 4$ by engineering the periodicity of cut patterning l/λ (d), the normalized cut depth d/t (e), and opening angle θ (f). (f) Also shows the evolution process of representative structural reconfigurations and von Mises stress contours in plates with different θ as the swelling ratio increases from 0 to 0.2. Stress unit is in kPa.

Figure 2.7f further shows the evolution of representative structural configurations in the plate when the swelling ratio is increased from 0 to 20% at different θ . The plate starts to fold slightly when it begins to swell for all θ , and then it either buckles or continues to fold without buckling as the swelling ratio increases, depending on θ . For a

relatively large θ (e.g. $\theta = 100^\circ$), the plate prefers to fold, generating sharp straight folds (bottom right of Figure 2.7f) in contrast to the formation of sinusoidal waves for a smaller θ , causing high stress concentration located at the tips of both the cut and the sharp folds. Similar stress concentration is observed at the cut tip for a small cut angle (e.g. $\theta = 1^\circ$) owing to out-of-plane shearing to tear the cut (the bottom-left image of Figure 2.7f). In both scenarios, stress concentration may lead to potential failure at the tip. However, in contrast, no stress concentration is observed at both locations with moderate θ (e.g. $\theta = 20^\circ$), which is effectively released through buckling, and thus will be more robust. Considering the requirement of cut-directed buckling and mechanical robustness with less stress concentration, the parametric FEM simulation results suggest that, in order to direct the buckling using the patterned cuts, the cuts should satisfy $l/\lambda = 1$, $6^\circ \leq \theta \leq 50^\circ$, and $0.05 \leq d/t \leq 0.5$, which corroborates with experimental observation (Figure 2.1d).

As seen from Equation (2.7), after cuts, the effective thickness of the plates is decreased, leading to a reduced critical buckling strain, which is consistent with the reduced critical buckling load in buckling of plates with both sides being free after introducing a notch[96]. The lowered critical buckling strain after cuts will be beneficial for speeding the response time in external stimuli-responsive materials. Furthermore, Equation (2.6) shows the buckling wavelength is only proportional to the height and independent of the thickness, implying that the cuts might have negligible effects on the buckling wavelength, which is consistent with the FEM simulations and experimental observations.

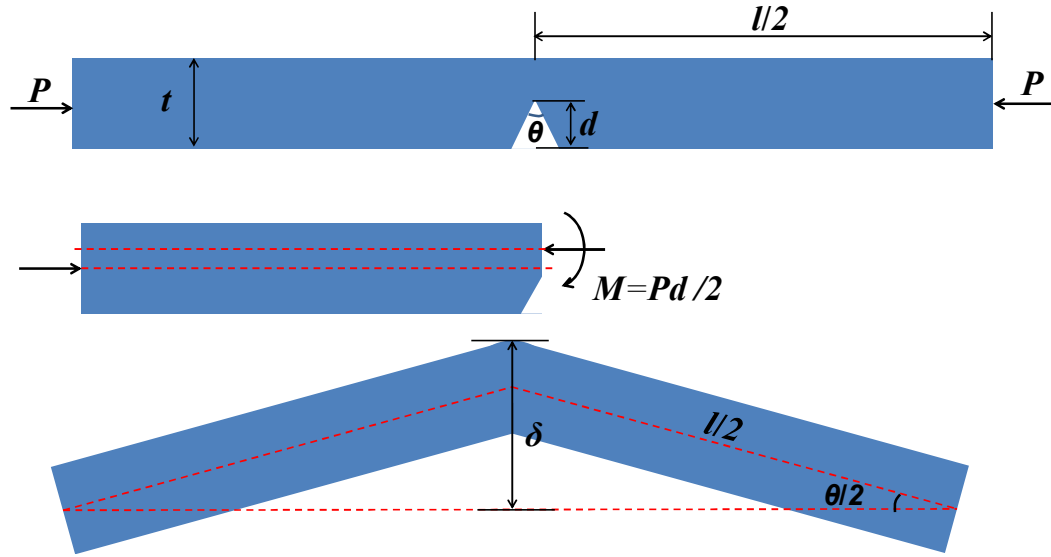


Figure 2.8: Schematic illustration of beam bending at a triangular cut.

In general, the patterned cuts play the role of geometrical imperfections, which not only induce but guide the buckling by closing the cut right at the buckled wave peaks or troughs. As seen from Figure 2.7f, during the initial swelling, the segments between cuts undergo rigid rotations around the cut first to close the V-shaped cuts, forming a zigzag shaped geometrical imperfection to trigger the occurrence of buckling. When the cuts are fully closed, it forms a corrugated “continuous” plate without cuts and the normalized magnitude δ of the zigzag imperfections by the plate thickness t reaches the maximum with $\delta/t = l \sin(\theta/2) / (2t + 1/\cos(\theta/2))$ (Figure 2.8), showing that δ/t increases with the opening angle θ . Apparently, for a small θ , δ/t is small and insufficient to guide the buckling (left of Figure 2.7f). For a $\theta > 90^\circ$, the large cut opening cannot be fully closed due to the bottom constraint, leading to continuing folding without buckling. To reach the maximum magnitude of imperfection, it requires sufficient bending moment at the cut location to fully close the cut. The positions of peaks or troughs of a sinusoidal buckling

mode have the largest deflection, and thus possess the largest bending moment to fully close the cuts when the locations of cuts are set to coincide with wave peaks or troughs, i.e. $l = \lambda$; otherwise, some of the cuts will not be fully closed for directing the buckling at cuts (Figure 2.7d). Similarly, when the cut depth d/t is shallow, the relatively larger bending stiffness (proportional to the uncut depth $(t-d)$) at the cut position makes it harder to become fully closed given the same bending moment. However, a much deeper cut will dramatically reduce the local stiffness and cause potential cut breakage despite its guidance of buckling, which should be avoided.

2.4 Applications of Cuts Guided Deterministic Buckling

2.4.1 Switchable electrical conductive pathway

Armed with the knowledge of how to design the cuts to induce deterministic buckling, I demonstrated multi-functionality enabled by cut-directed buckling. First, I tested the possibility of switching the electrical conductivity between the neighboring plates via buckling in proof-of-concept experiments. To do so, I coated conductive carbon grease onto the discrete PDMS plates (thickness $\sim 50 \mu\text{m}$) with a periodic cut pattern designed according to Equations (2.2) and (2.3) and placed in parallel to each other (Figure 2.9). As illustrated in the electrical circuit layouts in Figure 2.10a-d, a Domino-like conductive pathway in series can be realized by shifting the plates of identical cut patterns by one buckling wavelength horizontally to allow valley-peak contact (Figure 2.10b), while the parallel conductive pathway can be realized by applying symmetric cut patterning between plates without shifting (Figure 2.10c-d). The conductive pathways were selectively and reversibly activated through swelling,

transverse stretching, or longitudinal bending of the silicone rubber substrate (Figure 2.10d) fixed on a thin, flexible acrylic plate, leading to electrical conduction in series or parallel, respectively, as demonstrated by the lighting up of the red LED lights. Upon release of the mechanical loading, the plates returned to the original discrete state and the LED lights were off (Figure 2.10a and 2.10c). The switch of “on” and “off” was carried out for 100 cycles, and a small drop of conductivity, ~12% (Figure 2.10e), was observed. This could be attributed to the small abrasion between the contact points or delamination of conductive coatings on PDMS during stretching and bending, which could be improved using more compliant conductive coatings. For comparison, figure 2.11 shows that an array of PDMS plates without cuts was immersed in hexane solution to swell. Since hexane dissolves the carbon based conductive grease, the PDMS plates were partially immersed in hexane with the conductive coating of carbon grease on the top unexposed to hexane solution, and thus only the immersed part of the plates will swell, leading to the buckling of the PDMS plates. Since there are no cuts introduced to the plates, I observed the buckled sinusoidal wave shapes with random phase angles, which led to the uncontrollable side contacts between plates. Despite the random buckling and contacts, the red LED light was shown to be lit up with buckling-induced contacts. Since the contact does not occur at the valley-peak locations, the slight sliding of contact points was observed during the swelling process, and thus cut-guided controllable contacts were needed. After the hexane evaporates, the buckled structure returned to its original parallel state without contact, showing a reversible process.

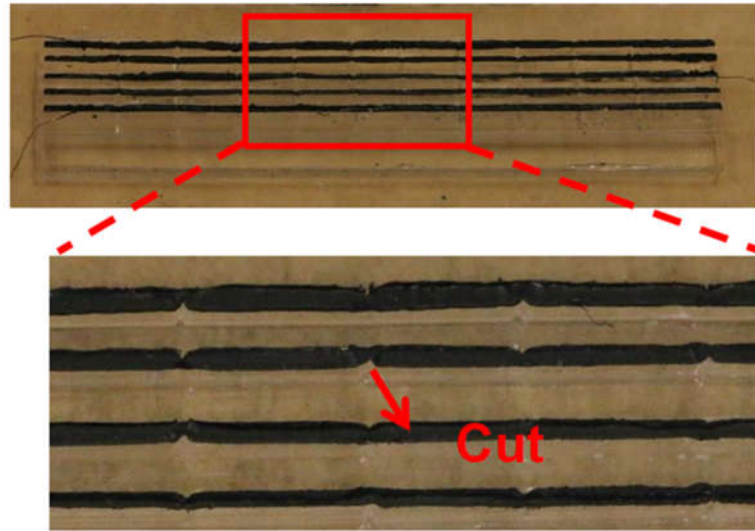
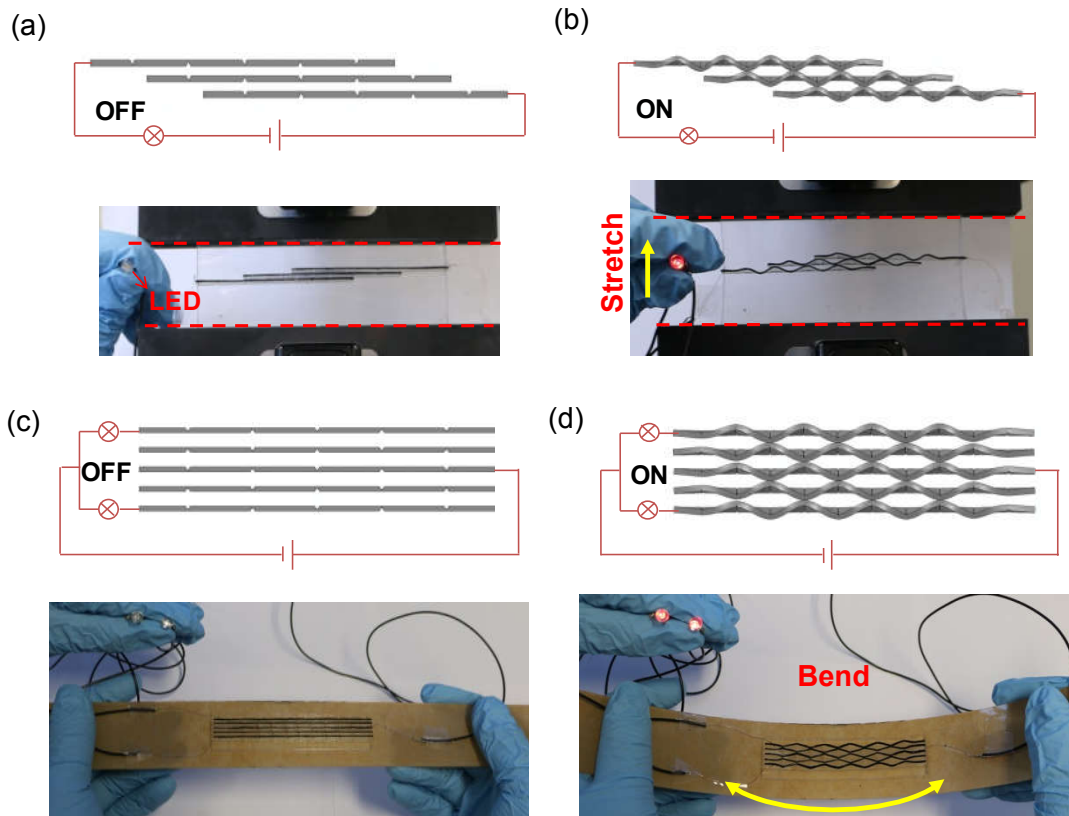


Figure 2.9: Zoom-in figure shows the conductive coating and V-shaped cuts on macro-scale PDMS plates.



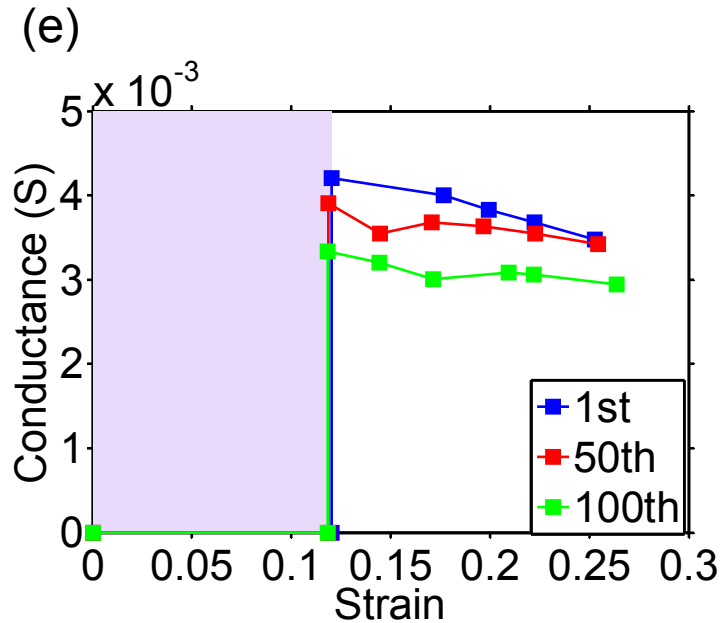


Figure 2.10: Demonstration of cuts-guided peak-valley contacts via directional buckling for activating switchable electrical conductive pathways. (a-d) Mechanically activating the Domino-like in-series (a-b) and parallel (c-d) electric circuits via cuts-guided peak-valley contacts driven by buckling of macroscale PDMS plates with conductive coatings. Buckling-induced contacts in plates occur and thus LED lights are on either by transversely stretching (b) or by longitudinally bending (d) the attached substrates. (e) Change of conductance after cycles of stretching-unstretching in (b).

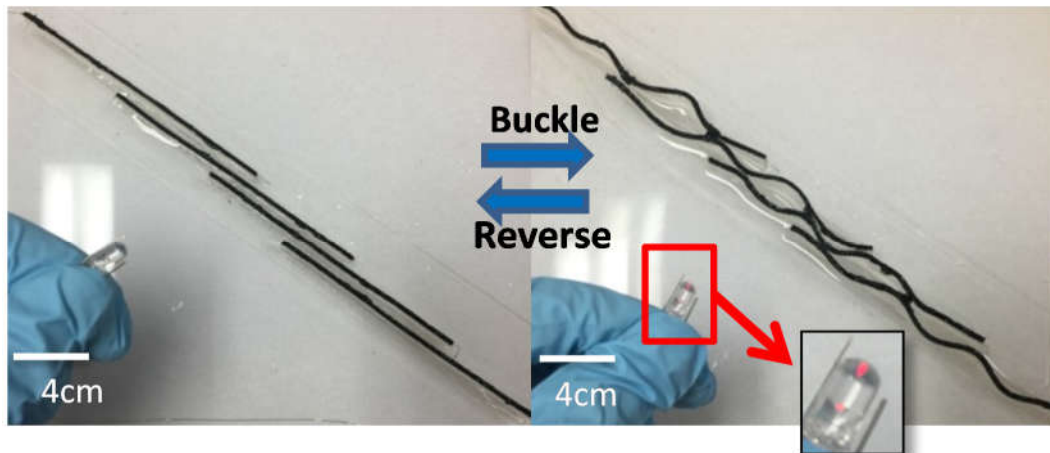


Figure 2.11: Swelling induced activation of the switchable electrical conductive pathway through buckling induced contact in array of PDMS plates coated with black carbon-based black conductive grease without cuts.

2.4.2 Mechanical logic gates

The switching between on and off through contacts could provide a potential function of basic mechanical logic gates and switches⁴⁰ that perform operations of AND, OR, and NOT depending on the setting of the distance s between two parallel plates and the introduced patterned cuts

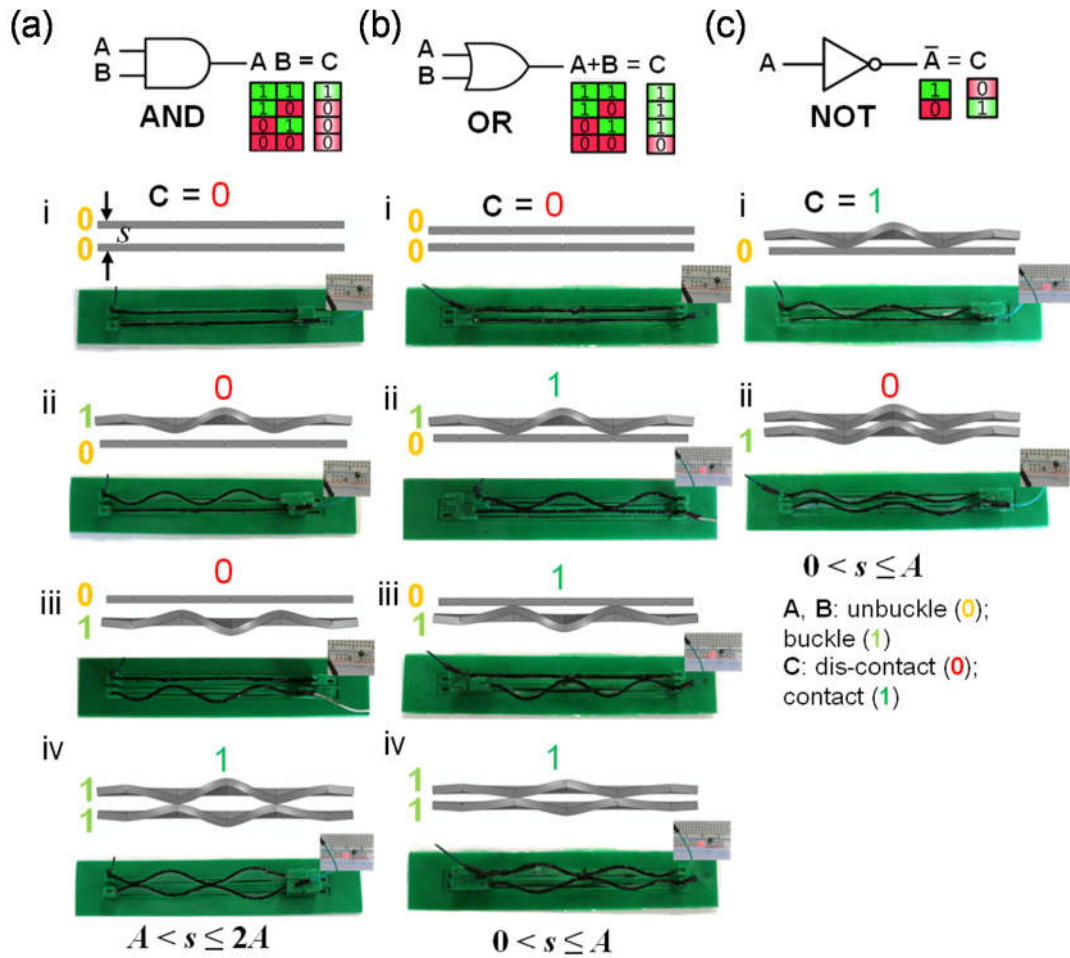


Figure 2.12: Designs of mechanical logic gate-like switchable conductive pathway via cut-guided directional buckling for functions of AND (a), OR (b), and NOT (c) operations demonstrated in a unit of two parallel bottom constrained plates. The buckled state is “1”, unbuckled state is “0”. The red LED light is on when the output of corresponding logic gate is “1” (“11” for AND, “10, 11” for or, and “0” for NOT).

Figure 2.12 demonstrates the design of mechanical logic gates through cut-directed buckling in two adjacent parallel plates. Only two output states are allowed: Logic “1” is referred as the contact state and the conduction (as indicated by the lightening of LED) is on, and Logic “0” is referred as the non-contact state and the conduction is off. Similarly, the inputs have two states when in response to external stimuli: Logic “0” represents no buckling, and Logic “1” represents buckling in the plate. Different patterned cuts are introduced to the two parallel plates to guide the directional buckling and contact for realizing different logic operations. For both AND and OR operation, symmetric cuts (Figure 2.12a(i) and 2.12b(i)) are introduced to enable valley-peak contacts after buckling of both plates, while for NOT operation, the two plates are set to have the identical patterned cuts (Figure 2.12c(i)) to buckle with the same phase angle, thus a non-contact state after buckling of both plates. For the proof-of-concept demonstration, similar to switchable electrical conductive pathway in Figure 2.9 and 2.10, I used thin PDMS stripes as the plate with electrical conductive coatings. The buckling of individual plate is induced by compressing the plate using a 3D printed home-made device.

When s is set to be $A < s \leq 2A$ with A being the buckle amplitude, it can perform the AND operation activated by external stimuli (e.g. mechanical compression as shown in Figure 2.12a), where only the concurrent buckling of two plates (two Logic “1” inputs) can lead to contact (Logic “1” outputs), indicated by the lightening of LED as shown in Figure 2.12a(iii). When s is set to be $0 < s \leq A$ (Figure 2.12b and 2.12c), it can perform either the OR operation or NOT operation, depending on the initial pre-set state of two plates. When the pre-set plates are initially straight (Figure 2.12b(i)), buckling of either plate (Figure 2.12b(ii)) or both plates (Figure 2.12b(iii)) can lead to contact, and thus the

output of Logic “1” and the lightening of LED. When one buckled plate is initially set to be in contact with another straight plate (an output of Logic “1” and lightening of LED, Figure 2.12c(i)), buckling of the straight plate under compression (an input of Logic “1”) leads to the same buckled phase angle through the to switch from contact to non-contact state, and thus the output of Logic “0” and LED light is off (Figure 2.12c(ii)). Similar buckling induced contact was demonstrated in the design of mechanical switches in micro-electro-mechanical systems (MEMS)[97-99], where a bistable beam with both ends clamped was laterally pushed in the center to enable a snap-through buckling to induce the contact and conduction connection. Compared to bistable buckling, our method is more controllable in the buckling behavior of plates and their contacts through cut-directed deterministic buckling. Accordingly, more complex conductive pathways, including hierarchical structures and polyline can be designed. Figure 2.13 illustrates some conceptual designs to show the potential of controlled buckling that could enable possible logic gates and complex pathways. Additional work needs to be carried out to validate the designs through selective activation and control of buckling in plates. It shows a design consisting of straight plates with patterned cuts in a centered rectangular arrangement, which are disconnected in both horizontal and vertical directions to cut off conduction. The overlapping length between the two neighboring parallel plates is designed to allow for at least one valley-peak contact upon buckling. Upon local buckling in the highlighted area, the mechanical metamaterial becomes locally connected in an binary tree shape (Figure 2.13a) and in an italic “L” shape (Figure 2.13b) with contacts in the vertical, oblique, and horizontal positions defined by cuts while the unbuckled area remains disconnected.

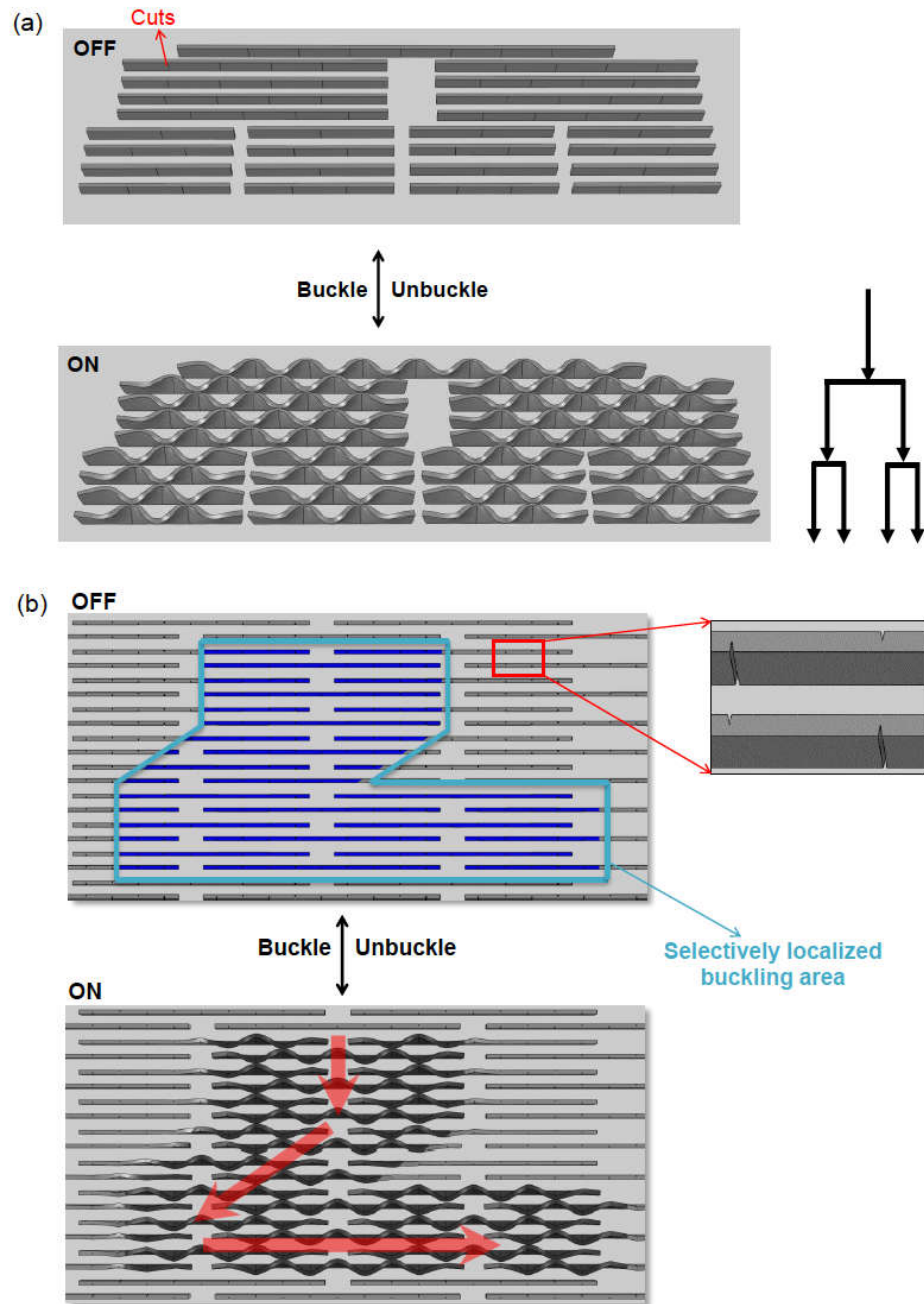


Figure 2.13: FEM simulations of complex conductive pathways with cut-directed controlled contacts via buckling. (a) A hierarchically branched pathway. Top: undeformed configuration. Bottom: buckled and connected configuration. Right: corresponding schematic illustration of a hierarchical branched electrical circuit. (b) Design of a confined polyline conductive pathway connecting vertical, oblique, and horizontal directions embedded in discrete rectangular-centered patterned plates via

localized buckling in the highlighted area. Top: undeformed configuration. Bottom: localized buckled configuration shows the generation of polyline conductive pathway.

2.4.3 Switchable optical properties

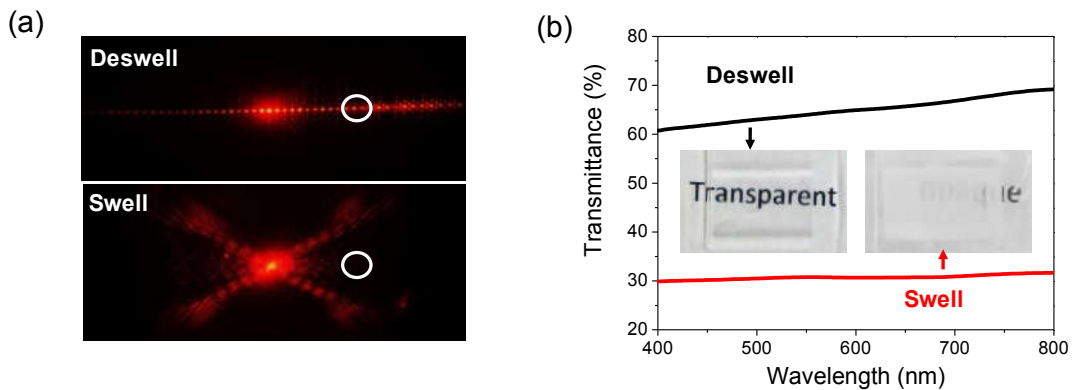
While buckling-induced contacts directed by cuts are scale-invariant, there could be new benefits when pattern size shrinks to (sub)micron scale. Unlike the electrical conductive pathways, where conductivity relies on the contact pressure between the buckled plates, in the case of directing optical responses, it is more governed by the globally buckled patterns rather than the contact pressure for conductance. Figure 2.14a shows the light diffraction pattern from the array of hydrogel microplates before and after swelling. Before buckling, the red laser light (wavelength of 633 nm) was transmitted along the plate's long axis. After the buckled plates making contact, the laser light was split at the intersection and propagated diagonally, bypassing the spot indicated by the white circle where the light would have propagated through in the original plate. The new pathway is the result of the formed globally interconnected lattice structure after buckling.

Besides redirecting the light propagation pathways, we can also change the light reflection from the array of buckled soft plates. As seen in Figure 2.14b, upon swollen in the pH 4 buffer solution, the average transmittance of the hydrogel soft plate arrays in the visible wavelength (400 nm-800 nm) decreased significantly, from ~ 66% (pristine film) to ~ 31%. The switching time is on the order of tens of seconds due to the fast diffusion of water on the micro-sized hydrogel. Similar to the switchable optical transparency via wrinkling of continuous thin films on substrates[64, 65, 100], the largely reduced optical

transmittance demonstrated in our system consisting of discrete micro-plate array is attributed to the light reflection from the contacted top surfaces between the twisted plates and strong scattering of the lateral buckles, which increases the light blocking area. It should be noted that unlike the light traveling path through the cut-directed interconnected structure, the optical transparency switch in the plate array through light scattering does not require the deterministic patterning of the phase angles of the buckles via patterned cuts.

The observed switch in optical transparency via buckling of plates adds a new dimension to reversibly “write”, display, and “erase” letters or images within the micro-plates (see Figure 2.14c). As a proof-of-concept, I design the discrete hydrogel micro-plates as shown in Figure 2.14c and 2.14d. SEM image in Figure 2.14d shows the symmetric cuts between the two neighboring micro-plates and the distance between cuts $l = \lambda$. The straight plates with patterned cuts are in a centered rectangular arrangement and disconnected in both horizontal and vertical directions to cut off conduction. The discrete plate design is “pluripotent” to the extent that it could be buckled to display any pattern or any shape of conductive pathways depending on how the swelling or buckling is introduced locally, and then be erased to display a new pattern or conductive pathway. Here, I choose the letter “N” with contacts in the vertical and oblique paths and letter “S” with curved contact paths to demonstrate the “pluripotency” of our method. The hydrogel micro-plate array is placed on a black background to enhance the optical contrast. For display, each buckled micro-plate plays the role of one display pixel, and each pixel possesses at least two contact points to ensure connections between the plates (Figure 2.14e).

A tissue paper in the shape of letter “N” or “S” was soaked with pH 4 buffer solution and placed on top of the hydrogel micro-plate array as a mask to locally swell the hydrogel micro-plates (Figure 2.14c (ii)). After removal of the mask, the letters could be visualized by naked eyes due to the change of transparency in the locally buckled regions (Figure 2.14c (iii) and 2.14e). The non-swollen area remained transparent. The optical image in Figure 2.14e shows the deformed configuration in the oblique segment of letter “N”, where the contacts between the discrete micro-plates through peak-valley are observed as designed. As water evaporated, the buckled micro-plates returned to their original parallel layouts (Figure 2.15), and thus the letters were “erased” (top-right inset of Figure 2.14d). The letters could be re-written and re-erased repeatedly on the array of soft micro-plates. The cycles of switchable swelling and deswelling, correspondingly, letter writing and erasing could sustain ~ 20 times. Further cycling will cause delamination of hydrogels from the glass substrate, which are weakly bonded due to the small contact area between the vertically aligned hydrogel micro-plate and the glass substrate.



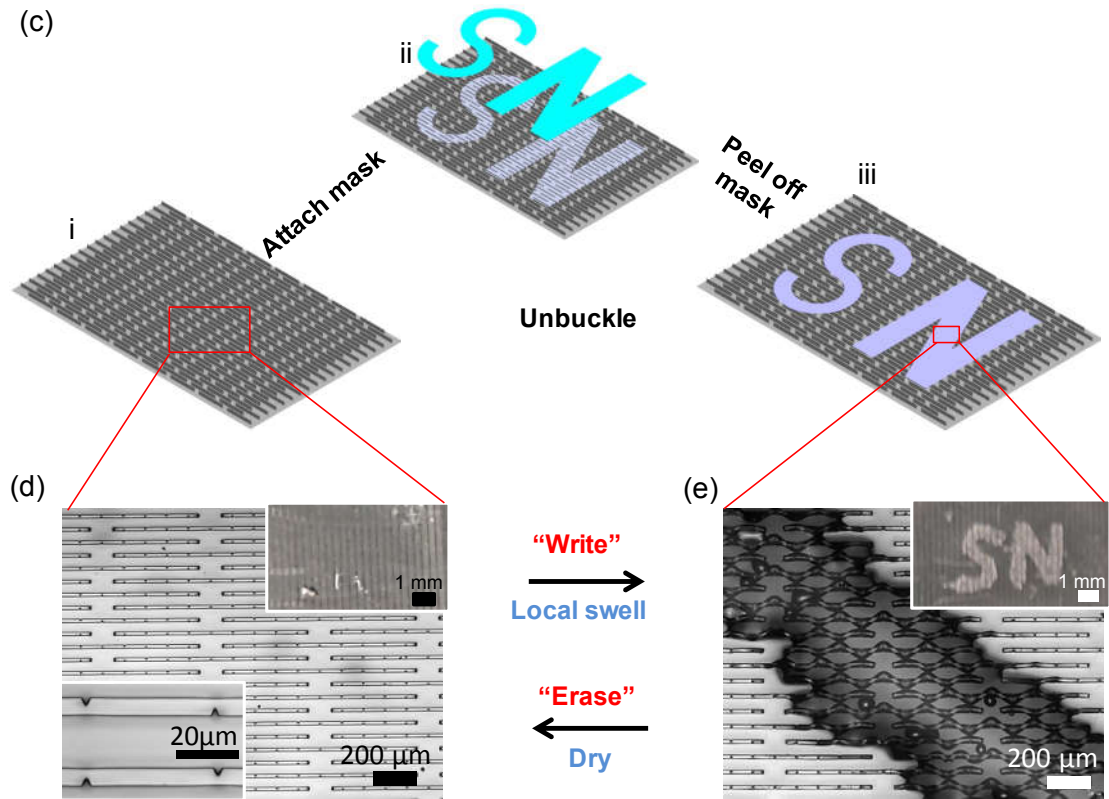


Figure 2.14: Demonstration of cuts-guided peak-valley contacts via directional buckling for multifunctional reconfigurable 1-D mechanical metamaterials with switchable optical properties. (a-b) Reconfiguration of laser light propagation pathways (a) and optical transparency (b) in the hydrogel mechanical metamaterials same as that in Fig. 1f through swelling-induced buckling. (c-e) Schematic illustration of the processes of “writing”, displaying, and “erasing” patterned conductive pathways such as letters “N” and “S” in a centered rectangular arrangement. Letters are displayed through localized buckling in the selective region. (d-e) Experimental demonstration of “writing” and “erasing” letters “N” and “S” with oblique and curved conductive pathways, respectively. (d) Top-view optical images of the layout of the hydrogel mechanical metamaterial before deformation. Bottom-left inset shows the opposite patterned cuts between two neighboring micro-plates; top-right inset shows the optical image of the transparent hydrogel mechanical metamaterial on a black background. (e) Optical image of interconnected oblique pathway through cuts-guided peak-valley contacts in the oblique segment of letter “N” after localized buckling. Top-right inset shows the appearance of letters of “S” and “N” in millimeter size after localized swelling. Upon water evaporation, the buckled regions return to the original state, thus, erasing the displayed letters.

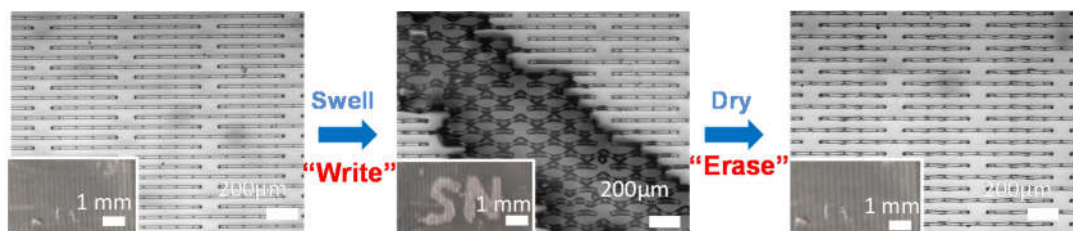


Figure 2.15: Optical images of the reversible buckling of an array of discrete hydrogel micro-plates, leading to the “write” of macroscopic letters upon swelling induced buckling and “erase” of letters upon deswelling.

2.5 Experimental Methods

2.5.1 Fabrication of microstructured hydrogel plates

Photomask of array of parallel stripes with triangular notches on both sides was prepared by Heidelberg DWL66+ laser lithography system (Heidelberg Instruments, Germany). 60 μm thick SU-8 (MicroChem Corp) patterns were fabricated on a silica wafer by photolithography, followed by replica molding to create the PDMS mold. The hydrogel micro-ridges were replica molded from the PDMS mold following the procedure reported in literature.[94] In brief, the hydrogel precursor for molding was prepared in two-steps. First, 200 μL acrylic acid (AA, Sigma-Aldrich), 2 mL 2-hydroxyethyl methacrylate (HEMA, Sigma-Aldrich) (HEMA /AA = 78/14 mol/mol), and 30 μL Darocur 1173 (Ciba Specialty Chemicals) as a photoinitiator were mixed in a vial and ultrasonicated for 30 min. The mixture was then exposed to UV light (365 nm, 97435 Oriel Flood Exposure Source, Newport Corp.) three times at a dosage of 200 mJ/cm^2 each time. Next, an additional 20 μL Darocur 1173 and 40 μL ethylene glycol dimethacrylate (EGDMA, Sigma-Aldrich) as a crosslinker were added into the mixture to form the hydrogel precursor for molding. To mold the hydrogel micro-ridges, 10 μL of the aforementioned hydrogel precursor was cast on a glass slide, and then a PDMS mold

was placed on top of it. The hydrogel precursor was infiltrated into the PDMS mold by capillarity, and crosslinked by UV curing at a dosage of 2 J/cm². After that, the hydrogel film was carefully peeled off from the PDMS mold for the buckling studies.

2.5.2 Swelling-induced buckling

Buckling was induced by constrained swelling of plates. Hexane was used for swelling of macroscale PDMS plates with their bottom surfaces attached to a substrate. The swelling of microscale hydrogel plates is controlled through pH buffer solutions of different pH values. Letter patterned tissue (Kimwipes, Kimberly-Clark Professional) was wetted by pH buffer and then placed on the hydrogel plates arrays surface to induce local swelling through contact.

2.5.3 Sample characterization

The buckled hydrogel films were imaged under optical microscope (Olympus BX61) and by scanning electron microscopy (SEM, FEI Strata DB235) in the dry state. The transmission spectra were acquired by UV-Vis spectrometer (Varian Cary 5000). Diffraction patterns were captured on a white paper using a He-Ne gas laser ($\lambda=633$ nm, 1mW, JDS Uniphase Corp) in a dark room.

2.5.4 Activation of the electrical conductive pathways

The array of macroscopic PDMS plates was replicated from a 3D printed mold. They were then coated with a carbon-based conductive film (Carbon Conductive Grease 846, M.G. Chemicals), powered by a 9 V battery with wired LED lights. To activate the conductive pathway, one sample was stretched using Instron 5944 through contacts

enabled by tension-induced buckling, and another sample was attached to an acrylic thin plate, followed by bending the plate manually.

2.5.5 Finite element method simulation

2.5.5.1 Simulation techniques

Swelling-induced buckling of the hydrogel plates with and without cuts was simulated by considering nonlinear effects of large displacements. The bottom surfaces of plates were securely bonded to a rigid substrate with other surfaces being free. The swelling ratio was assumed to vary from 1.0 to 1.2 throughout the analyses. The contact interaction between the two faces of each cut is set that normal behavior is ‘hard contact’ and tangential behavior is frictionless. First, a buckling analysis was performed using a linear perturbation algorithm. Next, the calculated buckling mode was superposed to the original perfect geometric model as introduced small imperfection. Then a static analysis was performed to capture the post buckling response. The material was modeled as hyper elastic and nearly incompressible Neo-Hookean material.

2.5.5.2 Hyperelastic constitutive model

The classical hyperelastic constitutive model is reviewed here. For many soft materials, linear elastic models can only capture the mechanical behavior in a small strain range (<10%). For large deformation, a hyperelastic constitutive models predict the stress-strain behaviors of soft materials.

The coordinate vector \mathbf{X} of each material particle in the reference configuration was used to name the material particle. Subjected to loads, the material deforms into the

deformed configuration. In the deformed configuration, the material particle \mathbf{X} locates at the place with coordinate vector \mathbf{x} . The deformation gradient tensor is defined by

$$\mathbf{F} = \text{Grad}\mathbf{X} \quad (2.13)$$

Where Grad is the gradient operator with respect to \mathbf{X} . Further denote dV and dv as the volume of a material element in the reference and deformed state, respectively. The change in volume due to deformation is given by $dv=J dV$, where $J= \det \mathbf{F}$. For incompressive material, $J=1$.

With the strain energy density is denoted by $W(\mathbf{F})$, the nominal stress can be defined as

$$\mathbf{s} = \frac{\partial W(\mathbf{F})}{\partial \mathbf{F}} \quad (2.14)$$

Where \mathbf{s} is the nominal stress tensor defined in the reference configuration whose meaning is the current force acting on a reference (undeformed) area. The corresponding Cauchy stress tensor is

$$\boldsymbol{\sigma} = \frac{1}{J} \frac{\partial W(\mathbf{F})}{\partial \mathbf{F}} \mathbf{F}^T \quad (2.15)$$

where $\boldsymbol{\sigma}$ is the true stress tensor defined in the deformed configuration.

The strain energy density of the incompressible Neo-Hookean material is defined as

$$W(\mathbf{F}) = \frac{\mu}{2} [\text{trace}(\mathbf{F}\mathbf{F}^T) - 3] - p(J - 1) \quad (2.16)$$

Where μ is the initial shear modulus and P is a Lagrangian multiplier that imposes the incompressibility condition. The corresponding Cauchy stress can be computed based on equation (2.15),

$$\boldsymbol{\sigma} = \frac{\mu \mathbf{F}\mathbf{F}^T}{J} - p\mathbf{I} \quad (2.17)$$

2.6 Conclusion

I demonstrate deterministic buckling of the array of parallel plates made of responsive soft materials as a new platform to create reversibly reconfigurable electrical and optical pathways. Guided by simple predictive mechanics model and FEM simulation, I design cuts to direct the buckling direction, and thus local contacts selectively. I demonstrate reversible tuning of the functions of the plate arrays, including lighting up the LED and displaying /erasing letters of different shapes, where the abrupt and localized changes can be introduced. Our method is versatile such that the buckling enabled electricity and light propagation pathways can be reconfigured repeatedly and locally. I believe that the *cuts*-guided buckling demonstrated here can be adopted in many stimuli-responsive material systems, including conducting polymers and nanocomposites, hydrogels, shape memory polymers and alloys, in response to heating, light, and electric and magnetic field for a wide range of applications, including metasurfaces, sensors, logic devices, color display, thermal and mechanical loading mitigation, phononic and photonic devices, optoelectronic devices, and micro-fluid channels.

CHAPTER 3 : SELF-SIMILAR HIERARCHICAL WRINKLES AS A POTENTIAL MULTIFUNCTIONAL SMART WINDOW

Note: This Chapter was partially adapted and modified from the publication below:

G. Lin, P. Chandrasekaran, C. Lv, Q. Zhang, Y. Tang, L. Han and J. Yin, “Self-similar hierarchical wrinkles as a potential multifunctional smart window with simultaneously tunable transparency, structural color, and droplet transport”, *ACS Appl. Mater. Interfaces*, 9(31), 26510-26517 (2017)

3.1 Introduction

Buildings account for 20% of the total global energy consumption and 22% of the global carbon dioxide (CO₂) emission[101]. Meanwhile, water use growth has doubled the rate of population increase in the last century. Almost one quarter of the world's population faces the economic water shortage. In the U.S., water use in building is nearly 10% of the total national water use. Therefore, the design of new multifunctional energy efficient and water harvesting materials in building envelopes is highly desired for energy saving, CO₂ emission reduction, and water consumption reduction.

Smart optical materials, which can reversibly switch from transparent to opaque, have immense potential as smart windows for energy-efficient buildings and vehicular applications[102] to save energy and reduce greenhouse gas emissions. The development of such dynamic glazing materials has focused primarily on chromogenic materials and devices such as electrochromic[103] and thermochromic materials[104], which respond to electrical field and temperature, respectively. However, these chromogenic materials often suffer from significant drawbacks related to complicated fabrication processes, cost, durability, and functionality.

Recently, there have been growing research interests in harnessing surface wrinkling at small scales for design of a new class of smart optical materials due to its ease in materials handling, fabrication, and control[64-66, 100, 105, 106]. Wrinkling is a phenomenon often observed in our daily life such as wrinkles in human skin. The wrinkling based optical materials are often mechano-optical materials with dynamically tunable optical properties controlled by simple mechanical strain. The switch from transparent to opaque has been realized by reversibly flattening the light-scattering wrinkled surface micro/nano-topography through mechanical strain[64, 65, 100, 105, 106]. In addition to optical properties, wrinkling has also shown its great promise in realizing a wide range of other tunable surface topography related properties[107], including adhesion[63, 108], wetting[109, 110], friction[111], and anti-biofouling[112].

Structural color has been recently integrated into the design of smart window[65, 66]. Beyond the aesthetics, the structural color is also beneficial for reflecting light in smart window. The structural color arises from the interaction of light with the surface micro/nanostructures rather than their constituent materials properties. Notable examples in nature include the blue structure color in the wings of *Morpho* butterflies[113] and iridescent color in the peacock's tail feather[114]. By integrating tilted micro-pillars on top of wrinkled PDMS, Yang et al., demonstrated an intermediate state of structural coloration between the two switchable states of transparency and opaqueness in a smart window[65]. The success makes one wonder whether it is possible to further combine the switchable opaqueness and transparency with simultaneous structural coloration into one smart optical material.

Meanwhile, water harvesting has attracted increasing research interest to address the issue of the economic water shortage in arid regions[115]. Biological structured surfaces, such as desert beetle's back[116], lizard skin[117], and spider silk or web[118], provide excellent examples and inspirations for biomimic design of high efficient water harvesting materials. How to control the water droplet movement on designed surfaces on demand becomes one of the key issues and challenges[115]. Smart structured surfaces with various chemically or geometrically gradient patterns have been explored in manipulating the water droplet transport[118-121] in response to external stimuli such as temperature, mechanical vibration, and mechanical strain.

Despite the advancement, most studies focus on single properties and functionality of either energy saving or water collection. The versatile applications of wrinkling makes it a promising strategy for design of next generation of multifunctional smart window[64], not only blocking light for energy saving, but harvesting and collecting water from air. By integrating nano-pillars on top of wrinkled poly(dimethylsiloxane) (PDMS), Lee et al., first proposed the concept of a potential multifunctional smart window[64], where both optical transparency and superhydrophobicity can be dynamically tunable via mechanical strain for energy saving and self-cleaning. Similar results on the tunable static wetting or optical properties or combined both via wrinkling were reported in different material systems[106, 122, 123]. However, most studies focus on the static wetting behavior including anisotropic wetting[109] and hydrophilic-hydrophobic transition[110, 123, 124]. Beyond static wetting, the dynamic wetting of how to control the water droplet motion on dynamically

tunable wrinkled surfaces remains untouched, which has important implications for harnessing wrinkling for water harvesting.

In this chapter, I propose harnessing hierarchical wrinkling for design of a potential multifunctional smart window with simultaneously dynamically tunable optical properties and controllable water droplet transport. I apply the simple sequential wrinkling strategy[8, 125] to generate self-similar hierarchical surface topographies on plasma-treated PDMS elastomer with their features ranging from nanoscale/(sub)micron to microscale. Compared to previous studies of hierarchical wrinkled patterns lacking self-similarity[122-124], the self-similarity in each hierarchical level can provide a better control of their hierarchical features. Such hierarchical features are often found in nature such as lotus leaf[126], butterfly wing[127], and gecko foot[128] to provide multifunctional properties of interest. Despite the fact that the generation of similar hierarchically wrinkled patterns was reported before[32], the underlying mechanism governing the formation and evolution of self-similar hierarchical wrinkles has yet to be identified and quantified, and hence the predictive design of self-similar hierarchical surface topographies remains a challenge. In addition, how the dynamically tunable hierarchical features determine both optical properties and droplet motion remains largely unexplored.

Different from previous reported tunable optical materials[64-66, 100, 105, 106], I find that our hierarchically wrinkled PDMS elastomer can reversibly switch from the strain-released opaque state to strain-stretched transparent state accompanied by the non-vanishing exhibited tunable iridescent structural color. The mechanism underpinning the observed phenomenon was revealed through combined experimental measurements,

theoretical modeling, and numerical simulation. In addition to demonstrating control over the combined tunable opaqueness and iridescent structural color, I also demonstrated its multifunctionality in manipulating the water droplet movement on demand controlled by applied strain. The controllable movement of water droplets on wrinkled surface could find potential applications in water harvesting systems.

3.2 Generation of Different Self-similar Hierarchical Wrinkles

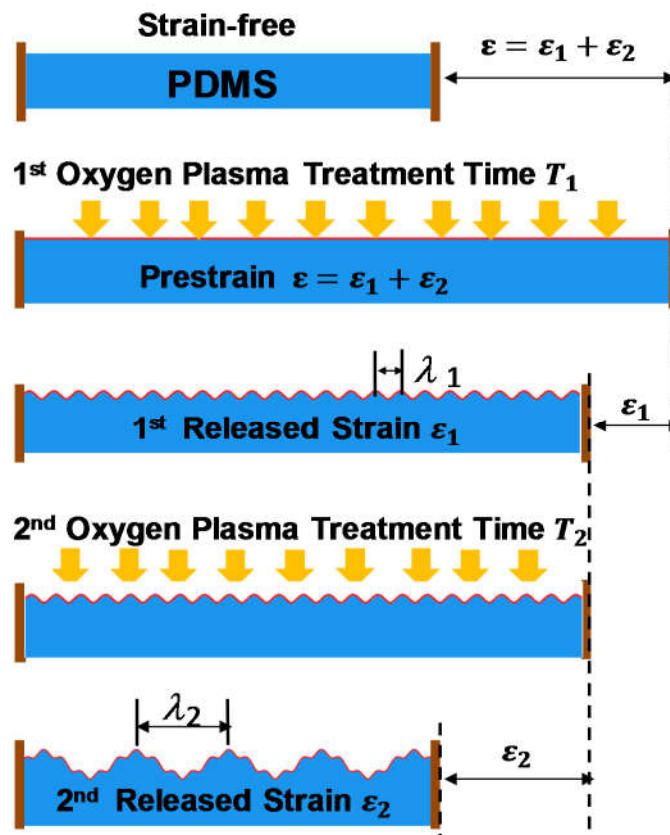


Figure 3.1: The schematic illustration for the fabrication process of generating hierarchical wrinkles on PDMS through two-step strain release and two-step oxygen plasma treatment.

Figure 3.1 shows the fabrication process of hierarchical wrinkles. In the first step, a thin sheet of PDMS substrate with thickness of $\approx 2\text{mm}$ is initially pre-stretched uni-

axially to a strain of $\mathcal{E}_{\text{pre}} = \mathcal{E}_1 + \mathcal{E}_2$ and followed by a first time oxygen plasma treatment for a short time T_1 , typically several minutes. This creates a thin stiff layer of amorphous silica on the PDMS substrate. Then the plasma treated PDMS substrate is partially released for the first time with a strain of \mathcal{E}_1 to generate small single-period wrinkles. Their wavelength λ_1 is typically several hundred nanometers. In the second step, the wrinkled PDMS is further treated with oxygen plasma for a second time with a longer time T_2 ($T_2 > T_1$) to create a thicker silica layer than that generated in the first step, followed by the complete release of the pre-stretched strain, i.e. a strain of \mathcal{E}_2 . This leads to the formation of hierarchical wrinkles, which are created by superposing small wrinkles generated in the first step on large wrinkles (wavelength of λ_2 on the order of several microns) generated in the second step. Through different combination of sequential release of pre-stretched strain (\mathcal{E}_1 and \mathcal{E}_2) and plasma treatment time (T_1 and T_2), a variety of hierarchical wrinkles can be generated.

Figure 3.2 shows the scanning electron microscopy (SEM) images of a family of generated hierarchical wrinkles via simple two-step sequential release of pre-strained PDMS elastomer and multi-step oxygen plasma treatment). It shows hierarchically wrinkled surfaces with different large to small wave number ratios, which is defined as the wavelength ratio of small wrinkles to large wrinkles. The wave number ratio represents the number of small wrinkles rested on top of a large wrinkle. For example, for a wave number ratio of 1:3, one large wave has 3 small waves on top of it (Figure 3.2a(i)). By shortening the 1st time or elongating the 2nd time plasma treatment time, hierarchical wrinkles with smaller ratios, i.e. more small waves on top of a large wave, can be generated (Figure 3.2a(ii-iv)). The hierarchical wrinkles exhibit features ranging from

nanoscale/(sub)micron to microscale, where the small wrinkles have a wavelength of 400nm~950nm and the large wrinkles have a wavelength of 3 μ m~5 μ m. The three-dimensional (3-D) atomic force microscopy (AFM) imaging of the hierarchically wrinkled surface topography with a wave number ratio of 1:4 is shown in Figure 3.2b. Its cross-sectional profile shown in Figure 3.2c demonstrates that the hierarchical wrinkles are highly asymmetric, where about 4 shallow small waves with average amplitude of \approx 125 nm rested on the mountain of one large wave, while only 1 deeper small wave rested in the valley with average amplitude of \approx 345 nm. This is in sharp contrast to the normal symmetric single-period wrinkles without hierarchy.

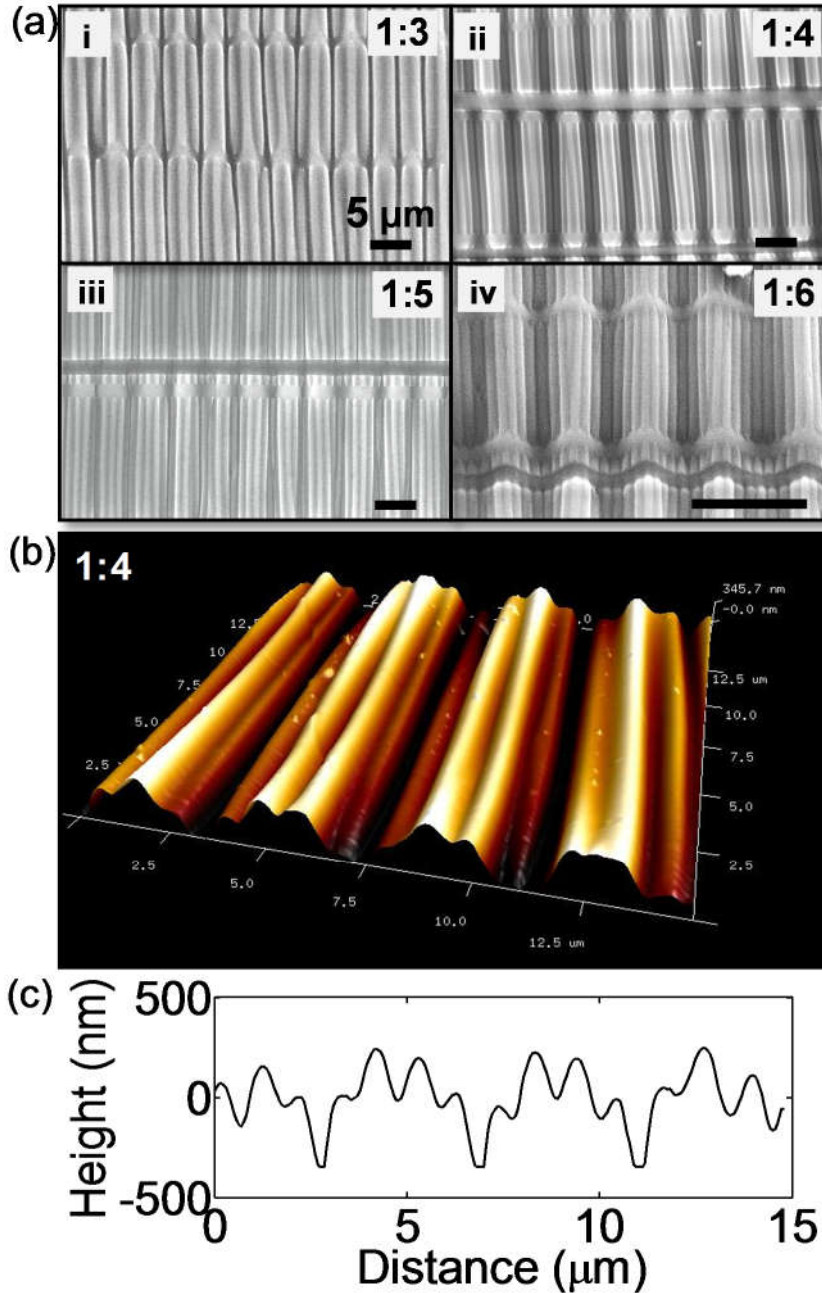


Figure 3.2: (a) SEM images of hierarchical wrinkles with different large to small wave number ratios generated on a pre-strained PDMS elastomer ($\epsilon_{pre} = \epsilon_1 + \epsilon_2$) through sequential strain release of ϵ_1 first and ϵ_2 second and two-step oxygen plasma treatment with time of T_1 and T_2 . (i) 3 small waves on top of one large wave, i.e. ratio of 1:3, generated with $(\epsilon_1, T_1, \epsilon_2, T_2) = (25\%, 360s, 25\%, 3000s)$, (ii) ratio of 1:4 with $(25\%, 270s, 25\%, 3000s)$, (iii) ratio of 1:5 with $(25\%, 200s, 25\%, 3000s)$, and (iv) ratio of 1:6 with $(25\%, 120s, 25\%, 2400s)$. Scale bar is $5\mu m$. (b) AFM 3D image of hierarchical wrinkles with a ratio of 1:4 with cross sectional profile shown in (c).

3.3 Tunable Optical Transparency and Non-vanishing Structural Color

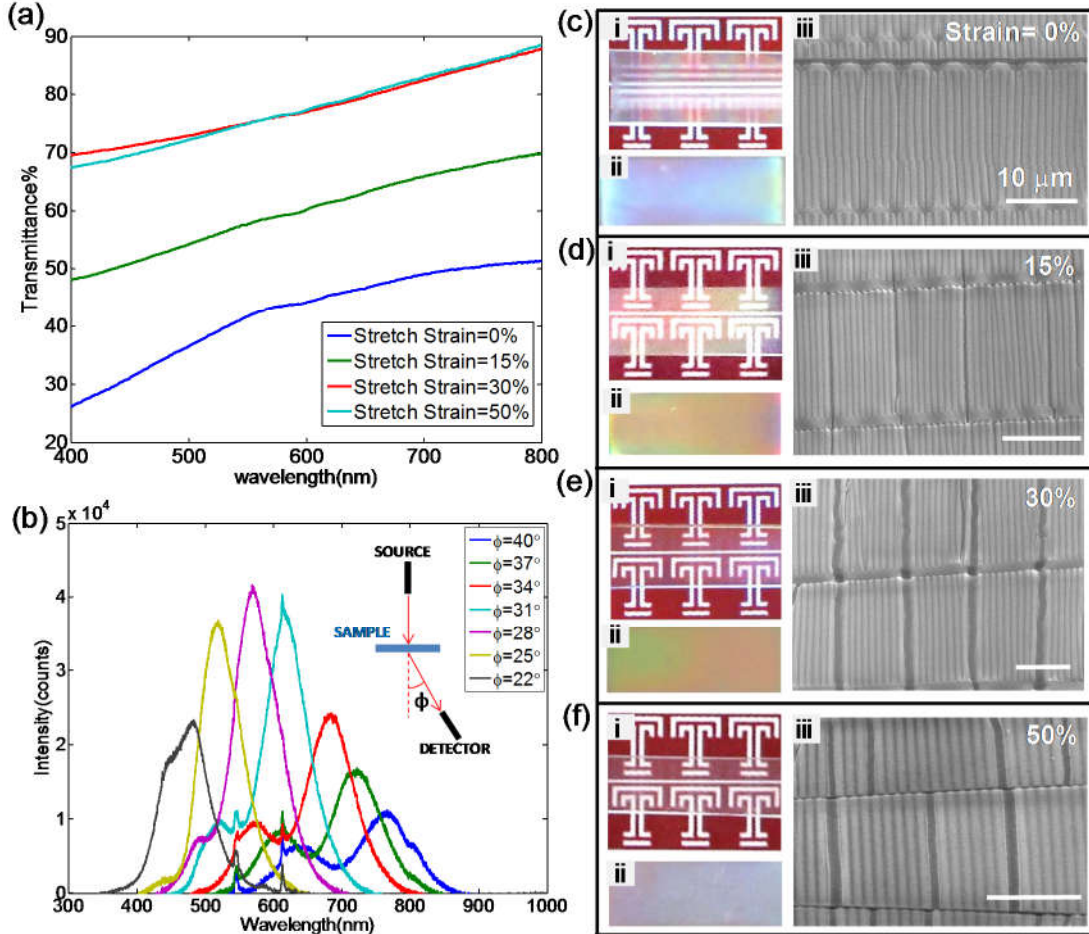
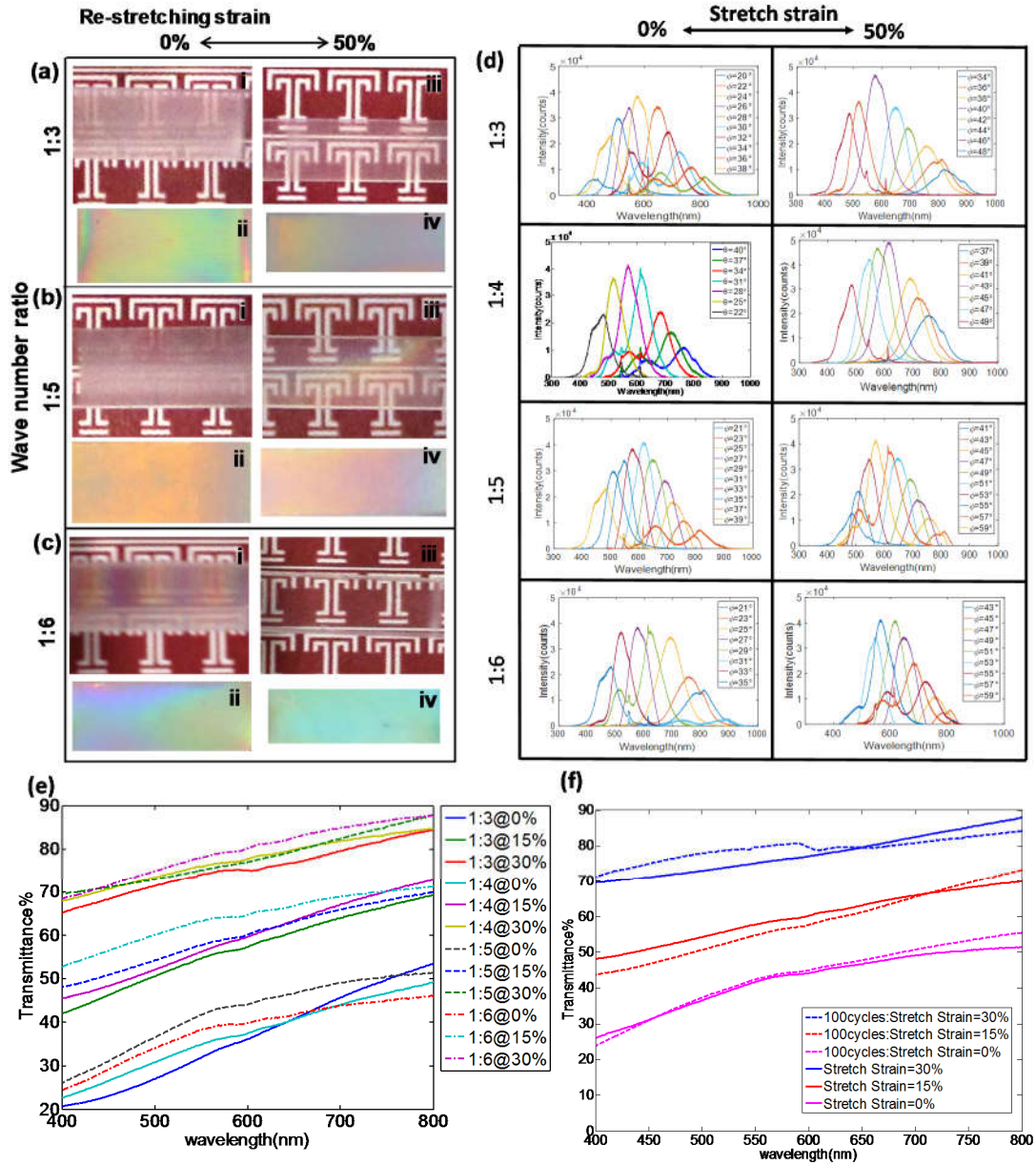


Figure 3.3: (a) Tunable transmittance of a hierarchically wrinkled PDMS elastomer (ratio of 1:4) with different levels of applied stretching strains. (b) Intensity spectrum of the wrinkled elastomer at different angles with the applied stretching strain of 0%. (c-f) the corresponding optical images showing the transparency (i) and structural color (ii) at a fixed angle of 30° and SEM images (iii) at different stretching strain of 0%, 15%, 30%, and 50%. Scale bar is 10 μm .

The switchable transmission of the hierarchically wrinkled PDMS with applied strains was characterized by UV-vis spectrophotometry. Figure 3.3a shows the measured optical transmittance of the sample with a wave number ratio of 1:4 over the visible light spectrum at different levels of applied strain 0% (without stretching), 15%, 30%, and 50% (fully re-stretched). At 0% strain, *i.e.* the hierarchically wrinkled state, it not only

appeared opaque (Figure 3.3c(i)) but displayed angle dependent iridescent structural color (Figure 3.3c(ii), viewed at an angle of 30°), arising from the Bragg diffraction from the periodic wavy structure (Figure 3.3c(iii)). The diffraction of the light can be characterized by the transmitted intensity spectrum (Figure 3.3b), which was measured from different angles ϕ using a custom-built spectrophotometer with two optical fibers arranged in the way shown in the inset of Figure 3.3b. The peak of the spectra shifted at various measurement angles, indicating the angle dependency of the structural color. The iridescent color can be observed from 22° to 40° with the exhibited spectral peaks. Similar combinations of opacity and iridescent color were also observed in all the other hierarchically wrinkled surfaces with different wave number ratios (Figure 3.4(a)-3.4(c)).



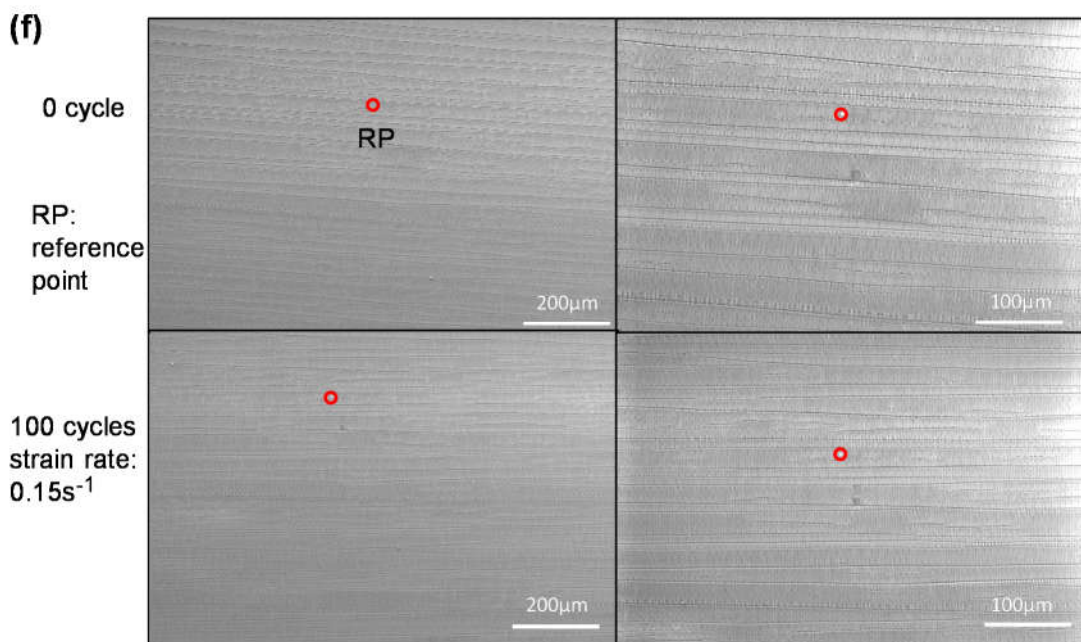


Figure 3.4: The combined tunable optical transparency and structural color of hierarchically wrinkled PDMS elastomer with different wave number ratios with mechanical strains (the initial pre-stretched strain was set to be 50% for all samples). (a-c) The optical images of samples with different wave number ratio (1:3 for (a), 1:5 for (b), and 1:6 for (c)) show the combined opacity (i) and iridescent structural color (ii) at stretching strain of 0%, as well as the combined transparency (iii) and iridescent structural color (iv) at stretching strain of 50%. The optical images for structural color were taken at a fixed angle of 30° . The remained structural color was observed in all the samples after re-stretching to their initial pre-stretched strain of 50%. (d) Intensity spectrum of the wrinkled elastomer at different angles with the applied stretching strain of 0% and 50% for different wave number ratios. (e) Corresponding measured tunable transmittance of the samples at different levels of applied stretching strains from 0% to 30%. (f) The comparison of the measured tunable transmittance of the sample with wave number ratio of 1:4 before and after 100 cycles of mechanical strain stretch and release at different strains. (g) The corresponding large-area SEM images at the same spot before and after 100 cycles with a strain rate of $0.15s^{-1}$.

Figure 3.3a shows that the optical transmittance increased with the applied strain. Correspondingly, the sample switched from opaque with an average transmission of 40% at 0% strain (Figure 3.3c(i)), to translucent with an average transmission of 60% at 15% strain (Figure 3.3d(i)), and to almost transparent with an average transmission of 80% at 30% strain (Figure 3.3e(i)). Further increasing the applied strain from 30% to the initial

pre-stretched strain of 50% (Figure 3.3a) showed a negligible change on the optical transmittance. Meanwhile, the iridescent color was always observed with reduced color intensity throughout the stretching process (Figure 3.3c(ii)-3.3e (ii)). Surprisingly, the iridescent color did not disappear even when it was stretched to its original pre-stretched strain of 50% (Figure 3.3f(ii)), which can be observed from 37° to 49° as indicated by the intensity spectrum in Figure 3.4d. Similar phenomenon of increased transmittance with the applied strain (Figure 3.4e) and non-vanishing iridescent color was also observed in other hierarchically wrinkled samples with different wave number ratios (Figure 3.4(a)-3.4(d)). This is in sharp contrast to the intermediate color state in the hierarchical pillar structures on wrinkles[65], where three states between transparent, colored, and opaque were switched.

To better understand the observed combined transparency and structural color, I conducted an in-situ measurement of the SEM images on the surface topographies at different levels of applied strain (Figure 3.3c(iii)-3.3f(iii)). It showed that as the applied strain increased, the large wrinkles became flattened first, as indicated by the increased periodicity (Figure 3.3e(iii)), leading to the increase of optical transmittance with a reduced scattering of light, while the small wrinkles were not smoothed and remained even when it was stretched to its original pre-stretched strain (Figure 3.3f(iii)). The light diffraction from the remained small wrinkles accounted for the still observed iridescent structural color. The deformation in the small wrinkles was locked by the residual stress during the two-step plasma treatment after a sequential release. This is in stark contrast to the disappearing features of wrinkles through one-step strain release[107]. When the applied stretching strain was fully released, it returned to opaque with color. After 100

cycles of strain releasing and re-stretching with a high strain rate of 0.15s^{-1} (an applied or released strain of 15% per second), the average optical transmittance of the sample showed little degradation (Figure 3.4f), demonstrating its repeatability, robustness, and fast response. The transition between opaque/colored and transparent/colored is reversible and repeatable over many cycles. The comparison of SEM images on the same spot before and after 100 cycles shows that the cracks didn't undergo severe propagation (Figure 3.4g), accounting for the little degradation in the optical performance observed in experiments.

3.4 Modeling and Simulation of Hierarchical Wrinkle Formation and Evolution

3.4.1 FEM simulation

I use both finite element method (FEM)-based numerical simulation and theoretical modeling to investigate the deformation mechanism underpinning the formation and evolution of hierarchical wrinkles with applied strains. Figure 3.5 shows the numerical results on simulating the process of generating hierarchical wrinkles through sequential release of a pre-stretched strain of 34%, as well as the surface topography evolution during the re-stretching process. The modeled soft substrate with a thin layer of stiff coating was initially compressed from Position C to B to simulate the first released strain of 17% (Figure 3.5(i) and (ii)), which generated single-period wrinkles without hierarchy as shown in Figure 3.5(ii). After adding another much thicker layer of stiff coating to simulate the effect of the second time plasma treatment, upon further compressing from Position B to A to simulate the 2nd strain release of 17% (i.e. a fully released state), hierarchical wrinkles were formed with small waves on top of large wrinkles (Figure 3.5(iii)), which is consistent with the experimental observation. Then,

after re-stretching from Position A to B, the large wrinkles disappeared with only the small wrinkles remained (Figure 3.5(iv)). Further stretching from Position B to C (original pre-stretched state), small wrinkles with reduced amplitude still remained due to the observed residual stress on the top interfacial layer from the stress contour shown in Figure 3.5(v). The FEM simulation results well reproduced the experimental observations.

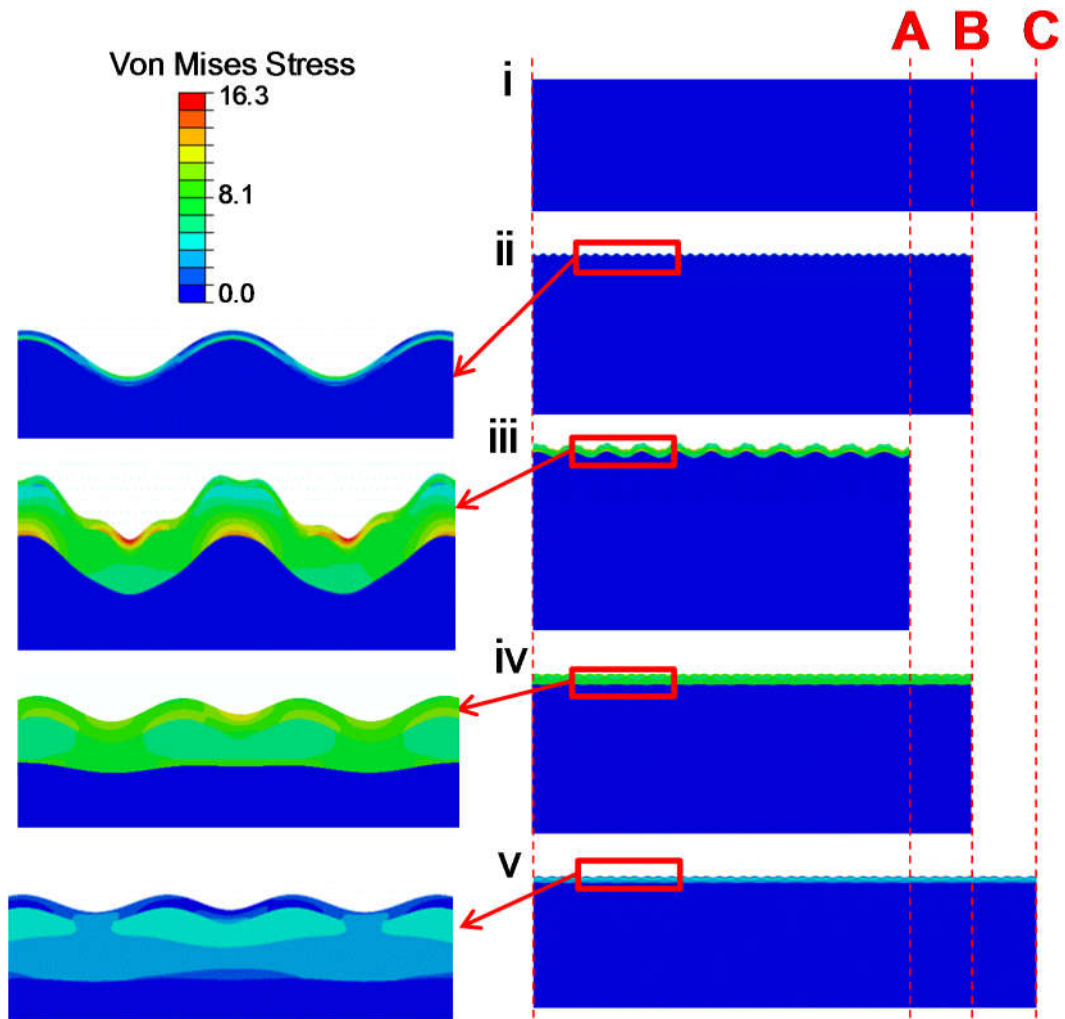


Figure 3.5: FEM simulation on the formation of hierarchical wrinkles through sequential wrinkling (i-iii), as well as the evolution of wrinkles with applied stretching strain (iii-v).

3.4.2 Theoretical model

To better control the formation of hierarchical wrinkles, I developed a simplified theoretical model to predict the geometry of hierarchical wrinkles. The cross-sectional profile of the generated hierarchical wrinkles can be well described by the superposition of two sinusoidal waves at different levels, i.e.

$$y = A_L \sin(2\pi x/\lambda_L) + A_S \sin(2\pi x/\lambda_S) \quad (3.1)$$

where A_L and A_S , λ_L and λ_S are the amplitude and wavelength of the large wrinkles and small wrinkles in the hierarchical wrinkles, respectively. Geometrically, Equation (3.1) shows that the formation of a hierarchical wave shape requires both $\lambda_L > \lambda_S$ and $A_S \neq 0$ otherwise it will reduce to the single-period wave shape without hierarchy when either $\lambda_L = \lambda_S$ or $A_S = 0$ (a case of diminishing small waves). Physically, $\lambda_L > \lambda_S$ requires a longer plasma treatment time in the 2nd step of strain release ε_2 than that in the 1st step of strain release ε_1 , i.e. $T_2 > T_1$. When $T_2 > T_1$ is satisfied, meanwhile, $A_S \neq 0$ requires that another relationship between the two-step strain release ε_1 and ε_2 also be satisfied. The total length of the hierarchical sinusoidal wave is

$$L = \int_0^{\lambda_L} \sqrt{1 + \left(\frac{dy}{dx}\right)^2} dx \quad (3.2)$$

It can also be expressed in terms of critical wrinkling wavelength λ_{L_cr} as

$$L = \lambda_{L_cr}(1 + \varepsilon_1) \quad (3.3)$$

While λ_L and λ_S can also be expressed in terms of λ_{L_cr} as $\lambda_L = \lambda_{L_cr}(1 - \varepsilon_2)$ and $\lambda_S = \lambda_L/n$.

Where n is the number of small wrinkles per large wrinkle. While the amplitude of large wrinkles can be expressed as $A_L = \lambda_{L_{cr}}\sqrt{\varepsilon_2}/\pi$. Solve A_S , we can have the quantitative relationship between λ_S and A_S in the generated hierarchical wrinkle

$$\left(\frac{A_S}{\lambda_S}\right)_{\text{hierarchical}} = \frac{\sqrt{\varepsilon_1 - \varepsilon_1\varepsilon_2 - \varepsilon_2^2}}{\pi} \quad (3.4)$$

In the special case of $\varepsilon_2 = 0$, the two-step strain release will reduce to a single-step strain release, thus Equation (3.4) reduces to $(A_S/\lambda_S)_{\text{single-period}} = \sqrt{\varepsilon_1}/\pi$ [129] for the well-known case of single-period wrinkling without hierarchy, which validates my theory at an extreme case. When comparing $(A_S/\lambda_S)_{\text{single-period}}$ and $(A_S/\lambda_S)_{\text{hierarchical}}$, I find that $(A_S/\lambda_S)_{\text{single-period}} > (A_S/\lambda_S)_{\text{hierarchical}}$. This is consistent with both experimental observation and FEM simulation, where during the formation of hierarchical wrinkles, the amplitude of small wrinkles generated in the 1st-step strain release was observed to decrease while their wavelength was observed to increase during the formation of hierarchical wrinkles in the 2nd-step release of strain.

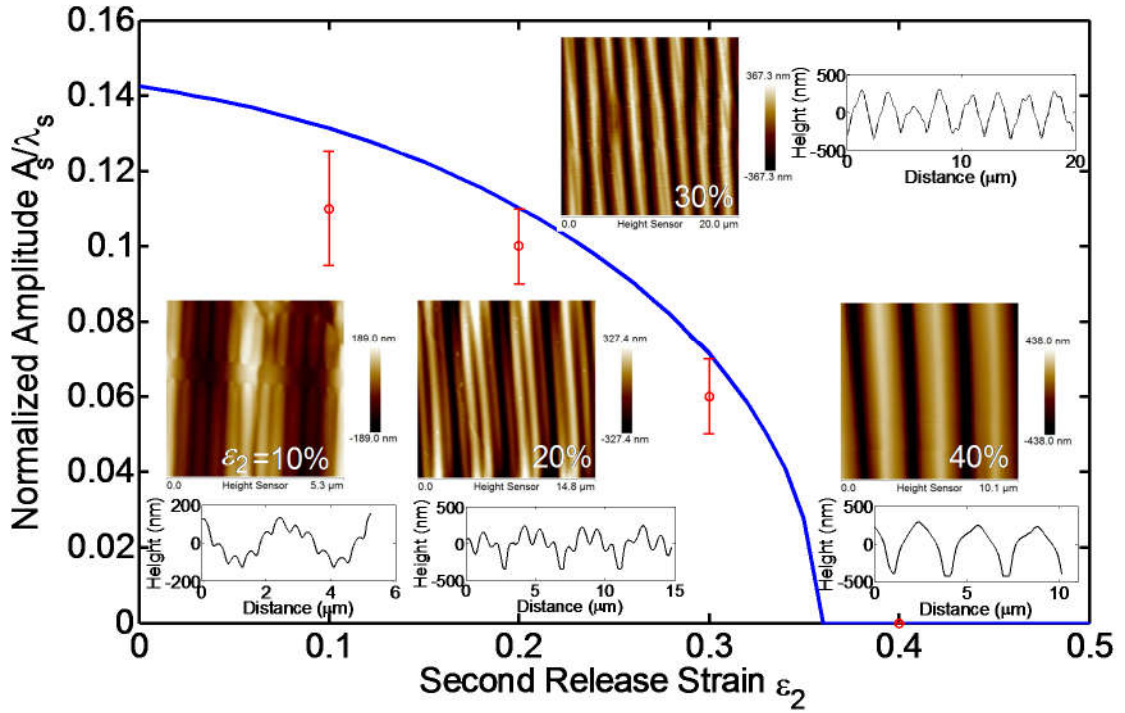


Figure 3.6: Comparison between theory and experiments on the normalized amplitude of the small wrinkles in the hierarchical wrinkles as a function of second released strain ϵ_2 with the first released strain $\epsilon_1 = 20\%$ fixed. Inset: AFM images and cross sectional profiles at different strains of ϵ_2 .

Equation (3.4) is further validated by the corresponding experimental measurements. Figure 3.6 shows the plot of Equation (3.4), i.e. A_s/λ_s as a function of ϵ_2 with a constant $\epsilon_1 = 20\%$. It shows that when ϵ_1 is fixed during the 1st-step strain release (e.g. $\epsilon_1 = 20\%$), an increasing ϵ_2 in the 2nd strain release step will lead to reduced amplitude in the small wrinkles. This is validated by the AFM measurements of the corresponding hierarchical wrinkles generated through two-step strain release in experiments (symbols in Figure 3.6), where ϵ_2 increased from 10% to 30% while ϵ_1 was kept constant as 20%. As seen from the solid curve in Figure 3.6, further increase of ϵ_2

will lead to a zero value of A_S , i.e. the small wrinkles on top of large wrinkles will disappear and thus a single-period wrinkle without hierarchy will be formed despite the satisfaction of $T_2 > T_1$. This is also validated by the corresponding experiment with $\varepsilon_1 = 20\%$ and $\varepsilon_2 = 40\%$, where single-period wrinkles were observed (Figure 3.6). With the validation of Equation (3.4) by experiments, now I can summarize the condition for generating hierarchical wrinkles through two-step strain release under the precondition of $\lambda_2 > \lambda_1$ (or $T_2 > T_1$) as below by satisfying a real value of A_S in Equation (3.4), i.e.

$$\varepsilon_1 > \frac{\varepsilon_2^2}{1 - \varepsilon_2} \quad (3.5)$$

Equation (3.5) provides a straightforward but important theoretical guidance for generating hierarchical wrinkles through sequential wrinkling. When $\varepsilon_1 \leq \varepsilon_2^2 / (1 - \varepsilon_2)$, single-period wrinkles without hierarchy will be preferred through two-step strain release despite the longer treatment time in the 2nd-step release.

3.5 Controllable Water Droplet Transport via Mechanical Strain

In addition to their tunable optical transparency and structural color, I also investigated the multifunctionality of tunable hierarchical wrinkles in dynamically manipulating the water droplet transport on the wrinkled surface through applied strains. The study of controllable water droplet transport on dynamically tunable surface topography with strain will have important implications in water collection[130]. The working mechanism is schematically illustrated in Figure 3.8a: the dynamical change in the undulating surface topography of hierarchical wrinkles with the applied stretching strain will reversibly drive the pinned water droplet to slide under its self-weight. Figure

3.8b demonstrate this ability for a water droplet ($V = 50\mu\text{L}$) transports along the direction perpendicular to hierarchical wrinkles on a tilted PDMS surface (wave number ratio of 1:4). The tilting angle α_t is 45° . To obtain a larger field of view (FOV), the camera was set at an angle of 35° with respect to the sample, showing a captured side view of sample with a tilting angle of 10° in Figure 3.8b. The droplet was initially pinned to the wrinkled surface due to its large roughness despite its hydrophobicity with a static apparent contact angle of about 125° as shown in Figure S4 indicates the droplet is in a Wenzel wetting state[131]. The wetting state of the droplet in Figure 3.8b can be quantitatively calculated following the Wenzel model¹,

$$\cos \theta^* = r \cos \theta_Y \quad (3.6)$$

in which θ_Y is the Young contact angle ^[deGennes] of the droplet ($\theta_Y \approx 110^\circ$ measured on a flat PDMS, as shown in Figure 3.7a), θ^* is the apparent contact angle of the droplet on the rough surface. r is the roughness value, defined as the ratio of the solid-liquid contact area to its projection area. As shown in Figure 3.8, our droplet transport experiments were carried out on the surface with wave number ratio of 1:4. Based on Figure 3.2(c), we can get $\lambda_L \approx 4 \mu\text{m}$, $\lambda_S \approx 1 \mu\text{m}$, $A_L \approx 0.5 \mu\text{m}$ and $A_S \approx 0.3 \mu\text{m}$. Putting these parameters into Equation (3.1), we can obtain the roughness of the surface $r \approx 6.7/4 \approx 1.67$, which leads to $\theta^* \approx 124.8^\circ$ by substituting r and θ_Y into Equation (3.6). The apparent contact angle θ^* estimated using the Wenzel model is well consistent with our experimental measurement ($\approx 125^\circ$, as shown in Figure 3.7b), which suggests that the droplet is indeed in a Wenzel wetting state.

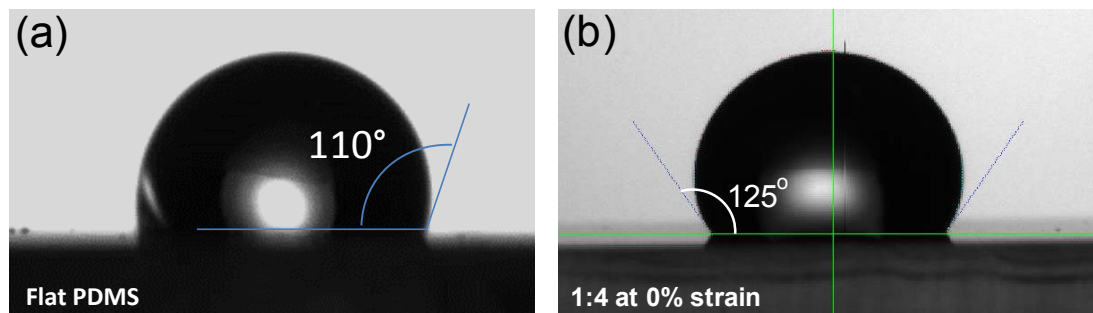


Figure 3.7: The optical images show the Young contact angle ($\sim 110^\circ$) on flat PDMS (a) and the static apparent static contact angle ($\sim 125^\circ$) on hierarchically wrinkled PDMS elastomer (b) with the wave number ratio of 1:4 without further treatment of superhydrophobic coatings, respectively.

When the surface was stretched, the roughness is reduced which weakens the Wenzel effect, so the water droplet started to slide. As soon as the stretched strain was released, the water droplet began to stop and became pinned to the surface (See Figure 3.8). Furthermore, re-stretching the substrate drove the pinned water droplet to slide again, and the moving water droplet became pinned again upon strain release. I verified this transition from pinned to sliding was repeatable through control of cyclic mechanical stretching and release. The changes in the mobility of water droplet correlate with the dynamically tunable surface topographies of hierarchically wrinkled substrates with applied stretching strain. As revealed by the SEM images in Figure 3.3c, the surface with hierarchical wrinkles became nearly flattened with small wrinkle remained after stretching and returned to rough with hierarchy when the strain was released.

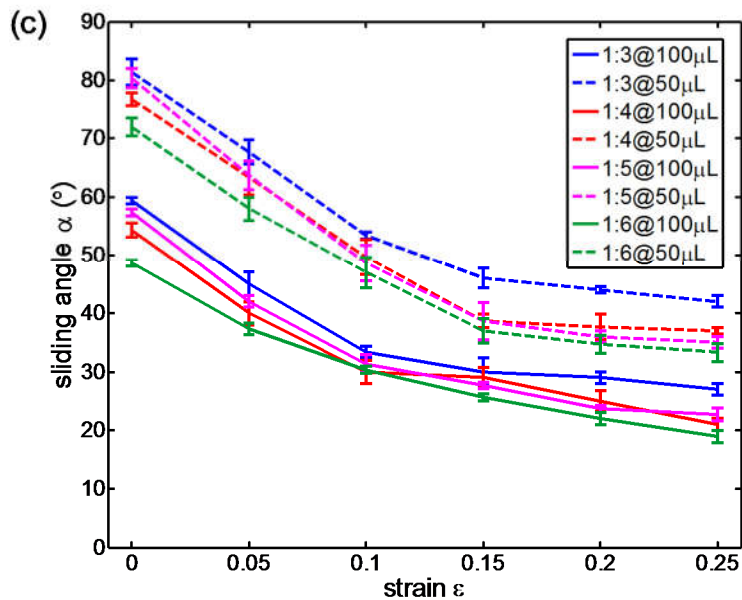
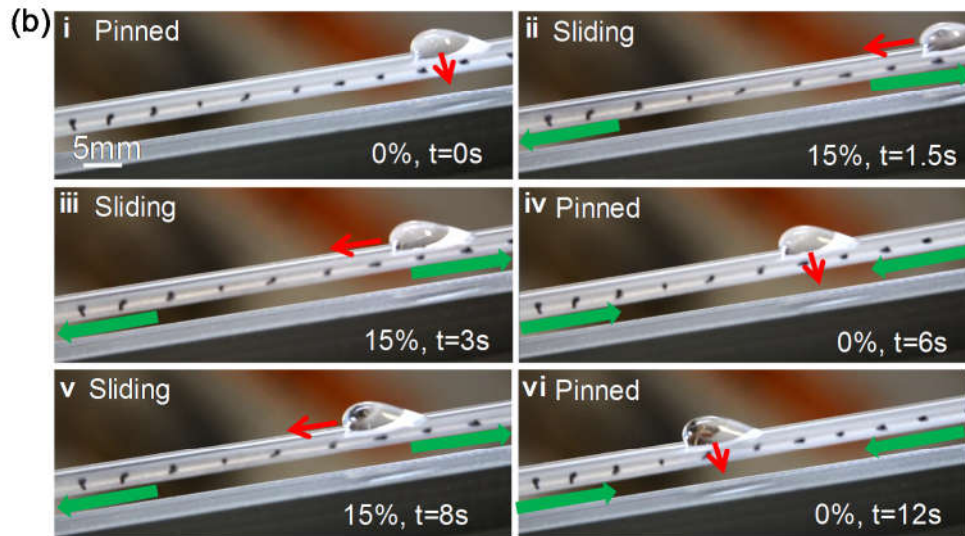
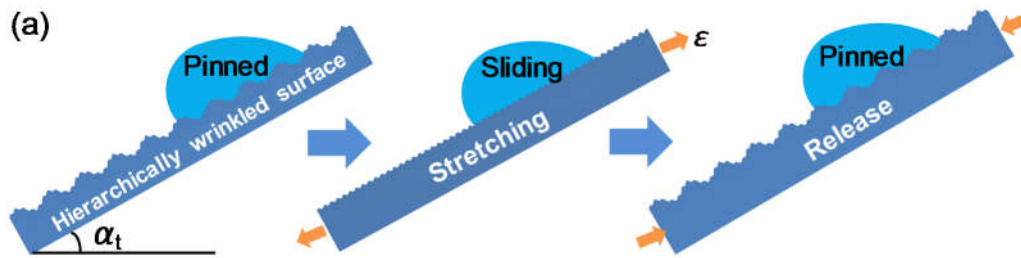


Figure 3.8: (a) Schematic illustration of controlling the motion of water droplets on inclined hierarchically wrinkled surfaces with tilted angle of α_t from pinned to sliding through applied mechanical stretching and release. (b) Corresponding experimental demonstration with optical images taken from a video showing the control of water droplet's movement on an inclined hierarchically wrinkled PDMS surface (tilted angle of

$\alpha_t = 45^\circ$) from pinned to sliding through applied stretching strain, and vice versa through strain release. The camera was set at an angle of 35° with respect to the sample to obtain a larger field of view, showing a captured side view at 10° . (c) Sliding angle α of hierarchically wrinkled PDMS surfaces with different wave-number ratios for different water droplet volumes as a function of applied stretching strain ε .

To better understand the underlying mechanism for the transition from pinned to sliding with the applied strain in the hierarchically wrinkled substrate, I did the simple qualitative analysis as follows. Along the sliding direction (tilting angle is α_t), there are two force components acting on the water droplet: the driving force resulting from the gravity $mgsin\alpha_t$ (downward along the substrate) and the retentive force F (upward along the substrate) resulting from the surface tension and the contact angle hysteresis[131], where m is the mass of the water droplet and g is gravitational acceleration. During the mechanical stretching and release, since the driving force $mgsin\alpha_t$ remains unchanged, the reversible pinned to sliding transition will break the two-force balance, requiring that the retentive force F be a function of strain, i.e. $F = F(\varepsilon)$. F can be indirectly characterized by the sliding angle α defined as the critical tilted angle of the substrate for the droplet to slide. When $\alpha_t = \alpha$, we have $mgsin\alpha_t = mgsin\alpha = F(\varepsilon)$, implying that the sliding angle is also a function of the applied strain ε , i.e. $F(\varepsilon) = mgsin[\alpha(\varepsilon)]$. When $\alpha_t > \alpha$, the driving force $mgsin\alpha_t$ is larger than the retentive force, i.e. $mgsin\alpha_t > F = mgsin\alpha$, driving the droplet to move, otherwise it will be pinned when $\alpha_t < \alpha$.

Knowing this, I systematically investigated the variation of the sliding angle α as the function of the applied strain using different droplet volumes and hierarchically wrinkled substrates with different large to small wave number ratios (Figure 3.8c). As

seen from the red dashed line in Figure 3.8c, the water droplet on the hierarchically wrinkled surface shown in Figure 3.8b corresponds to a sliding angle of about 78° at stretching strain $\varepsilon = 0$, i.e. $\alpha = \alpha(\varepsilon=0) = 78^\circ$. In this case, $\alpha_t = 45^\circ < \alpha = 78^\circ$, leading to the observed pinned to the substrate before stretching (Figure 3.8b(i)). When the substrate is increasingly stretched from 0% to 15%, Figure 3.8c shows that the corresponding sliding angle α is observed to decrease sharply from 78° to 38° due to the reduced surface roughness (i.e. the disappearance of large wrinkles). Since the tilted angle $\alpha_t = 45^\circ$ is fixed, at a critical stretching strain ε_{cs} when the sliding angle decreases to be equal to α_t , i.e. $\alpha(\varepsilon = \varepsilon_{cs}) \equiv \alpha_t = 45^\circ$, the initially pinned water droplet will start to slide. As measured from Figure 3.8c, $\alpha = 45^\circ$ corresponds to $\varepsilon = \varepsilon_{cs} \approx 12\%$. Thus, when the stretching strain ε is increased to be larger than ε_{cs} , i.e. $\varepsilon = \varepsilon_{cs} \approx 12\%$, the droplet starts to slide as observed in Figure 3.8b(ii) since the fixed tilted angle $\alpha_t = 45^\circ$ is larger than the corresponding strain dependent sliding angle α as shown in Figure 3.8c, i.e. $\alpha_t > \alpha(\varepsilon)$. On the contrary, when $\varepsilon = \varepsilon_{cs} \approx 12\%$ during the beginning of stretching or the end of fully release, it will lead to the droplet to stagnate as observed in Figure 3.8b(iv) with $\alpha_t = 45^\circ < \alpha$ as measured from Figure 3.8c. This simple analysis not only unequivocally explains the phenomena I observed in Figure 3.8b, but also is consistent well with our intuition: when the rough surface is stretched, the surface becomes relatively smooth, which reduces the contact line pinning (vice versa), so the balance of the water droplet between gravity and the retentive force is easily broken, thus lead the droplet to transport.

Furthermore, as displayed in Figure 3.8c, for all the studied hierarchically wrinkled samples with wave number ratio ranging from 1:3 to 1:6, we have $\Delta\alpha = \alpha(\varepsilon =$

0%) – $\alpha(\varepsilon = 25\%) \geq 30^\circ$ for both droplets with $V = 50 \mu\text{L}$ and $100 \mu\text{L}$, even at a much narrower strain range from 0% to 10%, I still surprisingly observed a sharp drop of the sliding angle $\Delta\alpha > 25^\circ$. Based on the above experiments and analyses, without loss of generality, I can envision that the pinned-to-sliding transition feature on a hierarchically wrinkled substrate can always happen at a given stretching strain $\varepsilon = \varepsilon_{-1}$ with a tilted angle of the substrate $\alpha_t \geq \alpha(\varepsilon_{-1})$. Thus, Figure 3.8c provides a phase diagram of the large strain range and sliding angle change governed by the strain for manipulating the pinned-to-sliding transition of water droplets, which will provide important potential guidance for design of robust water transport and collection system.

3.6 Experimental Methods

3.6.1 Fabrication of hierarchical surface wrinkling

PDMS precursor (Sylgard 184 from Dow Corning) was mixed with curing agent in 1:10 weight ratio. The mixed liquid PDMS was degassed in a desiccator for 1h, followed by cured at 70°C overnight. PDMS substrate was clamped and stretched uniaxially up to strain of 50% (i.e. $\varepsilon_{\text{pre}}=50\%= \varepsilon_1+ \varepsilon_2$) using a home-made stretching device. The surface was then treated with oxygen plasma (Harrick, model PDC-32G) at a power of 18watts for a short time T_1 ($T_1 = 2\text{-}5$ mins), followed by partially releasing the pre-stretched strain of ε_1 to generate small wavelength wrinkles. Then the wrinkled PDMS substrate was treated for a second time with oxygen plasma for a much longer time T_2 ($T_2 = 30$ mins-1hour) followed by fully releasing the pre-stretched strain to generate the hierarchical wrinkles.

3.6.2 Surface topography characterization

Scanning electron microscopy (SEM) images were taken by FEI Quanta 450FEG in low vacuum mode at an acceleration voltage of 10kV. Tapping mode atomic force microscopy (AFM) imaging was applied to quantify the 3D surface topography of the hierarchical wrinkle structure in ambient conditions using a Dimension Icon (BrukerNano, Santa Barbara, CA) and a nanosized silicon tip (nominal end radius $R \sim 10$ nm, spring constant $k \sim 42$ N/m, NCHV-A, BrukerNano). For each sample, a minimum of 5 different locations were imaged to confirm the repeatability.

3.6.3 Optical property characterization

Spectral transmittance was measured by Agilent Cary 500 UV-Vis-NIR spectrophotometer. Transmitted intensity spectrum was measured by a custom-built device with a fixed light source fiber normal to sample surface and a rotational detective fiber.

3.6.4 Contact angle and sliding angle measurement

The contact angles measurement were taken with ramé-hart Model 260 Standard Contact Angle Goniometer at ambient temperature. A 5 μ L liquid droplet was used in all contact angle measurements. The sliding angle was measured with a custom-built rotational sample stretcher.

3.6.5 Finite element method simulation

Finite element method was used to simulate and mimic the formation and evolution of hierarchical wrinkles through sequential wrinkling. A bilayer model of stiff thin film (silica-like layer[132, 133]) on soft substrate (PDMS) under compression

controlled by displacement is used to simulate the generation of small wrinkles after the 1st time plasma treatment and strain release. For simplicity, considering the relatively small applied strain, both stiff coating and substrate are modeled as isotropic and linear elastic material without considering the nonlinear deformation in the elastomer[32, 38, 134] and are represented using 2-D plane strain elements. In the simulation, for the first treatment time of $T_1=270$ s, the Young's modulus of the silica-like layer E_f and PDMS substrate E_s takes the value of $E_f=0.4$ GPa[132, 133] and $E_s=2$ MPa[135], respectively. The Poisson's ratio for both silica-like layer and PDMS substrate are the same with a value of 0.49[132]. The thickness of the silica-like layer t_1 is estimated to be $t_1 \approx 39$ nm from its measured wavelength of $\lambda_1 \approx 1\mu\text{m}$ in terms of equation of $t_1 = (\lambda_1/2\pi)(3E_s/E_f)^{1/3}$ [132, 133]. During the second time plasma treatment with a much longer time ($T_2=3000$ s), the oxygen plasma continued to gradually convert PDMS into a much thicker silica-like layer from the surface[136]. For simplicity, I assume that the modulus of 2nd time treatment layer remained unchanged. Similarly, after a single treatment time of $T=3000$ s, the corresponding layer thickness is estimated to be $t_2 \approx 136.5$ nm from the measured wavelength of single-period wrinkles ($\approx 3.5\mu\text{m}$). To simulate and mimic the effect of 2nd time prolonged plasma treatment, the total thickness of the stiff coating layer was increased to ≈ 175.5 nm (i.e. $t_1 + t_2$) in the simulation by modifying the material properties of its underlying connecting thin layer of soft substrate to be the same as the stiff coating. Upon further compression to simulate the 2nd-step release, hierarchical wrinkles were generated. First, a buckling analysis was performed using a linear perturbation algorithm. Next, the calculated buckling mode was superposed to the original perfect geometric model as introduced small imperfection. The post-buckling

response was captured through dynamic explicit simulations, which were performed under quasi-static conditions ensured by monitoring the kinetic energy. A Matlab code was developed in order to apply periodic boundary condition (PBC) to the left and right boundaries of simulated wrinkling sample (Appendix A). PBC set the x and y displacements of the nodes on left and right boundary identical to simulate an infinite long sample and thus eliminate the boundary effect.

3.7 Conclusion

In conclusion, I present a hierarchical wrinkle-based multifunctional smart window by harnessing the dynamic tunability of wrinkled surface topographies on oxygen plasma treated PDMS elastomer. The multifunctional smart window could not only reversibly switch from transparency to opaqueness with displayed non-vanishing iridescent structural color, but dynamically manipulate the mobility of water droplets from pinned to sliding on their surface for potential water harvesting through mechanical stretching and release. I envision that the sequential wrinkling strategy for generating dynamically tunable hierarchical wrinkles can be readily extended to other responsive materials systems such as liquid crystals elastomer and shape memory polymers in response to temperature or light, as well as other coatings through sequential depositions. The hierarchical wrinkle-based smart materials could also find other potential applications in tunable optics, display encoding, tunable structural color change for camouflage, water condensation, and design of slippery surface.

CHAPTER 4 SMALL DEGREE OF ANISOTROPIC WETTING ON SELF-SIMILAR HIERARCHICAL WRINKLED SURFACES

Note: This Chapter was partially adapted and modified from the publication below:

G. Lin, Q. Zhang, C. Lv, Y. Tang and J. Yin, “Small degree of anisotropic wetting on self-similar hierarchical wrinkled surfaces“, *Soft Matter*, 14, 1517-1529 (2018)

4.1 Introduction

Hierarchical surface structures which have multiscale roughness from the nanoscale to the macroscale are often found in nature to provide extraordinary properties, such as non-wettability and self-cleaning in lotus leaves[137], strong adhesion in gecko’s feet[138], and structural color in butterfly wings[139]. Fascinated by these intriguing properties, researchers have devoted great efforts to reproduce the functionalities by mimicking these biological hierarchical surface structures through a variety of fabrication methods, including replica molding[140], etching[141], lithography[142], chemical deposition[143], and colloidal assembly[144].

Due to its ease in materials handling, fabrication, and control[64, 65], surface wrinkling has attracted growing research interest in the past two decades and has been proven to be a facile approach to generate various controllable surface topographies with dynamic tunability and multifunctionality[17, 18, 33, 145-147], including but not limited to adaptive hierarchical surfaces[32, 134] with dynamically tunable properties in wetting and optics[64, 65, 122]. Among them, Efimenko et al. first demonstrated the formation of nested, hierarchical wrinkled surfaces on oxidized poly(dimethylsiloxane) (PDMS) elastomers under high compressive strain[32]. By coating gold film on highly pre-strained elastomer, Cao et al. generated high-aspect-ratio hierarchical ridged surfaces

with both tunable wetting and optical properties controlled by simple strain[122]. Structured hierarchical wrinkled surfaces have also been achieved by integrating micro/nano-structures (e.g. pillars or particles) onto single-period micro-wrinkled elastomers [64, 65, 110, 148], which exhibited similar switchable wetting and/or optical behavior. Very recently, based on the sequential wrinkling strategy[149], I have successfully fabricated multiscale self-similar hierarchical wrinkled surfaces on plasma treated PDMS elastomer with their surface features crossing from nanoscale (wrinkles with wavelength of 400-950nm) to microscale (wrinkles with wavelength of 3-5 μ m)[150]. Such multiscale self-similar hierarchical wrinkles have demonstrated unique performances in tunable optical properties and controllable droplet motion[150].

Meanwhile, anisotropic wetting is a fascinating feature on natural and engineered anisotropic patterned surfaces, which has attracted researchers' interest for decades due to its potential application in directional water transport and water collection[126]. Intriguing examples in nature include directional flow in a rice leaf and Namib desert grass[151], as well as radial water shedding in butterfly wing from its body center[152]. The anisotropic wettability can be achieved by either heterogeneous chemical patterning or anisotropic surface morphology or combined both. Chemically, through line-patterned hydrophobic/hydrophilic area, researchers have demonstrated the tunability in anisotropic wetting by adjusting the line width and interval[153-156]. Physically, anisotropic wetting can be realized by engineering surfaces with anisotropic morphological features. Theoretical studies of anisotropic wetting properties on various shapes of parallel grooved microstructures showed that the wetting anisotropy strongly depends on the specific topographical features and wetting state[157].

As one of the highly anisotropic structures, studies have demonstrated the dynamically tunable anisotropic wetting of wrinkles through mechanical stretch strain. Chung et al. first studied the tunable anisotropic wetting on single-period micro-wrinkled surfaces through simple mechanical strains[109]. They showed a transition from isotropic (flat) to anisotropic wetting (micro-wrinkled) through strain-controlled wrinkling, where the difference of the contact angles between two orthogonal directions could reach 50°. Lee et al. studied the anisotropic wetting on wavy surfaces covered with nanoparticles, similar to the structure of the rice leaf surface[158]. They showed that by increasing the roughness of nanoparticle layer on the wrinkled elastomer, the dynamic wetting behavior transited from anisotropic/pinned to anisotropic/rollable, and to isotropic/rollable state.

Despite the advancement, the experimental study and theoretical understanding of anisotropic wetting behavior and wetting state on hierarchical wrinkled surfaces still remain largely unexplored[109, 159]. Compared to single-period micro-wrinkles, how the structural hierarchy in multiscale wrinkled surfaces influences their wetting state and anisotropic wetting behavior alongside its underlying wetting mechanism is largely unknown. Several theoretical studies on the wetting property of multiscale hierarchical wrinkled surfaces predict the possibility of forming superhydrophobic surfaces by optimizing the geometrical parameters of wrinkles at each hierarchical level[160, 161], however, it remains to be examined experimentally.

In this chapter, I focus on the self-similar hierarchical wrinkled surfaces. Compared to most previously studied wrinkling-based hierarchical structured surfaces without self-similarity, including pillars on wrinkles[64, 65], particles on wrinkles[158], and grooves on wrinkles[124], the self-similar wrinkled surface structure presents the

most anisotropic morphological characteristics[156]. Furthermore, the self-similarity could provide a better control of the hierarchical features in each level, as well as an idealized model system for examining related developed theoretical models. Here, I extended our recent study of sequential wrinkling[150] to generate self-similar hierarchical wrinkles with one order higher multiscale hierarchy crossing from hundreds of nanometers to tens of microns, and explored their potential anisotropic wetting behavior through both experimental and theoretical analysis. I first discuss the tunable geometrical dimension in multiscale hierarchical wrinkles by manipulating the treatment time, as well as investigated its effect in the wetting anisotropy of hierarchical wrinkled surfaces. I examine the possible wetting state of the tunable multiscale hierarchical wrinkled surface through both surface free-energy based theoretical models and experimental confocal imaging visualization. Then I analyze the observed anisotropic wetting behavior through the developed theoretical model by calculating the free energy change during the three-phase contact line moving, as well as experimental examination. I conclude with some remarks on the competition between wrinkles and orthogonal cracks in line pinning in determining its anisotropic wetting behavior of a hierarchical wrinkled surface.

4.2 Experimental Methods

4.2.1 Generation of hierarchical wrinkled surfaces

A hierarchical wrinkled surface with a larger multi-scalability crossing two hierarchical levels is fabricated by sequential plasma and UVO treatment of the PDMS substrate. Figure 4.1 shows the schematics on the fabrication process of PDMS samples with hierarchical surface wrinkles by following two sequential steps. In the 1st step, a thin

sheet of PDMS substrate with thickness of $\approx 2\text{mm}$ is initially pre-stretched uni-axially to a strain of $\varepsilon_{\text{pre}} = \varepsilon_1 + \varepsilon_2$ using a home-made stretching device, followed by oxygen plasma treatment (Harrick, model PDC-32G) at a power of 18 watts for time T_1 (about 4-10 minutes). This creates a thin stiff layer of amorphous silica on the surface of the PDMS substrate. Then the plasma treated PDMS substrate is partially released for the first time with a strain of ε_1 to generate level-1 sub-micron wrinkles λ_1 (typically several hundred nanometers). In the 2nd step, the wrinkled PDMS is further treated with UVO (Jelight, model 18) for a second time with time T_2 (about 30-60 minutes) to create a much thicker silica layer than that generated in the 1st step, followed by the complete release of the pre-stretched strain, i.e. a released strain of ε_2 . This leads to the formation of hierarchical wrinkles with a much higher multi-scalability crossing each level, where level-1 sub-micron wrinkles generated in the 1st step are superposed on the level-2 micro-wrinkles (λ_2) generated in the 2nd step (λ_2 is on the order of tens of microns, rather than few microns through plasma treatment).

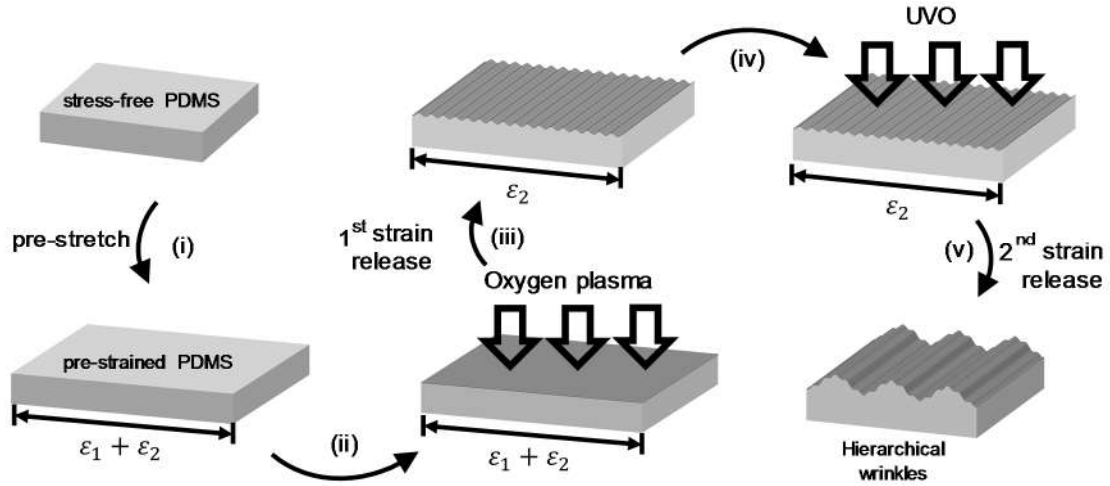


Figure 4.1: Schematics of the process of generating multiscale self-similar hierarchical wrinkles on PDMS elastomers through combined plasma and UVO treatment and two-step strain release.

4.2.2 Surface topography characterization

Scanning electron microscopy (SEM) images were taken by FEI Quanta 450FEG in low vacuum mode at an acceleration voltage of 10kV. Tapping mode atomic force microscopy (AFM) imaging was applied to quantify the surface 3D topography of the level-1 sub-micron wrinkled structure in ambient conditions using a Dimension Icon (BrukerNano, Santa Barbara, CA) and a nanosized silicon tip (nominal end radius $R \sim 10\text{nm}$, spring constant $k \sim 42\text{ N/m}$, NCHV-A, BrukerNano). For each sample, a minimum of five different locations were imaged to confirm the repeatability. The level-2 micro-wrinkles were imaged using non-contact white light interferometry (ZygoNewView 7300 Optical Profilometer). A Zeiss Axio Imager M2m optical microscope was used with 20x objective for optical imaging.

4.2.3 Confocal imaging

Wrinkled PDMS samples with 5 μ L water droplets containing fluorescently labelled microparticles (Micro particles based on melamine resin, FITC marked, 1 μ m in diameter, Sigma-Aldarich) on top were observed using confocal laser scanning microscopy (LSM 510, Zeiss, Germany; 40x objective, N.A.=0.55) to record the z-stacks of the samples. The fluorescence was excited by a 488nm laser. Two signals were recorded from each scan. The conventional reflectivity signal showed the surface topology and the fluorescence signal showed the existence of water. The fluorescence signal was superimposed on the reflectivity signal for a better view.

4.2.4 Contact angle (CA) measurements

The contact angles were taken with ramé-hart Model 260 Standard Contact Angle Goniometer at ambient temperature. For the measurement of the static contact angle, a 5 μ L deionized (DI) water droplet was first deposited gently on the hierarchical wrinkled surface using an automatic pipet, and then a photograph of the water droplet rested on the sample surface was taken immediately using the goniometer camera. The advancing and receding contact angles were measured by smoothly increasing or decreasing the volume of the droplet volume. The CA was measured from the photograph by the software. For each sample, at least three points were measured in two directions: perpendicular to and parallel with the wrinkled groove direction and an average value was recorded. To examine the stability of the measured contact angles after perturbation, the sample with a water droplet on top was clamped with a tweezer and manually shaken up and down at a frequency of \sim 3Hz and amplitude of 1 \sim 2cm for 3 seconds. Then the sample was placed back on goniometer and CAs of two directions were measured. This procedure was

repeated until the measured contact angles of both directions became unchanged. The experiments were conducted at three different locations of each sample to validate the consistency.

4.3 Tunable Dimensions of Multiscale Hierarchical Wrinkles

Figure 4.2a shows the representative SEM images of a hierarchical wrinkled surface structure after sequential strain release and plasma-UVO treatment with $\varepsilon_1 = \varepsilon_2 = 25\%$, $T_1 = 5\text{min}$, and $T_2 = 40\text{min}$ in a high (left) and low (right) magnified resolution, respectively. The corresponding cross section profiles are shown in Figure 4.2b and Figure 4.2c. It shows that sub-micron wrinkles at level 1 have an average amplitude A_1 and wavelength λ_1 of $A_1 \approx 297\text{nm}$ and $\lambda_1 \approx 800\text{nm}$ (measured by AFM); while the micro-wrinkles at level 2 have an average amplitude and wavelength of $A_2 \approx 4.5\mu\text{m}$ and $\lambda_2 \approx 25.8\mu\text{m}$ (measured by white light interferometry).

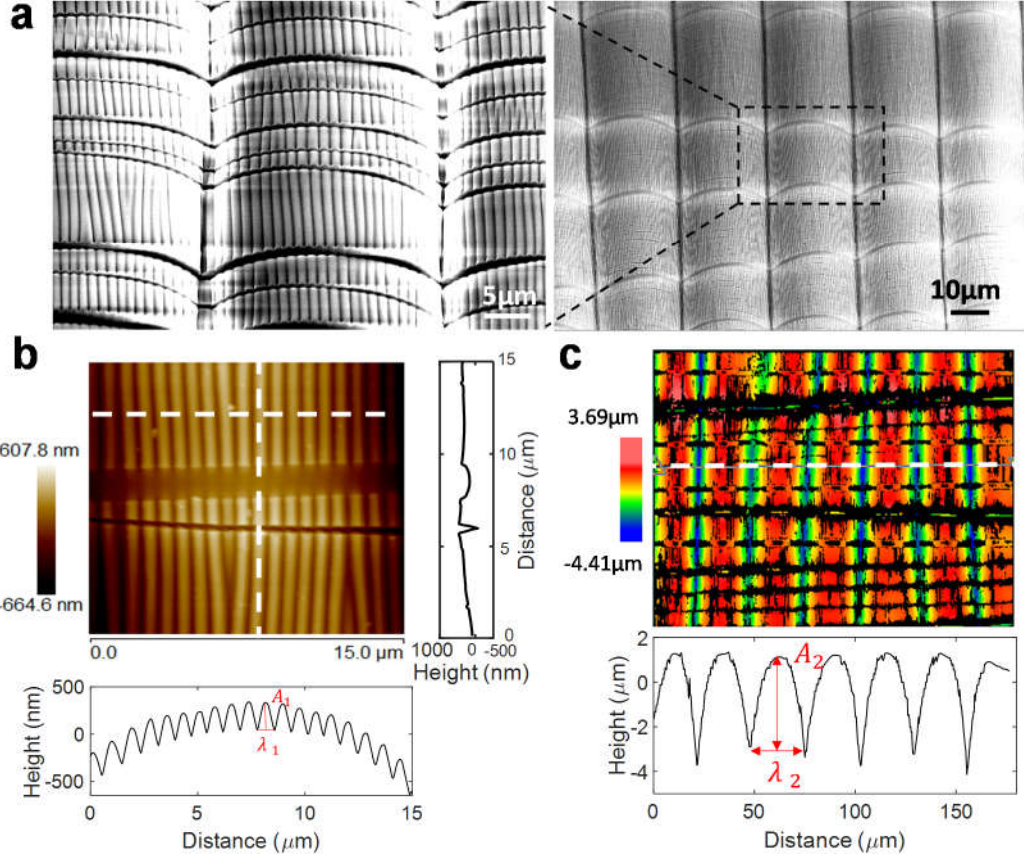


Figure 4.2: (a) SEM images of hierarchical wrinkles generated with $\varepsilon_1 = \varepsilon_2 = 25\%$, $T_1 = 5\text{min}$, $T_2 = 40\text{min}$. left: magnified view. (b) Corresponding AFM images of hierarchical wrinkles with measured horizontal and vertical cross-sectional profiles along the white dashed line shown to the bottom and to the right, respectively. (c) Corresponding optical profilometer images of level-2 large-wavelength wrinkles in the hierarchical wrinkle with measured cross-sectional profile along the white dashed line shown to the bottom.

It is well known that the geometrical size of the single-period wrinkles (wrinkling wavelength λ and amplitude A) for a thin film rested on a soft substrate can be well predicted by the following theoretical model[129], i.e.

$$\lambda = 2\pi t_f \left(\frac{\bar{E}_f}{3\bar{E}_{sub}} \right)^{\frac{1}{3}} \quad (4.1)$$

$$A = \frac{\lambda}{\pi} \sqrt{(\varepsilon - \varepsilon_{cr})} \quad (4.2)$$

where t_f is the film thickness of the oxidation layer after plasma or UVO treatment, $\bar{E} = E/(1 - \nu^2)$ is the plane-strain modulus with E being the Young's modulus and ν being the Poisson's ratio, respectively. The subscripts ' f ' and ' sub ' refer to the stiff film and soft substrate, respectively. ε is the released strain and ε_{cr} is the critical wrinkling strain given by[129]

$$\varepsilon_{cr} = -\frac{1}{4} \left(\frac{3\bar{E}_{sub}}{\bar{E}_f} \right)^{\frac{2}{3}} \quad (4.3)$$

The dimension of each level in the hierarchical wrinkles can be controlled independently by manipulating the treatment time and released strain in terms of Equation (4.1) and (4.2). Figure 4.3a and 4.3b show that the dimension of each hierarchical wrinkle can be tuned in the range of $\lambda_1 \approx 700 - 1500$ nm and $A_1 \approx 50 - 500$ nm for small-wavelength wrinkles generated in the 1st step of plasma treatment, and $\lambda_2 \approx 15 - 35$ μ m and $A_2 \approx 3.5 - 5.0$ μ m for large-wavelength wrinkles generated in the 2nd step of UVO treatment. Generally, the wavelength and amplitude of wrinkles generated in either treatment step show an approximately linear relation with the treatment duration.

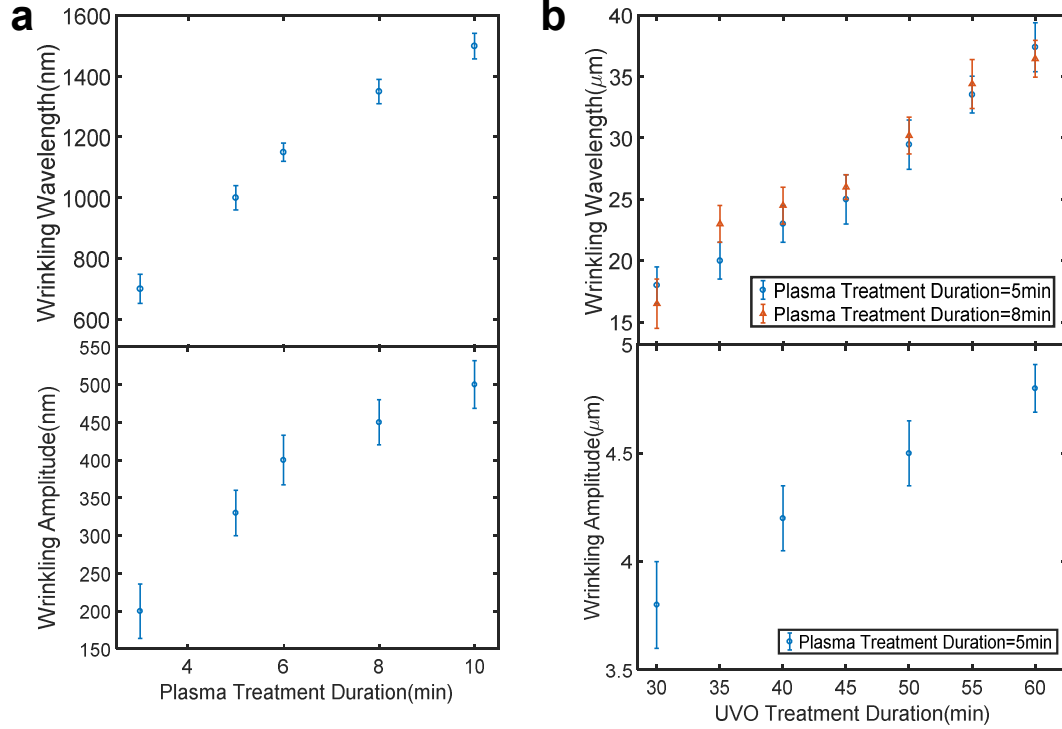


Figure 4.3: (a) Measured wavelength and amplitude of the generated small-wavelength wrinkles as a function of the plasma treatment duration. (b) Measured wavelength and amplitude of the generated large-wavelength wrinkles as a function of the UVO treatment duration. All the pre-strain is set to be 25%.

Meanwhile, a quantitative evaluation of the film thickness can be approximately obtained from Equation (4.1) with the measured wrinkle wavelength, i.e.

$$t_f = \frac{\lambda}{2\pi} \left(\frac{3\bar{E}_{sub}}{\bar{E}_f} \right)^{\frac{1}{3}} \quad (4.4)$$

The corresponding estimated film thickness as a function of treatment time is shown in Figure 4.4, where literature values[38, 133, 162] for the mechanical properties of stiff silica layer generated by plasma treatment with $\bar{E}_f = 140 \text{ GPa}$ ($E_f = 130 \text{ GPa}$ and $\nu = 0.27$) and silica layer generated by UVO treatment with $\bar{E}_f = 43 \text{ GPa}$ ($E_f = 40 \text{ GPa}$ and $\nu =$

0.27) , and $\bar{E}_{sub} = 2.3\text{MPa}$ ($E_{sub} = 1.8\text{MPa}$ and $\nu = 0.48$) for the PDMS substrate were used in Equation (4.4). It is found that the first layer of stiff films generated during plasma treatment has an approximate thickness t_{f1} of 4 - 9 nm, while the second layer of stiff films generated during UVO treatment has an approximate thickness t_{f2} of 150 - 350 nm, which is about 35 times thicker than the first layer. Since t_{f2} is much larger than t_{f1} , the existence of level-1 small-wavelength wrinkles generated in the 1st step is expected to have a negligible effect on the dimension of level-2 large-wavelength wrinkles formed in the following step. This is confirmed by Figure 4.3b, where given the measurement error, the change of the first stiff layer thickness with different treatment time T_1 almost does not affect the wavelength of level-2 wrinkles λ_2 generated in the 2nd step treatment.

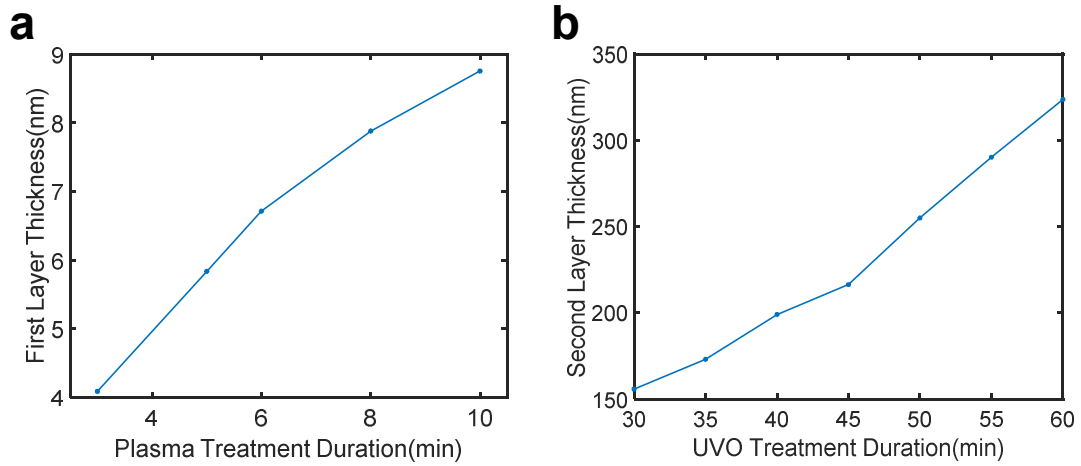


Figure 4.4: (a) The thickness of first layer stiff film generated on first strain release as a function of the Plasma treatment time. (b) The thickness of second layer stiff film generated on second strain release as a function of the UVO treatment time.

4.4 Cracks in Hierarchical Wrinkles

Figure 4.2b shows that two types of cracks with different depths and widths are also observed from the AFM-measured vertical cross section profile, the direction of

which is orthogonal to the generated hierarchical wrinkles. This is due to the lateral tensile deformation resulting from the Poisson's effect, where cracks were generated during the strain release in both sequential steps. I believe that the shallow but wide crack with depth ≈ 200 nm and width ≈ 1.8 μm corresponds to the thinner stiff layer generated in the 1st step of plasma treatment. This is evidenced by the AFM measured cross-sectional profile cut from the valley of wrinkles (see Figure 4.2b and Figure 4.5), where the wide crack vanished in the cross-sectional profile of the valleys, indicating that this is the first layer crack. The relatively deeper and narrower crack with depth ≈ 520 nm and width ≈ 0.7 μm corresponds to the thick stiff layer generated in the 2nd step of UVO treatment. The reason for the observed wider cracks during the 1st step release is that the subsequent applied strain during the 2nd step release will further widen the cracks generated in the 1st step.

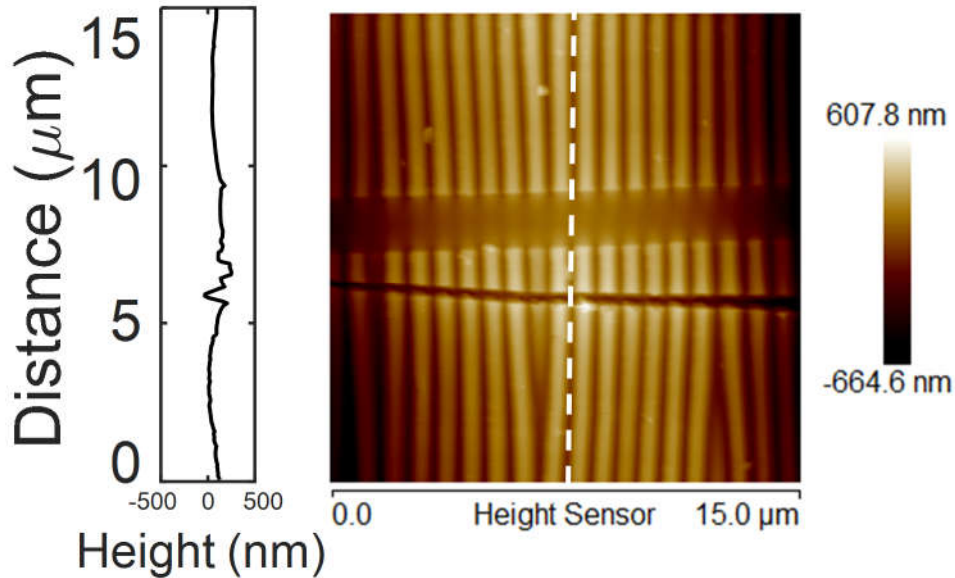


Figure 4.5: AFM images of hierarchical wrinkling surface with $\varepsilon_1 = \varepsilon_2 = 25\%$, $T_1 = 5$ min, $T_2 = 40$ min. From the cross sectional profile located at the valley of small wrinkles, it can be seen that the wide crack disappears but narrow cracks exist, indicating the wide cracks occur during the first release.

To quantify the relationship between the crack density and the change of the released strain and treatment time, I did a statistical study on the crack distribution by counting the number of cracks and analyzing the crack densities (defined as the number of cracks per 100 μm). The related result is shown in Figure 4.6. Generally, upon strain release, the density of cracks generated during the 1st step of plasma treatment is much smaller than that of cracks generated during the 2nd step of the UVO treatment (Figure 4.6). The reason is that the stiff film created by the UVO treatment is much thicker than that created by the plasma treatment (Figure 4.4), thus more prone to fracture. By varying the released strain in one step while fixing the released strain in the other step, I found that the density of cracks generated during either step only depends on the released strain in its respective step (Figure 4.6a and 4.6b). When I increased the plasma treatment duration, it shows a slight increase in the density of cracks upon strain release in both steps (Figure 4.6c). However, it was found that longer UVO treatment duration will only increase the density of cracks generated in the 2nd-step strain release (Figure 4.6d). In general, I found that similar to the formation of wrinkles, the cracks generated from the 1st and 2nd step strain release are independent from each other, and the crack density is more sensitive to the released strain than the plasma/UVO treatment time.

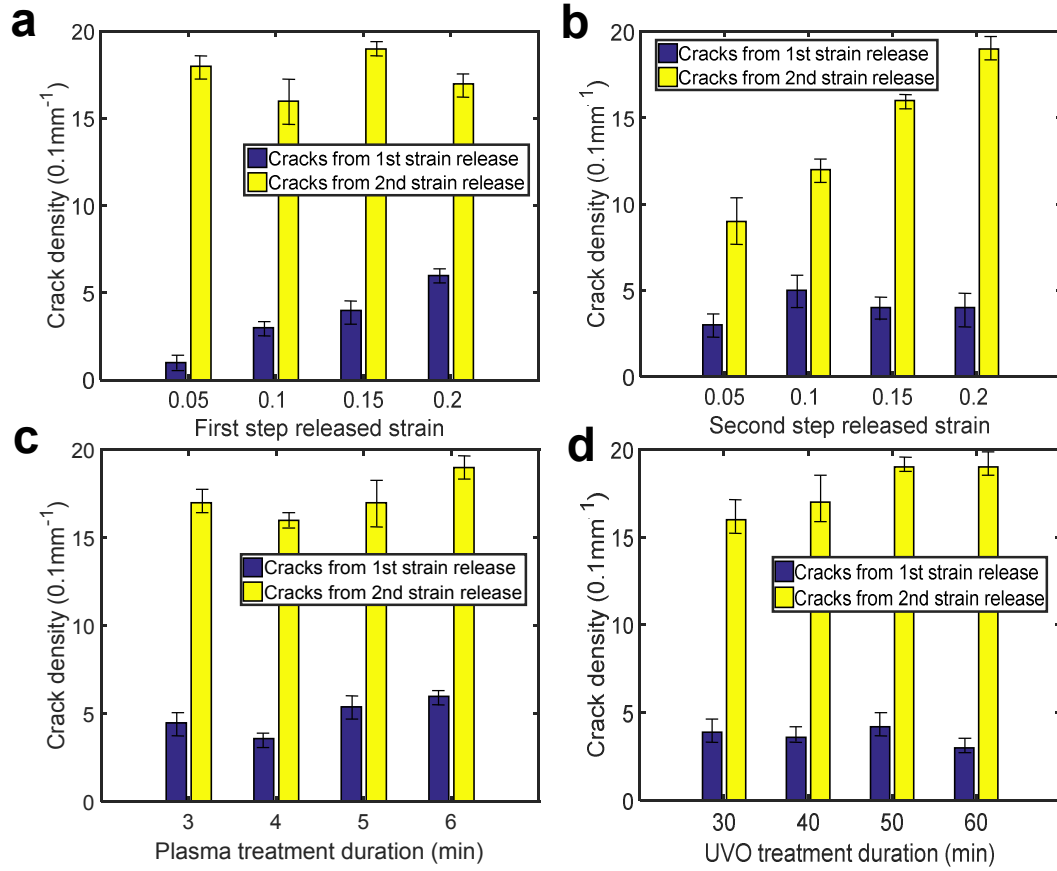


Figure 4.6: Dependence of the measured crack densities on (a) 1st-step released strain, (b) 2nd-step released strain, (c) plasma treatment duration, and (d) UVO treatment duration.

4.5 Effect of Wrinkles' Dimension on Anisotropic Wetting Behavior

Equipped with the knowledge of controlling the geometrical size of hierarchical wrinkles, next I investigated how the hierarchical geometry influences their corresponding anisotropic wetting behavior. Figure 4.7a shows the representative anisotropic wetting behavior of a 5 μ L water droplet on a hierarchical wrinkled surface with $A_1 \approx 267$ nm, $\lambda_1 \approx 750$ nm, and $A_2 \approx 4.2$ μ m, $\lambda_2 \approx 21.4$ μ m. The droplet size is small such that the effect of its gravitational force can be negligible. The top view of the water droplet shows that the water droplet became elongated along the wrinkle grooves. The apparent static contact angles were measured along both perpendicular and parallel

directions to the orientation of wrinkles (Figure 4.7b). The parallel direction's contact angles $\theta_{parallel}$ along the wrinkles were 4 degrees larger than those measured from the perpendicular direction to the wrinkles $\theta_{perpendicular}$, indicating an anisotropic wetting behavior on the hierarchical wrinkled surface. The value of the wetting anisotropy $\Delta\theta$ is defined as the difference of the contact angles measured from these two orthogonal directions[163], i.e.

$$\Delta\theta = \theta_{parallel} - \theta_{perpendicular} \quad (4.5)$$

By tuning the amplitude and wavelength of micro-wrinkles, I studied the effect of the aspect ratio of level-2 wrinkles (which is defined as A_2/λ_2) on the contact angle values and degree of wetting anisotropy of the hierarchical wrinkled surfaces, while the size of level-1 sub-micron wrinkles is approximately kept as the same ($A_1 \approx 300\text{nm}$, $\lambda_1 \approx 800\text{nm}$) considering the experimental measurement error. The results of the measured static contact angles along with dynamic contact angles in both directions are summarized in Table 4.1. I find that as the aspect ratio grows from 0.024 to 0.128, $\theta_{parallel}$ increases from 112° to 120° , while $\theta_{perpendicular}$ remains almost unchanged with a value of about 110° . Meanwhile, the degree of wetting anisotropy $\Delta\theta$ increases from 3° to 9° . When the aspect ratio is further increased, i.e. $0.13 < A_2/\lambda_2 < 0.2$, both $\theta_{parallel}$ and $\theta_{perpendicular}$ reach $125^\circ \sim 135^\circ$ and $\Delta\theta$ becomes about $4^\circ \sim 5^\circ$. I further notice that as A_2/λ_2 increases, along the parallel direction, the advancing contact angles increase from 115° to 140° while the receding contact angles decrease from 75° to 66° . A similar trend was also observed for the advancing and receding contact angles along the perpendicular direction. The contact angle hysteresis of both parallel and

perpendicular directions increases with the growing aspect ratios of level-2 micro-wrinkles. However, the contact angle hysteresis along the parallel direction is larger than that along the perpendicular direction for all aspect ratios ranging from 0.024 to 0.196, indicating that the water droplet is easier to transport along the perpendicular direction.

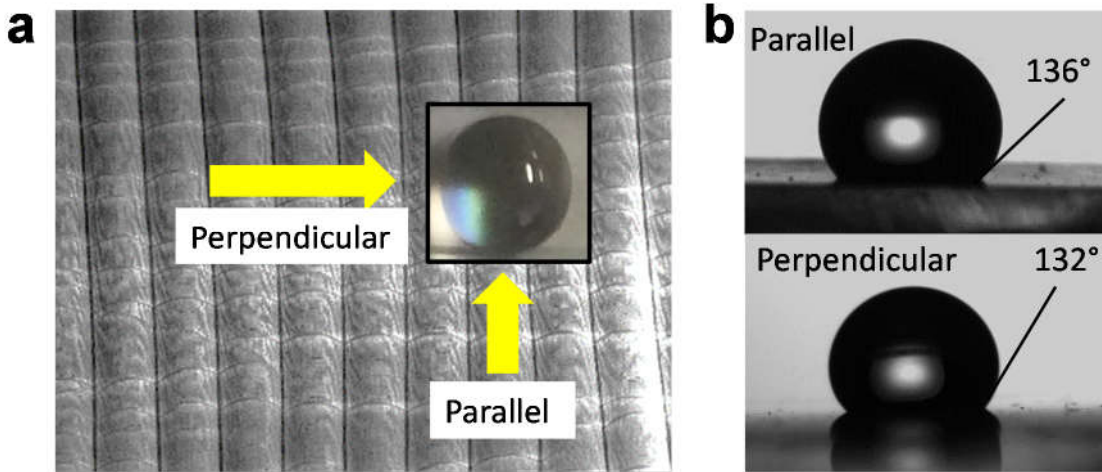


Figure 4.7: (a) SEM image of a hierarchical wrinkled structure with $A_1 \approx 267 \text{ nm}$, $\lambda_1 \approx 750 \text{ nm}$, $A_2 \approx 4.2 \text{ }\mu\text{m}$, $\lambda_2 \approx 21.4 \text{ }\mu\text{m}$. Inset: top view optical image of a $5\text{ }\mu\text{L}$ water droplet resting on the hierarchical wrinkled surface. (b) Side views of the droplet oriented to the parallel (top) and perpendicular (bottom) directions of wrinkles, respectively.

Table 4.1: Measured static and dynamic contact angles and degrees of wetting anisotropy on hierarchical wrinkled PDMS substrate

$A_1(\text{nm})$	$\lambda_1(\text{nm})$	$A_2(\mu\text{m})$	$\lambda_2(\mu\text{m})$	A_2/λ_2	Crack Densities (0.1 mm^{-1})	Parallel			Perpendicular			$\Delta\theta(\text{deg})$
						Stat. (deg)	Adv. (deg)	Rec. (deg)	Stat. (deg)	Adv. (deg)	Rec. (deg)	
275	822	0.6	25	0.024	4/8	112	115	75	109	120	93	3
322	774	2.75	39	0.071	6/12	113	116	74	110	121	90	3
305	790	3.5	39	0.090	4/10	115	118	73	110	119	87	5
311	825	4.35	34	0.128	4/14	120	122	75	111	118	89	9
247	770	2.5	16.7	0.150	3/15	129	134	72	125	129	82	4
297	800	4.5	25.8	0.174	4/17	127	131	62	124	130	87	3
270	776	3.75	20	0.188	5/20	135	136	64	130	133	85	5
315	815	4.5	23.3	0.193	7/18	134	138	68	129	134	82	5
267	750	4.2	21.4	0.196	5/21	136	140	66	132	137	84	4

The increase in the degree of wetting anisotropy with the wrinkle aspect ratio in hierarchical wrinkles is consistent with the observation on single-period micro-wrinkles generated through UVO treatment on pre-strained PDMS substrate reported by Chung et al.,[109]. However, in sharp contrast to the reported large value of wetting anisotropy ($\Delta\theta$ up to 50°) in single-period wrinkles[109], the self-similar hierarchical wrinkles in this work show a much smaller $\Delta\theta$ of up to 10° . Similar small degree of wetting anisotropy is also reported by Lee et al., on superhydrophobic non-similar hierarchical wrinkled surfaces[164], which is generated by depositing layer by layer silica nanoparticles on single-period micro-wrinkled PDMS substrate through UVO treatment. Lee et al., found that as the surface roughness of hierarchical nanostructures increases, the wettability can even transit from anisotropic ($\Delta\theta \approx 18^\circ$, hydrophobic wetting state) to isotropic wetting ($\Delta\theta \approx 0^\circ$, superhydrophobic wetting state) despite the existence of anisotropic micro-wrinkled microstructures[164]. By comparing the wettability on wrinkled PDMS

substrate including single-period micro-wrinkles (static CAs in the range of $64^\circ - 100^\circ$)[109], self-similar multiscale hierarchical wrinkles (static CAs in the range of $110^\circ - 135^\circ$), and nanoparticles on single-period micro-wrinkles (static CAs in the range of $110^\circ - 175^\circ$)[164], I suggest the observed reduced degree of wetting anisotropy in hierarchical wrinkles be partially attributed to the increased hydrophobicity due to the hierarchical nanostructures. Under superhydrophobic cases, anisotropic wetting could be largely suppressed by the superhydrophobicity of patterned surfaces, as evidenced by the observed small angle of wetting anisotropy in a multiscale hierarchical rice leaf surface ($\theta_{parallel} \approx 154^\circ$ and $\theta_{perpendicular} \approx 157^\circ$ with $\Delta\theta \approx 3^\circ$) despite the anisotropic grooved microstructures[164].

4.6 Wetting state of hierarchical wrinkles: theoretical and experimental analysis

Two classic wetting models, the Wenzel model and Cassie-Baxter (CB) models, are widely used to characterize the apparent contact angle on a rough surface[155, 165, 166]. The Wenzel model assumes that the surface is fully wetted, and its apparent contact angle θ^* will be enhanced by the surface roughness according to the equation[167]:

$$\cos\theta^* = r \cos\theta_Y \quad (4.6)$$

where r is the surface roughness, and θ_Y is the Young contact angle of the material. The CB model, on the other hand, assumed that the air is trapped below the droplet forming a composite interface. The droplet wets in the CB wetting state follows the following equation[168]:

$$\cos\theta^* = f(1 + \cos\theta_Y) - 1 \quad (4.7)$$

where f is the fraction of the projection area that is wet.

Regarding the wetting state in a sinusoidal-wave-like surface, Johnson and Dettre demonstrated that for a single-period sinusoidal surface without hierarchy, the preferred wetting state could transfer from the Wenzel state to CB state when the aspect ratio is above a certain value[169]. Bittoun et al. showed the theoretical possibility of the CB state in a hierarchical sinusoidal structure[161].

4.6.1 Thermodynamic model

To determine the wetting state on our hierarchical sinusoidal wrinkling surface, I theoretically calculated the surface free energy by following the thermodynamic model proposed by Marmur et al. [161, 165]. In general, a water droplet on our hierarchical wrinkling structure could be modelled as a solid-liquid-vapor wetting system. The Gibbs energy of such a system could be described by

$$G=A_{lv}\sigma_{lv} + A_{sl}\sigma_{sl} + A_{sv}\sigma_{sv} \quad (4.8)$$

Where σ is the interfacial tension, A is the interfacial area, and the subscripts l, s and v stand for liquid, solid and vapor, respectively. The liquid-vapor interfacial area consists of two parts, one is the outside surface of the drop and another is the liquid-vapor interfaces within the wrinkling grooves

$$A_{lv} = 2\pi R^2(1 - \cos\theta) + (1 - f)\pi R^2 \sin^2\theta \quad (4.9)$$

R is the radius of the spherical drop, θ is the apparent contact angle at any given state of a drop. The solid-liquid interfacial area is given by

$$A_{sl} = \pi R^2 r_f f \sin^2\theta \quad (4.10)$$

where r_f is the roughness ratio of wet part. The solid-vapor interfacial area also consists of two parts, the interface outside the drop and within the grooves:

$$A_{sv} = (A_{tot} - \pi R^2 r \sin^2 \theta) + \pi R^2 r_{1-f} (1-f) \sin^2 \theta \quad (4.11)$$

Here, A_{tot} is the total area of the solid surface, and r_{1-f} is the roughness ratio which related to r_f by

$$r_f f + r_{1-f} (1-f) = r \quad (4.12)$$

The drop radius is related to its volume by

$$R^2 = \left(\frac{3V}{\pi}\right)^{\frac{2}{3}} (2 - 3\cos\theta + \cos^3\theta)^{-2/3} \quad (4.13)$$

Introducing equations (4.9)-(4.13) into (4.8), the dimensionless surface free energy G^* could be calculated as

$$G^* = F^{-\frac{2}{3}}(\theta) (2 - 2\cos\theta - (r_f f \cos\theta_Y + f - 1) \sin^2\theta) \quad (4.14)$$

where

$$F(\theta) = (2 - 3\cos\theta + \cos^3\theta) \quad (4.15)$$

where r_f is the roughness ratio of the actual wet area and θ is the apparent contact angle.

Both r_f and f are functions of the normalized droplet penetration depth h ($0 < h < 1$) defined as the normalized distance between the liquid level and base (inset of Figure 4.8a), i.e. $r_f = r_f(h)$, $f = f(h)$. It is known that among all the apparent contact angles, the CB contact angle defined by equation (4.7) (note that the CB contact angle will transfer to the Wenzel contact angle when it is fully penetrated) is associated with the lowest surface free energy[161]. Thus by replacing θ with θ_{CB} in Equation (4.14), it could be further simplified as the following with only one argument h left:

$$G^* = F^{-\frac{2}{3}}(\theta_{CB}) (2 - 2\cos\theta_{CB} - (r_f f \cos\theta_Y + f - 1) \sin^2\theta_{CB}) \quad (4.16)$$

The minimums of equation (4.16) must also be the minimums of original equation (4.14).

For the observed hierarchical sinusoidal wrinkles, their geometry can be modelled by:

$$y = A_1 \sin\left(\frac{\pi}{\lambda_1} x\right)^2 + A_2 \sin\left(\frac{\pi}{\lambda_2} x\right)^2 \quad (4.17)$$

A Matlab code was developed to numerically calculate r_f and f in Equation (4.16) for the hierarchical surface morphology modeled by Equation (4.17), where normalized droplet penetration depth h varied from 0 to 1 in incremental steps of 0.01 (Appendix B). For the calculation, the Young contact angle is chosen as the measured value of $\theta_Y = 96^\circ$ for the treated PDMS substrate without pre-stretching or wrinkle, which shows slight hydrophobicity, as well as isotropic wettability in both parallel and perpendicular directions. Due to cracks-induced accelerated hydrophobic recovery[170], our measured Young CA is larger than the previously reported data in literature[109]. In addition, the amplitude and wavelength of level-1 wrinkles used in the calculations were fixed by taking the same value as those in experiments with $A_1 = 300\text{nm}$, $\lambda_1 = 800\text{nm}$.

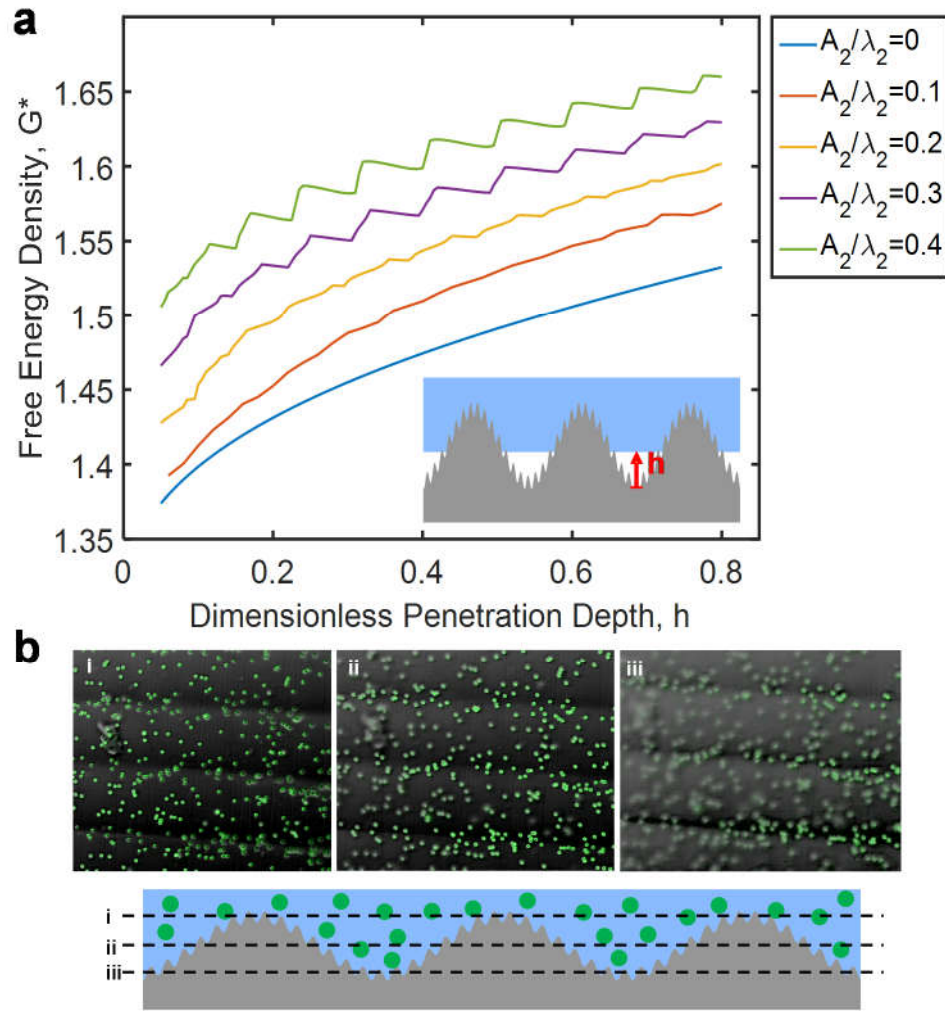


Figure 4.8: (a) Dimensionless free energy density curves vs. the normalized penetration depth for hierarchical wrinkles with different wrinkling aspect ratios. Note that the curves have been translated vertically for clarity. (b) Confocal images combined of reflectance scan (grey) and fluorescence signal (green) at different focus lengths on the peak (i), middle (ii), and valley (iii) of the wrinkle grooves as illustrated by the schematic on the bottom. Nanoparticles (green) are seen from the peaks to the valleys of the wrinkles. The hierarchical wrinkled structure has the dimension of $A_1 \approx 267 \text{ nm}$, $\lambda_1 \approx 750 \text{ nm}$, $A_2 \approx 4.2 \text{ }\mu\text{m}$, $\lambda_2 \approx 21.4 \text{ }\mu\text{m}$.

In Figure 4.8a, I plot the calculated free energy density versus the penetration depth h for the hierarchical wrinkled surface with different aspect ratios of level-2 micro-

wrinkles (i.e. $A_2/\lambda_2 = 0, 0.1, 0.2, 0.3,$ and 0.4). For relatively shallow micro-wrinkles with $A_2/\lambda_2 \leq 0.2$, the regime that our samples locate, the free energy density has one single minimum at $h = 0$, which means that the droplet penetrates into the grooves of wrinkles and fully wets the surface, corresponding to a Wenzel state. That is to say, our hierarchical wrinkled samples with aspect ratios of no larger than 0.2 all favor a Wenzel wetting state. As A_2/λ_2 further increases, i.e. $0.2 < A_2/\lambda_2 \leq 0.4$, I notice that unlike the low-aspect-ratio hierarchical wrinkles, in this case the free energy density has multiple local minima at various penetration depths. These local minima represent the metastable CB states. However, the Wenzel state at $h=0$ is still the most stable wetting state associated with the lowest free energy density. Therefore, I validate that the hierarchical wrinkled surfaces do have the theoretical possibility to support the CB state but it requires a much higher aspect ratio of $A_2/\lambda_2 = 0.3 \sim 0.4$. However, so far the aspect ratio of experimentally generated wrinkles is limited to be lower than 0.3 due to the transition to localized modes such as creasing[39, 171, 172], folding[10, 19, 41], ridging[122, 173, 174], and period-doubling[41, 175], thus making it hard to transit to CB states.

4.6.2 Directly observation through confocal imaging

To further examine the theoretically predicted wetting state, I used the fluorescent particle dispersed water and confocal microscopy to capture the penetration depth that water droplets wet the wrinkle grooves by following the technique introduced by Verho[176] (see experimental section for more information). A $5\mu\text{L}$ droplet of fluorescence marked particles dispersed water was gently deposited on the sample surface with $A_1 = 267\text{nm}$, $\lambda_1 = 750\text{nm}$, $A_2 = 4.2\mu\text{m}$, $\lambda_2 = 21.4\mu\text{m}$, which has the largest

aspect ratio of $A_2/\lambda_2 \approx 0.2$ in Table 4.1. As illustrated in the schematic (bottom of Figure 4.8b), the confocal microscope was set to focus on the peak (i), middle (ii), and valley (iii) of the wrinkling grooves. A 488nm laser was used to excite the fluorescence. Two signals could be received from the observation. The conventional reflectivity signals show the surface structure and the fluorescence signal indicates the distribution of water. Due to the limit of the resolution, the level-1 sub-micron wrinkles were not able to be observed.

Figure 4.8b shows the corresponding fluorescent images at the three representative depths. At position (i), i.e. the peak of wrinkles, all the fluorescent micro-particles at this layer were excited (Figure 4.8b(i)), showing no concentration of water. In position (ii), i.e. the middle of wrinkles, the fluorescent micro-particles at the side walls of wrinkle grooves became lit, indicating the presence of water in those regions (Figure 4.8b(ii)). In position (iii), i.e. the valley of wrinkle grooves, the fluorescent micro-particles in a narrow region emitted lights, showing that the water went all the way down to the bottom of the wrinkled structure (Figure 4.8b(iii)). This confirms that the wetting state is the Wenzel state. Noting that in Figure 4.8b(iii), since the confocal microscope focused on the valley of wrinkle grooves, the wrinkled structure cannot be seen very clear due to the small depth of the field of view of the objective.

4.7 Anisotropic Wetting Behavior: Theoretical and Experimental Analysis

4.7.1 Failure of Wenzel model

Knowing that the wetting state of the hierarchical wrinkled samples is in the Wenzel state, I first plot the measured contact angles versus the aspect ratio of level-2 micro-wrinkles together with those predicted by the Wenzel model Equation (4.6) for

comparison. The geometric parameters for level-1 sub-micron wrinkles are fixed as $A_1 = 300nm$ and $\lambda_1 = 800nm$ during all the calculations. As shown in Figure 4.9, the predicted contact angle from the Wenzel model has a value of $\sim 100^\circ$ and shows a slight increase with the aspect ratio of the level-2 micro-wrinkles A_2/λ_2 , due to the fact that the surface roughness does not change too much when tuning level-2 micro-wrinkles' aspect ratios in the range from 0 to 0.2 with the existence of level-1 sub-micron wrinkles. By comparing the value of the measured contact angles with that of the theoretically predicted contact angles, I found that the measured contact angles in both parallel and perpendicular directions deviated from the theoretical curve predicted by the Wenzel model with a difference in a range of 10% ~ 30%. It could be seen that the Wenzel model is not able to predict the observed contact angles even when the wetting state is in the Wenzel state.

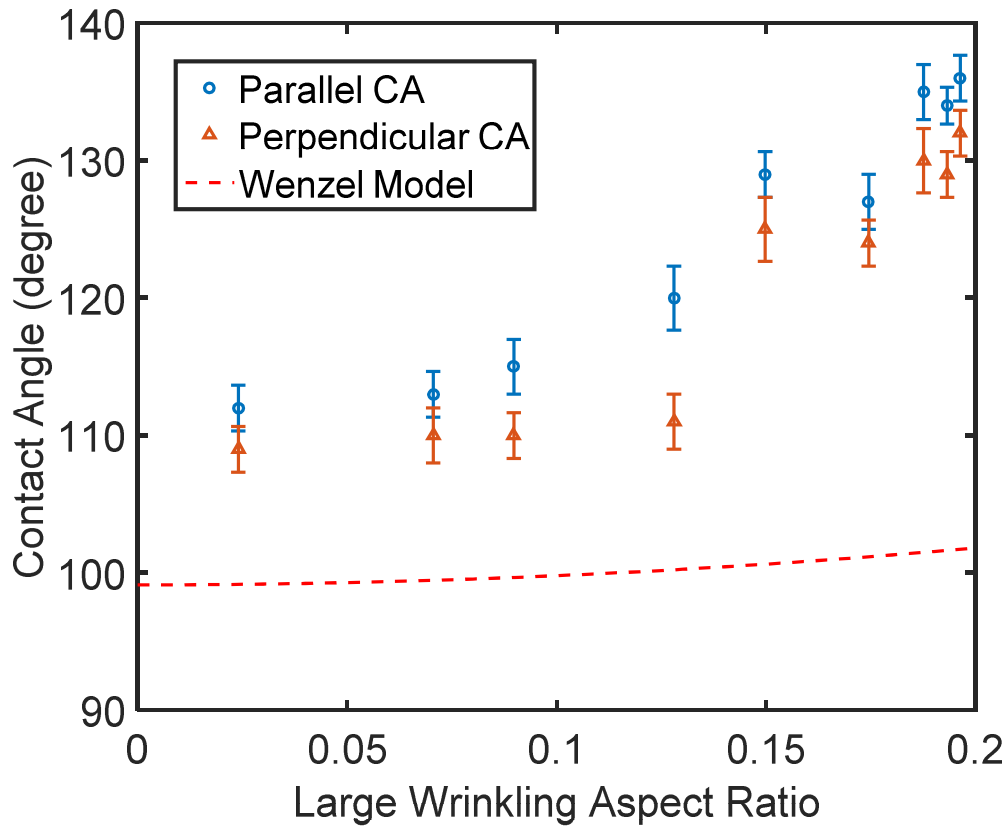


Figure 4.9: Relation between the measured contact angles and Wenzel contact angles.

The failure of using the Wenzel model to predict the measured contact angle can be well explained from a dynamic point of view. Theoretically, the static contact angle could be an arbitrary value between advancing contact angle and receding contact angle depending on history. In our experiments, the static contact angles are close to the advancing contact angles because the water droplets are deposited in a way to increase the droplet volume (Table 4.1). Therefore, the larger static contact angles than the Wenzel contact angles here imply that the dynamic effect is involved in the wetting process.

4.7.2 Experimental evidence of contact line pinning

I decomposed the surface morphology into combined wrinkles and cracks which are orthogonal to each other, and then analyzed the three-phase contact line (TPCL) motion towards these two directions independently. When the TPCL moves against the wrinkles during the wetting and de-wetting process, it will pin on the wrinkle peaks as evidenced by the observed advancing and receding TPCL through optical microscopy (Figure 4.10a). Note that the advancing TPCL cannot be observed directly due to the larger advancing contact angle than 90° . By observing the shape of the droplet, I find that the droplet has a straight contour, implying that the advancing TPCL is pinned and is straight (left of Figure 4.10a). The receding TPCL is straight along the peak of wrinkles and shows more obvious pinning effect of the TPCL (right of Figure 4.10a). Such a pinning effect blocks the motion of the TPCL, and it will induce an energy barrier to prevent the total energy of the system from decreasing to the minimum. A pinned advancing (receding) TPCL will lead to a larger (smaller) contact angle when compared with the equilibrium contact angle. Further adding (withdrawing) water will provide the water droplet additional energy to overcome the energy barrier, thus depin the TPCL and decrease (increase) the contact angle.

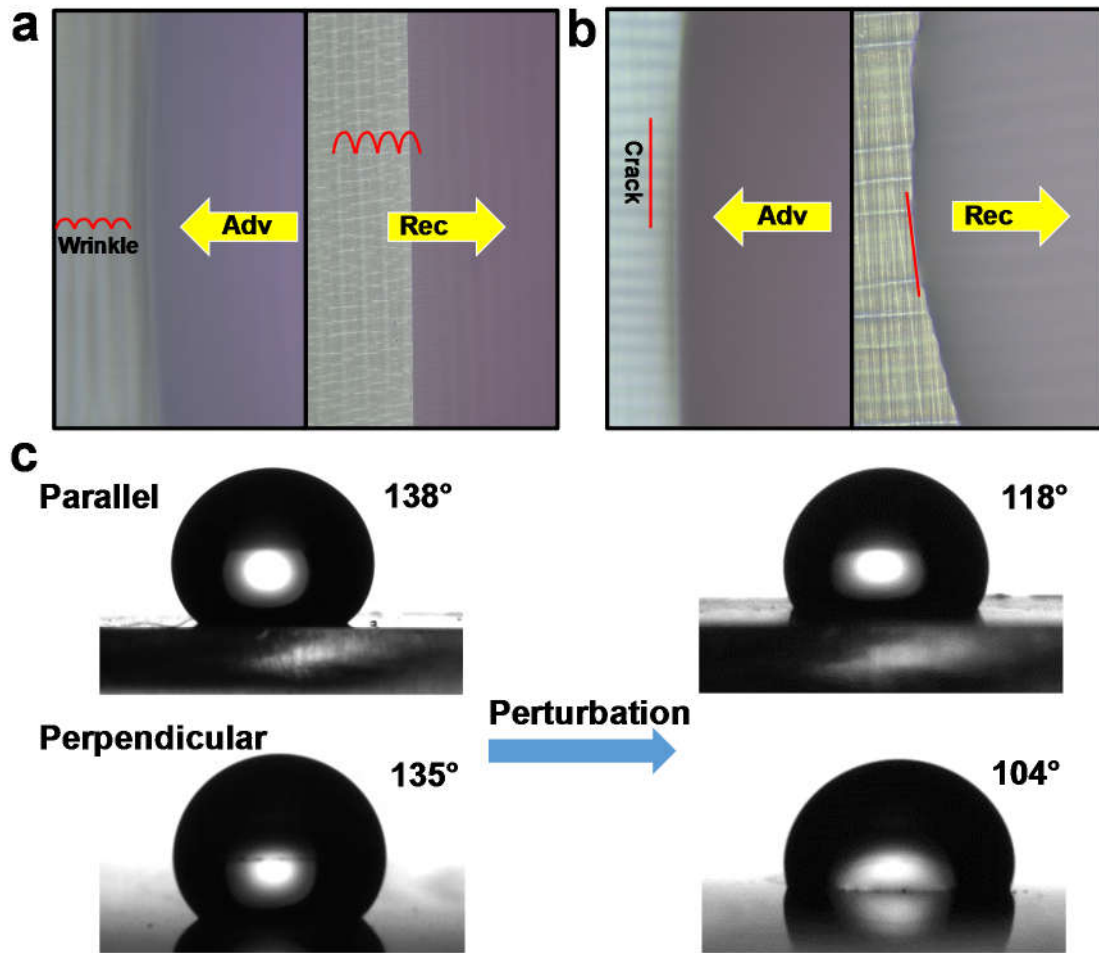


Figure 4.10: Images of advancing and receding contact line when (a) contact line moves against hierarchical wrinkles (b) contact line moves against cracks. (c) Contact angles in the parallel and perpendicular directions of wrinkles before and after vibration on hierarchical wrinkled surfaces.

To validate the pinning and depinning effect, I provide the water droplet certain external energy through vibration. Such external energy will help the TPCL to overcome more energy barriers, thus leading to a decreased contact angle (top of Figure 4.10c). When the sample was gently shaken (see experimental method for details), a sudden collapse of the water droplet was observed. The contact angle decreased from 138° to

115°. Similar phenomenon was also observed when TPCL moves along the wrinkles (against cracks). The cracks will pin the advancing (receding) TPCL (Figure 4.10b), leading to a larger (smaller) contact angle in the perpendicular direction when compared to the equilibrium contact angle. After the vibration perturbation, a sudden drop of the perpendicular contact angle from 135° to 104° was also observed (bottom of Figure 4.10c). Now I can conclude that the measured parallel and perpendicular contact angles which are larger than the Wenzel contact angle result from the pinning effect of wrinkles and cracks, respectively.

4.7.3 Thermodynamic model predicting the dynamic contact angles

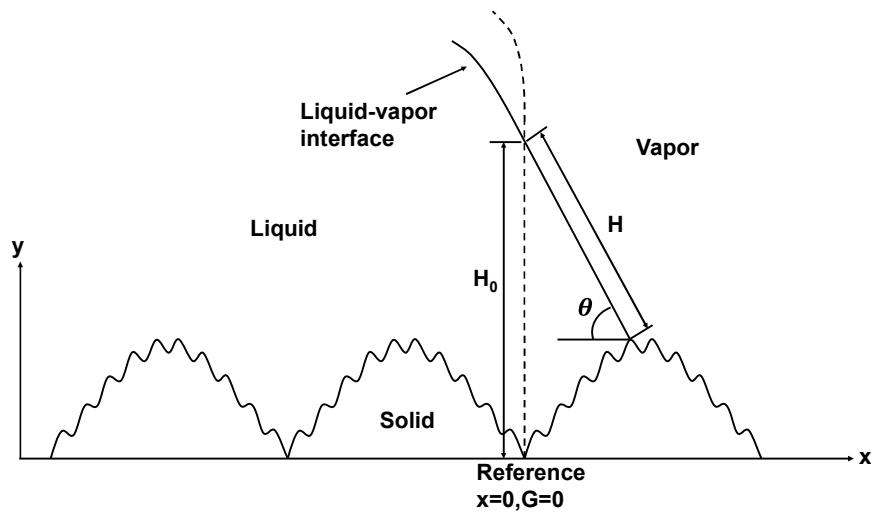


Figure 4.11: Schematic model for the three phase contact line moving against hierarchical wrinkled structure.

To better understand the physics of the pinning and depinning shown in Figure 4.10, a thermodynamic calculation of the change in the surface free energy during the TPCL moving against the wrinkles was performed. Modeling of the water droplet moving against the wrinkles was illustrated in Figure 4.11. In this model, a position with

the apparent contact angle of 90° is set to be a reference where the free energy is 0 and x -coordinate is 0. The total free energy change (ΔG) due to the movement of the TPCL to a new position x with respect to the reference point 0 is represented by

$$\Delta G = \int_0^x -\gamma_{lv} \cos\theta_Y \sqrt{1 + \left(\frac{dy}{dx}\right)^2} dx + \gamma_{lv} \Delta H \quad (4.18)$$

where γ_{lv} is the liquid-vapor interfacial tension, $y(x)$ is the hierarchical wrinkling represented by Equation (4.17), ΔH is the change in the length of liquid-vapor interface. The left term in Equation (4.18) calculates the interfacial energy change resulting from the replacement of a solid-vapor interface by a solid-liquid interface. The right term is the interfacial energy change caused by the change in the length of liquid-vapor interface. The effect of gravity is neglected here. Since ΔH cannot be determined exactly, here I adopt the concept of liquid front for an approximation[177]. In general, as the size of a water droplet is much larger than the characteristic scale of wrinkles, a small portion of the liquid-vapor interface near the solid surface could be approximated as a straight line with a length H_0 and a contact angle θ . After the TPCL moves a small distance x , the liquid front changes to a state with a length H and a contact angle of $\theta + \Delta\theta$. Thus ΔH could be estimated as

$$\Delta H = H - H_0 = \sqrt{(H_0 - y)^2 + x^2} - H_0 \quad (4.19)$$

The relationship between H_0 and contact angle θ could be obtained by a geometric relation:

$$\tan\theta = \frac{H_0 - y}{x} \quad (4.20)$$

Based on Equations (4.18), (4.19) and (4.20), a Matlab code was programmed to numerically calculate the free energy change with respect to the apparent contact angle.

In all the calculations, I set $\gamma_{lv} = 72.6 \text{ mJ}/m^2$ (water surface tension in room temperature), $H_0 = 200 \text{ }\mu\text{m}$. The chosen H_0 is much larger than the scale of wrinkles. In fact, it is found that the ΔG vs. θ curve is independent of H_0 [177].

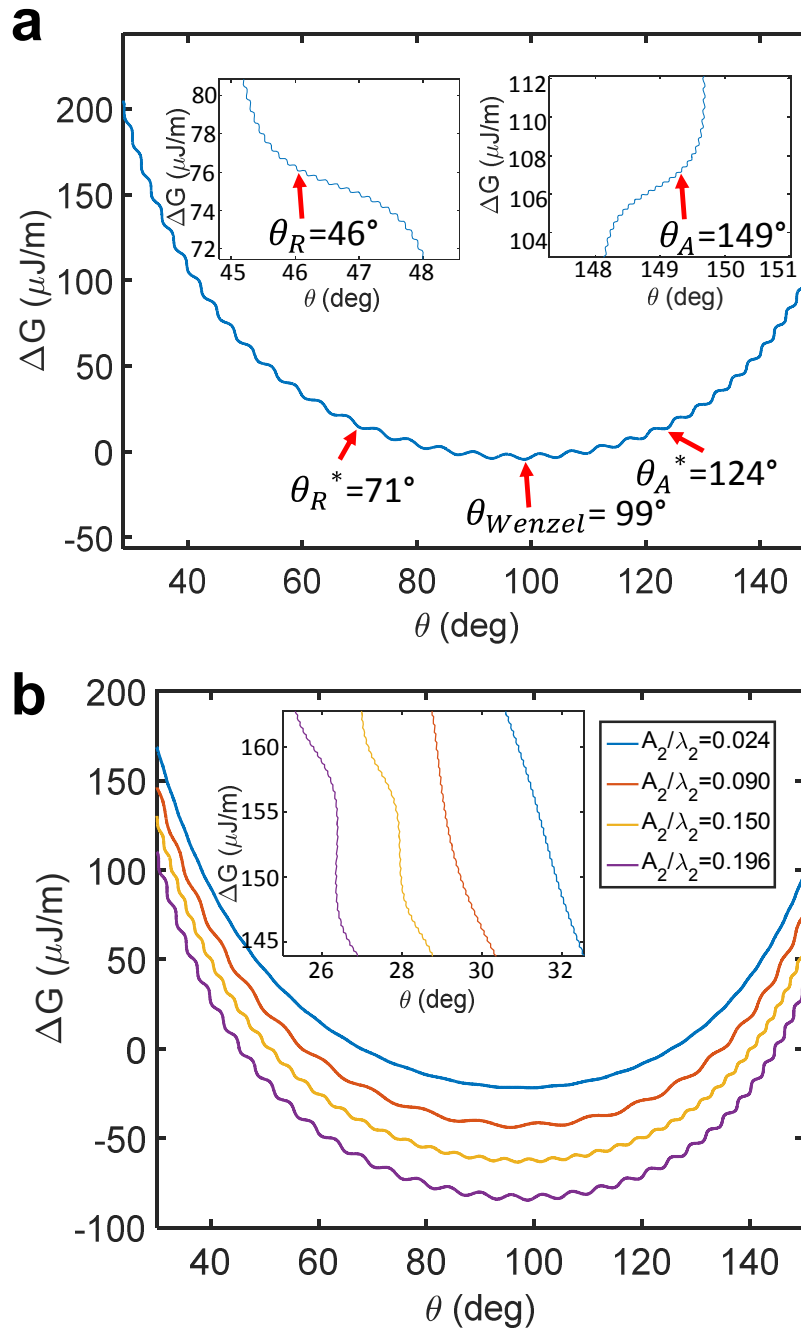


Figure 4.12: (a) Free energy change as a function of contact angle when the three phase contact line moves against the wrinkles for the hierarchical wrinkled structure with $A_1 \approx 267$ nm, $\lambda_1 \approx 750$ nm, $A_2 \approx 4.2$ μm , $\lambda_2 \approx 21.4$ μm (b) Free energy changes as a function of contact angle when the three phase contact line moves against the wrinkles for the hierarchical wrinkled samples with different aspect ratios of level-2 micro-wrinkles.

For a hierarchical wrinkled surface with $A_1 = 267$ nm, $\lambda_1 = 750$ nm, $A_2 = 4.2$ μm , $\lambda_2 = 21.4$ μm , the $\Delta G-\theta$ curve in Figure 4.12a shows a number of local minima, which represent the energy barriers. The local extremes exist at two scales, indicating that in our hierarchical wrinkled surface, both level-1 and level-2 wrinkles will provide the energy barriers and pin the TPCL. The small energy barriers correspond to the level-1 sub-micron wrinkles while the large energy barriers correspond to the level-2 micro-wrinkles. To overcome the energy barrier from the level-1 and level-2 wrinkles, the energy needed is 0.2 μJ and 4 μJ , respectively. This result indicates that it will take 20 times more energy to overcome a large energy barrier than that requires to overcome a small energy barrier. Theoretically, the first and last local minimum in the $\Delta G-\theta$ curve correspond to two limiting angles, i.e. the receding contact angle and advancing contact angle, which are $\theta_R = 46^\circ$ and $\theta_A = 149^\circ$ here (inset of Figure 4.12a). However, as the level-2 micro-wrinkles are the major energy barriers, it is highly possible that the receding and advancing contact angles are mainly determined by the large energy barriers from the level-2 micro-wrinkles. With this assumption, by only counting the large energy barriers, now we can obtain a modified receding contact angle ($\theta_R^* = 71^\circ$) and a modified advancing contact angle ($\theta_A^* = 124^\circ$) from Figure 4.12a. There is a global minimum of 99° corresponding to the Wenzel contact angle.

To investigate the effect of aspect ratio of the level-2 micro-wrinkles on the total free-energy change, we also plot the $\Delta G-\theta$ curves for hierarchical wrinkles with different $A_2/\lambda_2 = 0.024, 0.090, 0.150, 0.196$ together (Figure 4.12b). As expected, the energy barriers from level-2 micro-wrinkles decrease dramatically with the reduced aspect ratio. When the aspect ratio is close to zero, the two scales of the energy barriers in the free

energy curve are reduced to one. On contrast, the energy barriers from the level-1 sub-micron wrinkles remain almost unchanged due to their approximately constant aspect ratio (inset of Figure 4.12b). Therefore, we can see that the magnitude of the energy barriers is dependent of the aspect ratio of the wrinkles. For hierarchical wrinkles with a larger aspect ratio, it can form deeper energy barriers, thus leading to a stronger pinning effect.

To validate my theory, I compare the theoretically predicted advancing and receding contact angles with experimental measurements, the data of which are summarized in Table 4.2. Generally, we can see that as the aspect ratio of level-2 micro-wrinkles increases from 0.024 to 0.196, the calculated advancing contact angles increase while the calculated receding contact angles decrease. The unmodified advancing contact angles provide an upper limit as it counts the energy barriers from both hierarchical level wrinkles, while the modified advancing contact angles provide a lower limit since only level-2 micro-wrinkles are considered to contribute to the energy barriers. Similarly, for the receding contact angles, the unmodified ones represent the lower limit while the modified ones represent the upper limit. Thus, the predicted unmodified and modified contact angles from the theory set the upper and lower limits for the possible values of a measured advancing/receding contact angle in experiments. As shown in Table 4.2 on the comparison of both advancing and receding contact angle between experiment and theory, both the measured advancing and receding contact angles for all the hierarchical wrinkled samples with aspect ratio ranging from 0.024 to 0.196 fall into the range predicted by theory, validating my theoretical models.

Table 4.2: Calculated and measured advancing and receding contact angles in the parallel direction of hierarchical wrinkled PDMS substrate

$A_1(\text{nm})$	$\lambda_1(\text{nm})$	$A_2(\mu\text{m})$	$\lambda_2(\mu\text{m})$	A_2/λ_2	Static (deg)	Wenzel (deg)	Adv.(deg)			Rec.(deg)		
							Expt	Calcd*	Calcd	Expt	Calcd*	Calcd
275	822	0.6	25	0.024	112	97.8	115	106	132	75	93	62
322	774	2.75	39	0.071	113	98.6	116	105	140	74	85	57
305	790	3.5	39	0.090	115	98.5	118	107	140	73	86	52
311	825	4.35	34	0.128	120	98.3	122	112	144	75	80	49
247	770	2.5	16.7	0.150	129	97.8	134	114	144	72	79	50
297	800	4.5	25.8	0.174	127	98.5	131	119	145	62	76	45
270	776	3.75	20	0.188	135	98.3	136	123	147	64	76	45
315	815	4.5	23.3	0.193	134	98.9	138	124	148	68	75	44
267	750	4.2	21.4	0.196	136	98.4	140	124	149	66	71	46

Note: * Represents modified advancing or receding contact angles.

4.8 Calculation of Volume Fraction and Roughness Factor of Cracks

Calculations for ϕ_s and r in Cassie and Wenzel equations resulted from cracks based on a simplified model are shown in Figure 4.13. All dimensions, in micrometers, are based on the SEM images and AFM images. In all calculations, n is the number of large wrinkles covered by the droplet; $a_1=1.8\mu\text{m}$, $b_1=0.2\mu\text{m}$, $c_1=33\mu\text{m}$ and $a_2=0.7\mu\text{m}$, $b_2=0.52\mu\text{m}$, $c_2=6\mu\text{m}$ are the width, depth, interval of cracks generated in first release and second release, respectively. The magnitude of n is adequately large, since at least hundreds of cracks are covered. Based on this value, we can estimate that the surface roughness factor r and the solid fraction ϕ_s as below:

$$\phi_s = \frac{c_2 * 5n}{c_1 * n + a_1 * (n-1)} = \frac{6 * 5n}{33n + 1.8(n-1)} = 0.86 \quad (4.21)$$

$$r = \frac{[c_1 * n + (n-1) * a_1] + 2n * b_1 + b_2 * 8n}{c_1 * n + (n-1) * a_1} = \frac{[33n + 1.8(n-1)] + 2n * 0.2 + 0.52 * 8n}{33n + 1.8(n-1)} \approx 1.13 \quad (4.22)$$

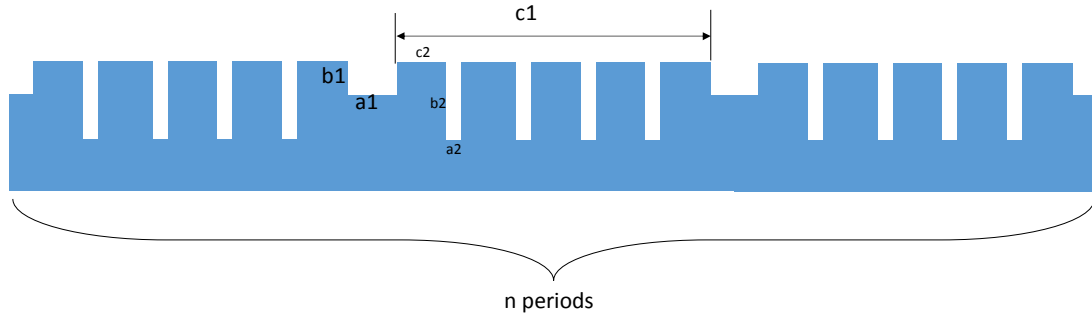


Figure 4.13: Schematic illustration of modeling cracks of two levels.

4.9 Some Remarks on Coexistence of Orthogonal Wrinkles and Cracks

When a water droplet is deposited on the hierarchical wrinkled surface, it cannot automatically go to the position with the lowest free energy, i.e. the Wenzel contact angle, due to the existence of energy barriers. Instead, the TPCL will be trapped into a metastable state with a contact angle larger than the Wenzel contact angle. Only when enough energy is input, the TPCL can overcome the energy barriers and continue to move. Therefore, the observed apparent contact angles are the intermediate contact angle between the advancing contact angle and Wenzel contact angle as validated by the data in Table 4.2. Furthermore, when the TPCL moves along the wrinkles, it will encounter cracks. To estimate the influence of cracks, I did a quantitative analysis based on the statistical data of cracks densities and dimensions. From the SEM images shown in Figure 4.2a, the average interval in between narrow cracks and in between wide cracks is approximately $6 \mu\text{m}$ and $33 \mu\text{m}$, respectively. The depth of narrow cracks and wide cracks are estimated to be 520 nm and 200 nm , respectively. Based on these measured data, the surface roughness factor r can be estimated to be ~ 1.13 and the solid fraction f is $\sim 86\%$ due to the existence of cracks. Since the cracks-induced changes in surface

roughness and solid fraction are small, the main effect of cracks lies in forming the energy barriers and pinning the TPCL in a way similar to the effect of wrinkles. In addition to the geometry, the existence of cracks exposed the untreated PDMS, forming a chemical contrast with treated PDMS. Such heterogeneous chemical pattern will also lead to an anisotropic wetting [153] that will enhance the pinning effect of cracks.

For wrinkled surfaces without cracks, previous studies have shown that the perpendicular contact angle is close to the Young contact angle on a flat surface[109, 163]. For our samples, the perpendicular contact angles are larger than the Young contact angle due to the pinning effect of cracks (Figure 4.10b). Generally, the crack density increases with the aspect ratio of level-2 micro-wrinkles, thus leading to an increased density of energy barriers. Therefore, a sample surface with more cracks will have a larger perpendicular contact angle, as evidenced by the data shown in Table 4.1. That is to say, wrinkles and cracks will compete with each other in elongating the droplet along their respective orientation, which partially accounts for the observed small degrees of wetting anisotropy in experiments. Similar competition between two orthogonal features through imprinted hierarchical structures was reported by Zhang et al. in determining the wetting anisotropy[156], where the smallest degree of wetting anisotropy was observed when the second level rectangular grooves are orthogonal to those in the first level with similar scales. Examples of competition between orthogonal features in determining the anisotropic wetting in hierarchical structures can be also observed in nature. Koch et al. revealed that daisy florets have several different hierarchical structures, including parallel hemispherical protrusions with cuticle folds on top and perpendicular to the protrusions, parallel trapezoid protrusions with cuticle folds on top surface and parallel with

protrusions, and parallel triangular protrusions with cuticle folds on side walls and perpendicular to protrusions[178]. Among these three anisotropic structures, the second one, i.e. the protrusions and cuticle folds have the same orientation, demonstrate the largest wetting anisotropy the ($\Delta\theta \approx 46^\circ$), while the other two structures exhibiting two orthogonal features have a much smaller wetting anisotropy ($\Delta\theta \approx 12^\circ$ - 17°) due to the competing contact line pinning effect.

Another potential contribution factor to the small degree of wetting anisotropy in the hierarchical wrinkled PDMS samples could be the hydrophobicity of PDMS materials itself. Previous research has shown that the hydrophobicity of materials could also reduce the anisotropy of wetting[179], especially when the hydrophobicity of the materials is high enough to enable the formation of CB state on certain anisotropic structured surface, the wetting on such surfaces could be nearly isotropic. In our case, the hydrophobicity is expected to reduce the wetting anisotropy but in a very limited extent since the wetting state in hierarchical wrinkles is still Wenzel state. Thus, I believe that the pinning effect plays a dominant role in determining the observed small degree of wetting anisotropy.

4.10 Conclusion

In summary, I have studied the anisotropic wetting behavior on self-similar hierarchical wrinkled structures through a combined experimental characterization and theoretical modeling. The hierarchical wrinkled structure with features crossing from hundreds of nanometers to tens of microns is fabricated through sequential plasma and UVO treatment upon sequential strain release. The dimension of wrinkles at each hierarchical level can be quantitatively and independently controlled by manipulating the

treatment time and sequential strain release. The hierarchical dimensional effect on the wetting state and anisotropic wetting behavior of hierarchical wrinkled surface were systematically investigated through both experimental and theoretical analysis. I conclude that the observed apparent contact angles are the intermediate contact angles between advancing contact angles and Wenzel contact angles due to the energy barriers from orthogonal wrinkles and cracks, which is validated by both experiments and theoretical predictions. Furthermore, the competition between orthogonal wrinkles and cracks in contact line pinning accounts for the observed small degree of wetting anisotropy in the hierarchical wrinkled surfaces.

I note that the mechanism of anisotropic wettability on hierarchical structures is still not well understood, where the exact wetting state at nanoscale remains unknown. As noted by Rahmawan et al.[180], there are four possible combinations of wetting state in a dual roughness surface: both the wetting state of microscale and nanoscale are Wenzel (W^m-W^n); the microscale wetting state is Wenzel but the nanoscale wetting state is CB (W^m-C^n); both microscale and nanoscale wetting states are CB (C^m-C^n); and the microscale wetting state is CB while the nanoscale wetting state is Wenzel (C^m-W^n). Due to the limited knowledge of the wetting state on the nanoscale, here the use of Wenzel wetting state in both large scale and small scale represents a simplified explanation of its complex wetting behavior. The results of this work could find potential applications in microfluidics, antifouling, and waterproofing.

CHAPTER 5 FUTURE WORK

5.1 2D Hierarchical Wrinkling Surfaces

In addition to the one dimensional hierarchical wrinkling structure generated by uniaxial stretch, we can also obtain two dimensional hierarchical wrinkling structures by changing uniaxial stretch to biaxial stretch and introducing anisotropic stretch strain, as illustrated in Figure 5.1. If the strain releases in both first and second step are biaxial, a 2D wrinkles on 2D wrinkles pattern could be generated (Top line). If the first strain release is biaxial but second strain release is uniaxial, a 2D wrinkles on 1D wrinkles pattern could be generated (Middle line). If first strain release is uniaxial and second strain release is biaxial, we can get 1D wrinkles on 2D wrinkles pattern (bottom line).

The representative SEM images are shown in Figure 5.1b. Top two of Figure 5.1b show that 2D-2D hierarchical wrinkling structure is composed of large scale creases which are orthogonal to each other and small scale random labyrinth patterns. While the 2D-1D hierarchical wrinkling structure has uniform 1D wrinkles in large scale and 2D labyrinth pattern in small scale. The 1D-2D wrinkle has the same large scale feature with 2D-2D hierarchical wrinkles but 1D wavy structure in small scale.

In chapter 3, I have studied the optical property of 1D on 1D case. I developed a novel smart window based on the 1D-1D self-similar hierarchical wrinkling surface. In chapter 4, I have investigated the dynamic wetting property of hierarchical wrinkling surface. Therefore it has been proven that such hierarchical wrinkling structures have unique property that worth further study. So far the optical property and wetting behavior of 2D hierarchical wrinkling surfaces with different amplitude and wavelength still remains unexplored. Also the potential application of 2D hierarchical wrinkling structure

such as micro fluidics, smart windows, and superhydrophobic surface still requires further investigation.

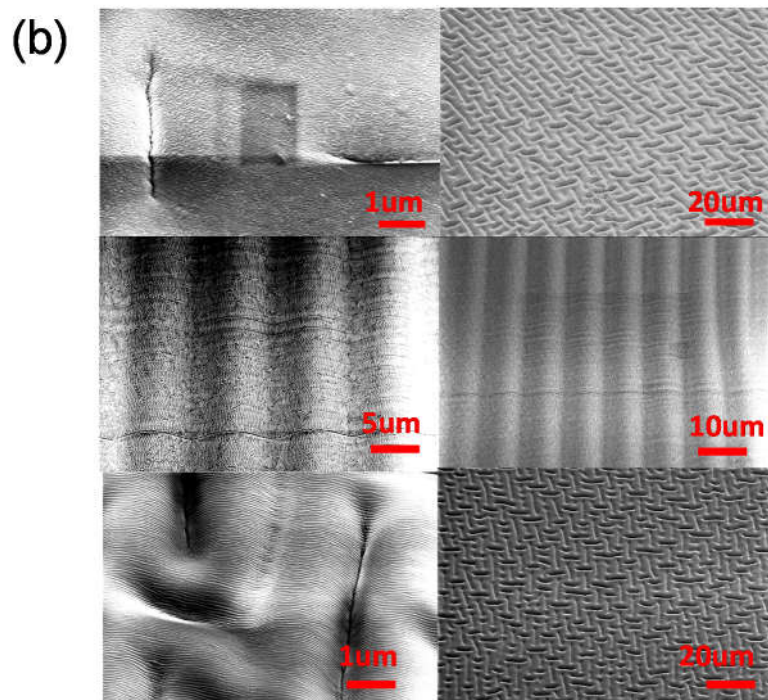
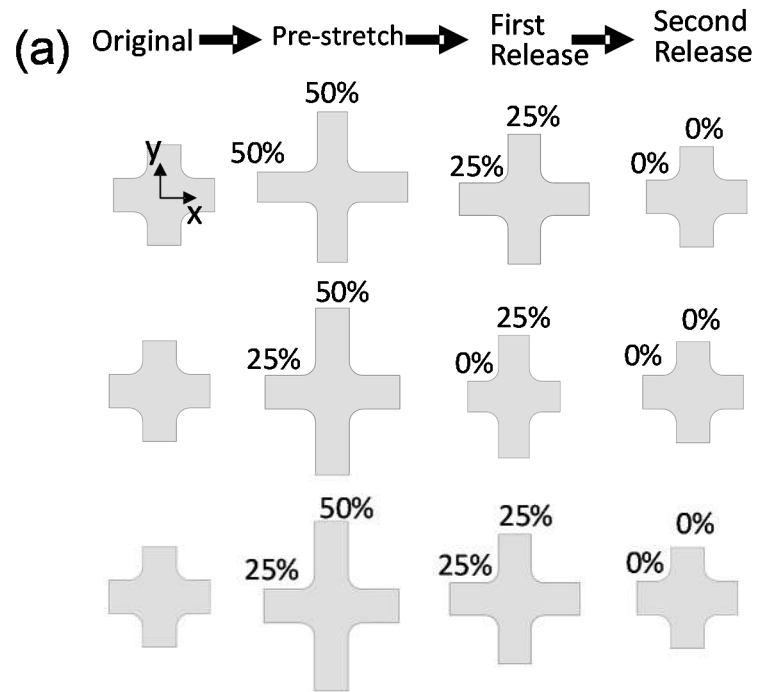


Figure 5.1: (a) Schematic illustration of fabrication process of 2D hierarchical wrinkling surface. (b) Corresponding SEM images of 2D hierarchical wrinkling surface.

5.2 Water Condensation on Wrinkling Surfaces

In nature, control of the heterogeneous nucleation and growth of water droplets on a surface has been crucial for survival and proliferation of the bio-organisms. For example, in extremely arid habitat such as the Namib Desert, beetles *Stenocara sp.* capture and collect water from the early morning fog on their backs, which are covered with a random array of bumps. The peaks of the bumps are smooth and hydrophilic, where the fog is captured, and the troughs consisting of flattened hemispheres (10 μ m in diameter) are superhydrophobic, which assists the roll-off of water droplets[116, 181]. Management of water on surfaces is also important to water filtration, microfluidics, and anti-biofouling.

There have been increasing efforts to create beetle-like patterned surfaces to manipulate water nucleation and growth during condensation [182-190]. Garrod *et al.*[185] show that a surface patterned with hydrophilic-hydrophobic regions enhances the water collection efficiency compared with that from a homogeneously hydrophobic or hydrophilic surface. They suggest that the optimal feature size and center-to-center distance of hydrophilic area are 500 μ m and 1000 μ m, respectively. Dorrer *et al.* suggest that the critical volume at which droplets coalesce and roll off from the hydrophilic spot is linearly proportional to the spot size.[183]

Despite the water condensation on a variety of geometries such as spike[191], pillar[192], and pyramid[193] has been studied, the water condensation on wrinkling surface remains unexplored. Some preliminary investigations of water condensation on 1D single period wrinkles have been conducted by me mainly in order to develop necessary SEM imaging techniques. The fabrication process of wrinkling surface is

shown in Figure 5.2a. Figure 5.2b shows the representative wrinkling structure. To study the water condensation on the wrinkling surface, the wrinkling surface (Figure 5.2b) was put into SEM chamber where the environmental humidity and sample surface temperature was set to be near the water-vapor phase transition line. Environmental Scanning electron microscopy (ESEM) images were taken by FEI Quanta 450FEG in ESEM mode. The sample was mounted on a thermoelectric cooling stage in SEM chamber and tilted 45° for improving the imaging quality. At first the sample surface was cooled down to $1\sim 3^\circ\text{C}$ and relative humidity was set to 100%. Then the chamber pressure was increased to be $\sim 6\text{torr}$ to enable the water condensation occur. To ensure the wrinkling surface were efficiently cooled, the PDMS film was fabricated to have a low thickness of $1\sim 2\text{mm}$. The observation was conducted at least 30mins later after starting

I successfully observed the water condensation through SEM as shown in Figure 5.3-5.6. The condensation behaviors on micropatterned surfaces was categorized into three stages, including initial nucleation, coalescence of small droplets, and large droplet growth. Figure 5.3 shows the initial nucleation of water droplet. As seen from the zoom in SEM images, the water droplet nucleated at the grooves of the wrinkling surface. Figure 5.4 shows the coalescence of small droplets. As pointed by red arrows at $t=6.1$, the two small water droplet coalesce and form one larger droplet. The two larger water droplet pointed by blue arrows at $t=7.3$ further grows and eventually coalesce at $t=19.5$ and became one droplet. After each time tow droplets coalesce, the new droplet will cover more wrinkles. The large water droplet formed at $t=19.5$ covered six wrinkles while the initial nucleated water droplet only cover one groove. Figure 5.5 shows the large droplet growing process. Compared the water droplet at $t=6.1$ and $t=18.5$, it became

larger and taller but the wetting area remains unchanged. Eventually, the large droplet collapsed and wetted a larger area. If the nucleated water droplet cannot coalesce with another droplet, it will also grow but extend along the wrinkling grooves as shown in Figure 5.6. This seems imply that to enable water droplet formation large enough and slide along groove direction, it may require sufficient wide grooves and prevent water droplet coalescing. The further study may proof my idea.

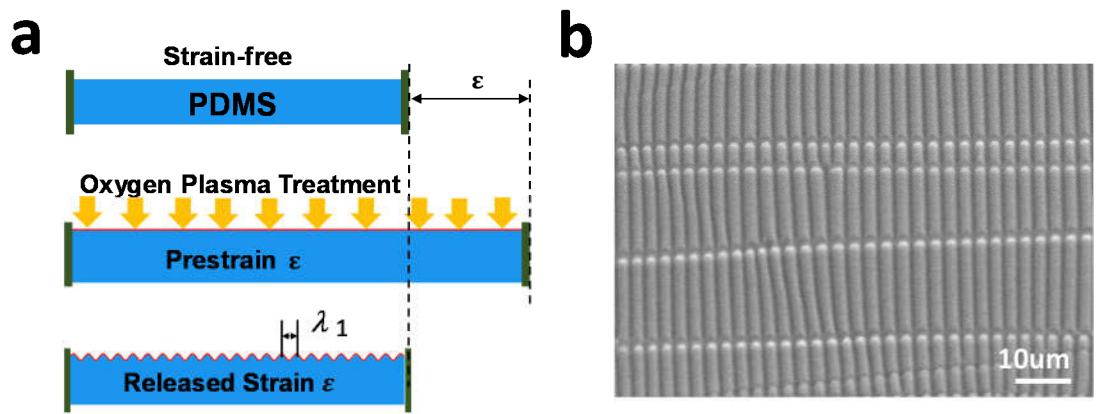


Figure 5.2: (a) Fabrication process of wrinkling surface. (b) SEM images of representative wrinkling surface.

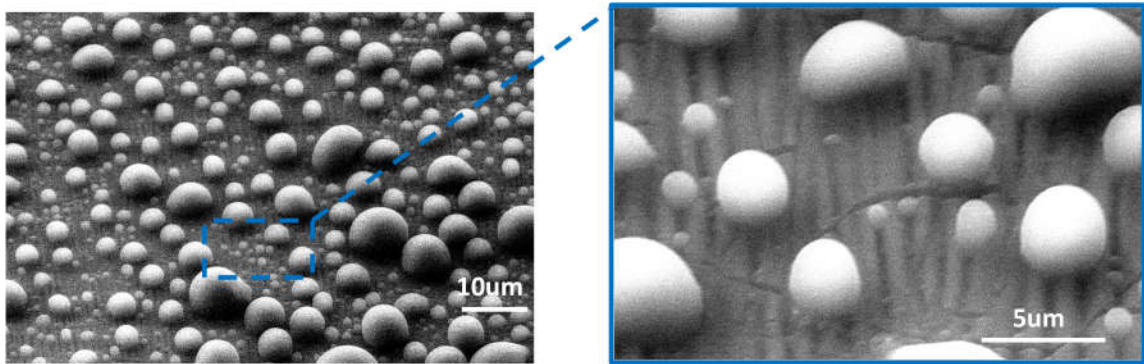


Figure 5.3: SEM images of condensed water on wrinkling surface. The Chamber pressure is 7.2torr, temperature is 4.9°C. Condensation duration is 25mins.

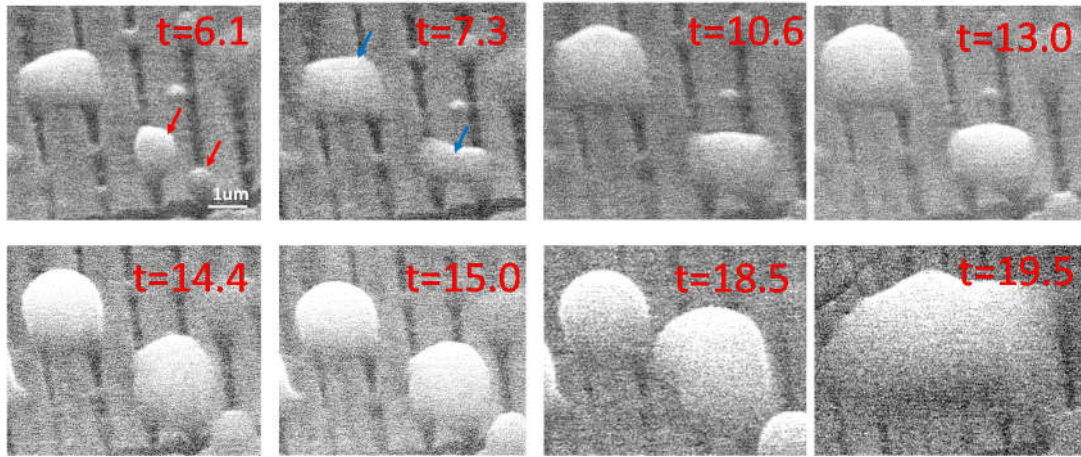


Figure 5.4: Time evolution of water condensation on wrinkling surface showing the coalescence. The Chamber pressure is 5.6torr, temperature is 2.1°C. Condensation time was marked in red, the unit is minute.

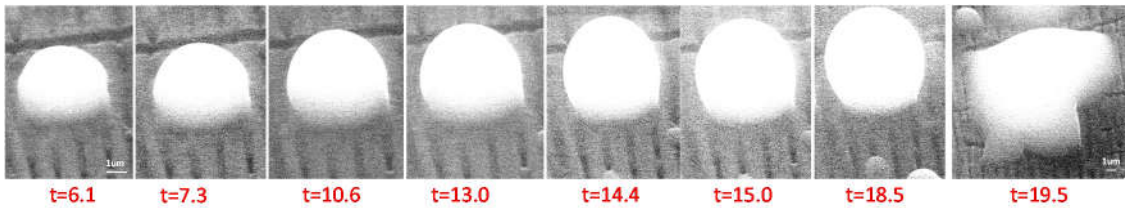


Figure 5.5: Time evolution of water condensation on wrinkling surface showing the large droplet growth. The Chamber pressure is 5.6torr, temperature is 2.1°C. Condensation time was marked in red, the unit is minute.

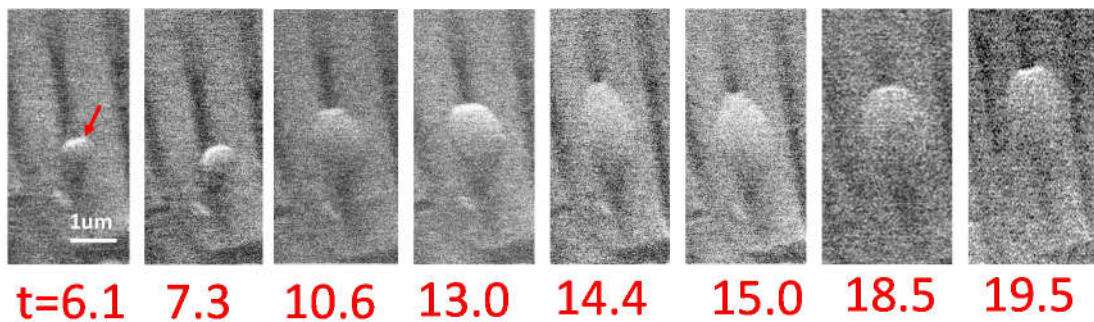


Figure 5.6: Time evolution of water condensation on wrinkling surface showing the single droplet growth. The Chamber pressure is 5.6torr, temperature is 2.1°C. Condensation time was marked in red, the unit is minute.

In addition to the simple single period wrinkles, we may even partially coat the wrinkling surface with nanoparticles to achieve a contrast of wettability, for example the wrinkling ridges are hydrophobic but valleys are hydrophilic. Figure 5.7 shows the wrinkling surface which ridges are coated with 200nm silica nanoparticles through dip-coating. Before the dip coating, the wrinkles have been generated on sample. The particles only assembly on the wrinkling ridges probably due to the Cassie wetting state during dip-coating or the contact line jumping during withdrawing the sample from colloid, which is not clear so far. Interestingly, previous result has demonstrate assembly the nanoparticles on wrinkling valley through dip-coating technique [34]. The reason for our totally reverse result is also not clear yet. The water condensation on such a non-homogenous wrinkling surface may show some unexplored phenomenon and also worth further study.

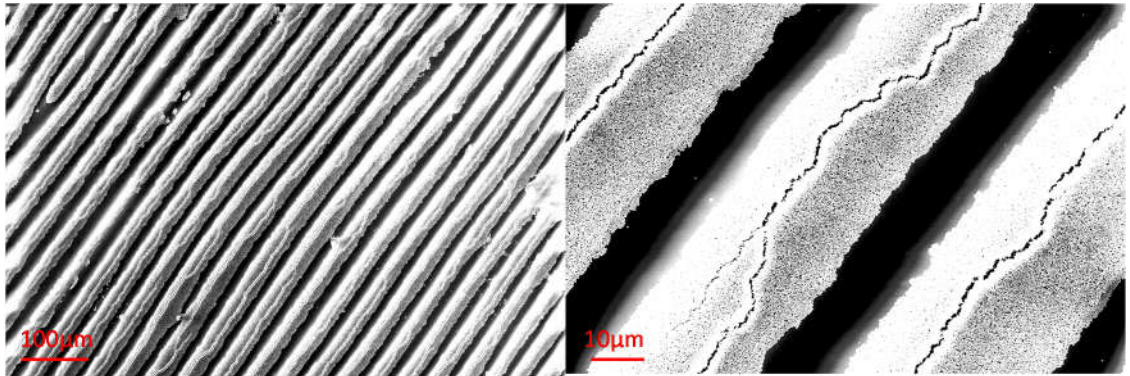


Figure 5.7: SEM images of wrinkles with ridges covered by silica nanoparticles.

5.3 Assembly of Colloidal Particles by Evaporation on Wrinkling Surface with Anisotropic Wettability

Creating ordered assemblies of colloidal particles has attract much attention of researchers. Evaporation provides a straightforward approach of collecting particles from colloid near three-phase contact lines thus has been used in particle self-assembly and exploited in a variety of geometries[34, 194, 195]. I have demonstrated that wrinkling surfaces with anisotropic wettability have unique directionally selected contact line pinning effect. As the assembly of particles highly depend on the moving of three-phase contact lines, how this anisotropic wettability affect the particle assembly is of great interest.

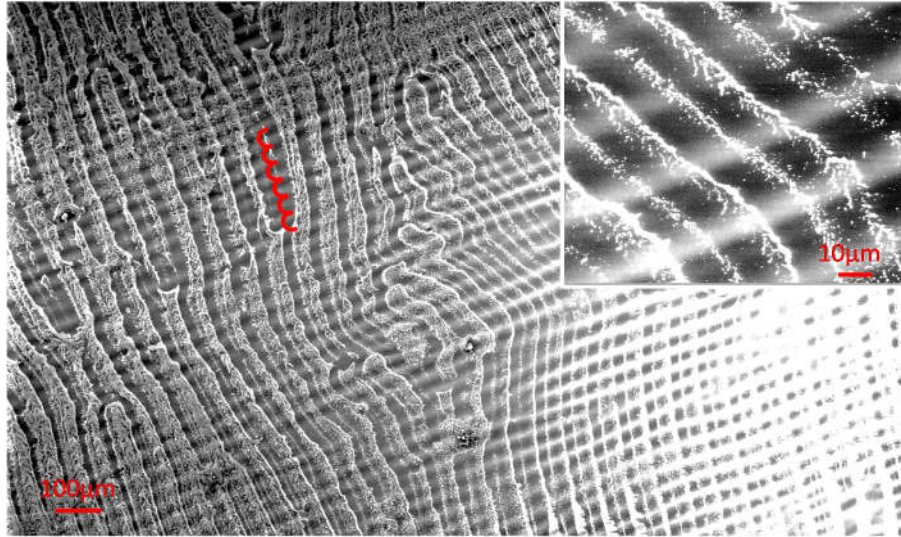


Figure 5.8: SEM image showing the discrete strips of particle distribution after evaporation on wrinkling surface. Insert: zoom in SEM image

I already got some preliminary result. Figure 5.8 shows the distribution of particles after evaporation on a simple single period wrinkling surface. Rather than assembling at wrinkling valleys, the particles after evaporation forms an array of strips which are nearly orthogonal to the wrinkling direction. This may be due to the contact

line pinning effect of wrinkles which blocks the receding contact line moving during evaporation as I have showed in chapter 4. Defects such as splits and curvy strips were observed which may be due to existence of cracks. A more detailed work is required in future in order to understand how the periodicity of these strips come, how we can precisely control the evaporation pattern and how the result can extent to other wetting system. The assembly of colloidal particles may find application or shed some light on molecule concentration and ultra-high sensitive diagnose.

5.4 Swell Induced Buckling of Top and Bottom Constrained Lattice Structure

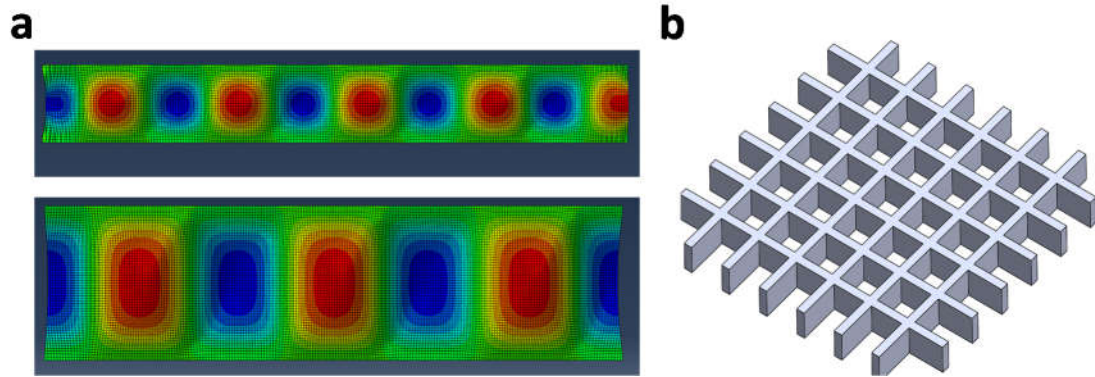


Figure 5.9: (a) FEM simulations of buckling of two edge fixed plates with different width. (b) Schematic illustration of lattice structure.

When a plate is constrained on both top and bottom surface (top and bottom edge in 2D model), it will buckle into periodic dimple like structure. Figure 5.9 shows the buckling shape of two edge constrained plate with different width. For narrow plate, the buckled periodic dimples are more close to a square shape (Figure 5.9a). Double the width will stretch the dimple into a relative rectangular shape. Also, the periodicity is also changed showing dependence on the width. The straight plates orthogonal to each other could form the lattice structure (Figure 5.9b). It has been shown that the bottom fixed lattice structure will generate rotatory joint with two different chirality: left hand and right hand after swelling induced buckling[31]. But it is still unknown if one more constrain e.g. the top surface constrain is added into the system, the chirality will be uniform or not. In future I may further study the swelling induced buckling of top and bottom fixed lattice structure. The analytical methods and techniques will be similar to what has been used in chapter 2. The pattern transformation of the lattice structures with both top and bottom constrained before and after buckling is of the most interest. Also the dependence of buckling wavelength on the geometry and the influence of introduced cuts

on the buckling direction are unknown yet. The potential applications of such constrained lattice structure may include energy absorption, band structure and wettability, which worth further investigation.

REFERENCES

1. Cerda, E. and L. Mahadevan, *Geometry and Physics of Wrinkling*. Physical Review Letters, 2003. **90**(7): p. 074302.
2. Li, B., et al., *Surface wrinkling of mucosa induced by volumetric growth: Theory, simulation and experiment*. Journal of the Mechanics and Physics of Solids, 2011. **59**(4): p. 758-774.
3. Liang, H. and L. Mahadevan, *The shape of a long leaf*. Proceedings of the National Academy of Sciences, 2009. **106**(52): p. 22049.
4. Yin, J., et al., *Stress-driven buckling patterns in spheroidal core/shell structures*. Proceedings of the National Academy of Sciences, 2008. **105**(49): p. 19132.
5. Haven, K.H., *Wonders of the land: merging earth myth with earth science*. 2006, Westport, Conn.: Libraries Unlimited.
6. Mullin, T., et al., *Pattern Transformation Triggered by Deformation*. Physical Review Letters, 2007. **99**(8): p. 084301.
7. Zhang, Y., et al., *One-Step Nanoscale Assembly of Complex Structures via Harnessing of an Elastic Instability*. Nano Letters, 2008. **8**(4): p. 1192-1196.
8. Yin, J., et al., *Deterministic Order in Surface Micro-Topologies through Sequential Wrinkling*. Adv. Mater., 2012. **24**(40): p. 5441-5446.
9. Yang, S., K. Khare, and P.-C. Lin, *Harnessing Surface Wrinkle Patterns in Soft Matter*. Advanced Functional Materials, 2010. **20**(16): p. 2550-2564.
10. Pocivavsek, L., et al., *Stress and Fold Localization in Thin Elastic Membranes*. Science, 2008. **320**(5878): p. 912.
11. Diamant, H. and T.A. Witten, *Compression Induced Folding of a Sheet: An Integrable System*. Physical Review Letters, 2011. **107**(16): p. 164302.

12. Zhang, Q., et al., *Spontaneous Periodic Delamination of Thin Films To Form Crack-Free Metal and Silicon Ribbons with High Stretchability*. ACS Applied Materials & Interfaces, 2017. **9**(51): p. 44938-44947.
13. Gent, A.N. and I.S. Cho, *Surface Instabilities in Compressed or Bent Rubber Blocks*. Rubber Chemistry and Technology, 1999. **72**(2): p. 253-262.
14. Trujillo, V., J. Kim, and R.C. Hayward, *Creasing instability of surface-attached hydrogels*. Soft Matter, 2008. **4**(3): p. 564-569.
15. Khang, D.-Y., et al., *A Stretchable Form of Single-Crystal Silicon for High-Performance Electronics on Rubber Substrates*. Science, 2006. **311**(5758): p. 208.
16. Rogers, J.A., T. Someya, and Y. Huang, *Materials and Mechanics for Stretchable Electronics*. Science, 2010. **327**(5973): p. 1603-1607.
17. Stafford, C.M., et al., *A buckling-based metrology for measuring the elastic moduli of polymeric thin films*. Nat Mater, 2004. **3**(8): p. 545-550.
18. Koo, W.H., et al., *Light extraction from organic light-emitting diodes enhanced by spontaneously formed buckles*. Nat Photon, 2010. **4**(4): p. 222-226.
19. Kim, J.B., et al., *Wrinkles and deep folds as photonic structures in photovoltaics*. Nat Photon, 2012. **6**(5): p. 327-332.
20. Jang, J.-H., et al., *Combining Pattern Instability and Shape-Memory Hysteresis for Phononic Switching*. Nano Letters, 2009. **9**(5): p. 2113-2119.
21. Khare, K., J. Zhou, and S. Yang, *Tunable Open-Channel Microfluidics on Soft Poly(dimethylsiloxane) (PDMS) Substrates with Sinusoidal Grooves*. Langmuir, 2009. **25**(21): p. 12794-12799.
22. Moon, M.-W., et al., *Directed assembly of fluidic networks by buckle delamination of films on patterned substrates*. International Journal of Materials Research, 2007. **98**(12): p. 1203-1208.

23. Kim, J., J. Yoon, and R.C. Hayward, *Dynamic display of biomolecular patterns through an elastic creasing instability of stimuli-responsive hydrogels*. Nature Materials, 2009. **9**: p. 159.
24. Bertoldi, K., et al., *Negative Poisson's Ratio Behavior Induced by an Elastic Instability*. Advanced Materials, 2010. **22**(3): p. 361-366.
25. Li, J., et al., *Switching periodic membranes via pattern transformation and shape memory effect*. Soft Matter, 2012. **8**(40): p. 10322-10328.
26. Zhu, X., et al., *Capillarity induced instability in responsive hydrogel membranes with periodic hole array*. Soft Matter, 2012. **8**(31): p. 8088-8093.
27. Zhu, X., et al., *Two-dimensional photonic crystals with anisotropic unit cells imprinted from poly(dimethylsiloxane) membranes under elastic deformation*. Applied Physics Letters, 2008. **93**(16): p. 161911.
28. Babaei, S., et al., *3D Soft Metamaterials with Negative Poisson's Ratio*. Advanced Materials, 2013. **25**(36): p. 5044-5049.
29. Overvelde, J.T.B., S. Shan, and K. Bertoldi, *Compaction Through Buckling in 2D Periodic, Soft and Porous Structures: Effect of Pore Shape*. Advanced Materials, 2012. **24**(17): p. 2337-2342.
30. Shim, J., et al., *Buckling-induced encapsulation of structured elastic shells under pressure*. Proceedings of the National Academy of Sciences, 2012. **109**(16): p. 5978.
31. Kang, S.H., et al., *Complex Ordered Patterns in Mechanical Instability Induced Geometrically Frustrated Triangular Cellular Structures*. Phys. Rev. Lett., 2014. **112**(9): p. 098701.
32. Efimenko, K., et al., *Nested self-similar wrinkling patterns in skins*. Nat Mater, 2005. **4**(4): p. 293-297.

33. Schweikart, A. and A. Fery, *Controlled wrinkling as a novel method for the fabrication of patterned surfaces*. *Microchimica Acta*, 2009. **165**(3): p. 249-263.
34. Lu, C., H. Mohwald, and A. Fery, *A lithography-free method for directed colloidal crystal assembly based on wrinkling*. *Soft Matter*, 2007. **3**(12): p. 1530-1536.
35. Wilbur, J.L., et al., *Elastomeric Optics*. *Chemistry of Materials*, 1996. **8**(7): p. 1380-1385.
36. Yu, C., et al., *Tunable optical gratings based on buckled nanoscale thin films on transparent elastomeric substrates*. *Applied Physics Letters*, 2010. **96**(4): p. 041111.
37. Huang, Z.Y., W. Hong, and Z. Suo, *Nonlinear analyses of wrinkles in a film bonded to a compliant substrate*. *Journal of the Mechanics and Physics of Solids*, 2005. **53**(9): p. 2101-2118.
38. Jiang, H., et al., *Finite deformation mechanics in buckled thin films on compliant supports*. *Proceedings of the National Academy of Sciences*, 2007. **104**(40): p. 15607-15612.
39. Cao, Y. and J.W. Hutchinson, *From wrinkles to creases in elastomers: the instability and imperfection-sensitivity of wrinkling*. *Proceedings of the Royal Society A: Mathematical, Physical and Engineering Science*, 2011. **468**(2137): p. 94.
40. Holmes, D.P. and A.J. Crosby, *Draping Films: A Wrinkle to Fold Transition*. *Physical Review Letters*, 2010. **105**(3): p. 038303.
41. Brau, F., et al., *Wrinkle to fold transition: influence of the substrate response*. *Soft Matter*, 2013. **9**(34): p. 8177-8186.
42. Vella, D., et al., *The macroscopic delamination of thin films from elastic substrates*. *Proceedings of the National Academy of Sciences*, 2009. **106**(27): p. 10901.
43. Hutchinson, J.W., M.D. Thouless, and E.G. Liniger, *Growth and configurational stability of circular, buckling-driven film delaminations*. *Acta Metallurgica et Materialia*, 1992. **40**(2): p. 295-308.

44. Moon, M.W., et al., *Buckle delamination on patterned substrates*. Acta Materialia, 2004. **52**(10): p. 3151-3159.
45. Edmondson, S., et al., *Buckling in Quasi-2D Polymers*. Advanced Materials, 2006. **18**(6): p. 724-728.
46. Cowin, S.C., *Tissue Growth and Remodeling*. Annual Review of Biomedical Engineering, 2004. **6**(1): p. 77-107.
47. Kopeček, J., *Hydrogel biomaterials: A smart future?* Biomaterials, 2007. **28**(34): p. 5185-5192.
48. Genzer, J. and J. Groenewold, *Soft matter with hard skin: From skin wrinkles to templating and material characterization*. Soft Matter, 2006. **2**(4): p. 310-323.
49. He, L.H. and L. Qiao, *Pre-tension regulates buckling patterns of soft films with interactions*. EPL (Europhysics Letters), 2007. **80**(1): p. 14003.
50. Shenoy, V. and A. Sharma, *Pattern Formation in a Thin Solid Film with Interactions*. Physical Review Letters, 2001. **86**(1): p. 119-122.
51. Hong, W., et al., *A theory of coupled diffusion and large deformation in polymeric gels*. Journal of the Mechanics and Physics of Solids, 2008. **56**(5): p. 1779-1793.
52. Maeda, S., et al., *Self-Walking Gel*. Advanced Materials, 2007. **19**(21): p. 3480-3484.
53. Jeong, K.-U., et al., *Three-dimensional actuators transformed from the programmed two-dimensional structures via bending, twisting and folding mechanisms*. Journal of Materials Chemistry, 2011. **21**(19): p. 6824-6830.
54. Shin, J., P.V. Braun, and W. Lee, *Fast response photonic crystal pH sensor based on templated photo-polymerized hydrogel inverse opal*. Sensors and Actuators B: Chemical, 2010. **150**(1): p. 183-190.
55. Sun, J.-Y., et al., *Ionic skin*. Advanced Materials, 2014. **26**(45): p. 7608-7614.

56. Sidorenko, A., T. Krupenkin, and J. Aizenberg, *Controlled switching of the wetting behavior of biomimetic surfaces with hydrogel-supported nanostructures*. Journal of Materials Chemistry, 2008. **18**(32): p. 3841-3846.
57. Zee, F. and J.W. Judy, *Micromachined polymer-based chemical gas sensor array*. Sensors and Actuators B: Chemical, 2001. **72**(2): p. 120-128.
58. Kishi, R., H. Ichijo, and O. Hirasa, *Thermo-Responsive Devices Using Poly(vinyl methyl ether) Hydrogels*. Journal of Intelligent Material Systems and Structures, 1993. **4**(4): p. 533-537.
59. Kim, J.J. and K. Park, *Smart hydrogels for bioseparation*. Bioseparation, 1998. **7**(4): p. 177-184.
60. Wichterle, O. and D. LÍM, *Hydrophilic Gels for Biological Use*. Nature, 1960. **185**: p. 117.
61. Kopeček, J. and J. Yang, *Hydrogels as smart biomaterials*. Polymer International, 2007. **56**(9): p. 1078-1098.
62. Lin, P.C. and S. Yang, *Mechanically switchable wetting on wrinkled elastomers with dual-scale roughness*. Soft Matter, 2009. **5**(5): p. 1011-1018.
63. Lin, P.-C., et al., *Mechanically tunable dry adhesive from wrinkled elastomers*. Soft Matter, 2008. **4**(9): p. 1830-1835.
64. Lee, S.G., et al., *Switchable Transparency and Wetting of Elastomeric Smart Windows*. Advanced Materials, 2010. **22**(44): p. 5013-5017.
65. Lee, E., et al., *Tilted Pillars on Wrinkled Elastomers as a Reversibly Tunable Optical Window*. Advanced Materials, 2014. **26**(24): p. 4127-4133.
66. Ge, D., et al., *A Robust Smart Window: Reversibly Switching from High Transparency to Angle-Independent Structural Color Display*. Advanced Materials, 2015. **27**(15): p. 2489-2495.

67. Rocklin, D.Z., et al., *Transformable topological mechanical metamaterials*. Nature Communications, 2017. **8**: p. 14201.
68. Rudykh, S. and M.C. Boyce, *Transforming Wave Propagation in Layered Media via Instability-Induced Interfacial Wrinkling*. Physical Review Letters, 2014. **112**(3): p. 034301.
69. Singamaneni, S. and V.V. Tsukruk, *Buckling instabilities in periodic composite polymeric materials*. Soft Matter, 2010. **6**(22): p. 5681-5692.
70. Mei, Y., et al., *Principles and applications of micro and nanoscale wrinkles*. Materials Science and Engineering: R: Reports, 2010. **70**(3–6): p. 209-224.
71. Li, B., et al., *Mechanics of morphological instabilities and surface wrinkling in soft materials: a review*. Soft Matter, 2012. **8**(21): p. 5728-5745.
72. Lin, P.C., et al., *Mechanically tunable dry adhesive from wrinkled elastomers*. Soft Matter, 2008. **4**(9): p. 1830-1835.
73. Chen, C.-M., et al., *Buckling-Based Strong Dry Adhesives Via Interlocking*. Adv. Funct. Mater., 2013. **23**(30): p. 3813–3823.
74. Efimenko, K., et al., *Development and Testing of Hierarchically Wrinkled Coatings for Marine Antifouling*. ACS Appl. Mater. Interfaces, 2009. **1**(5): p. 1031-1040.
75. Huh, D., et al., *Tuneable elastomeric nanochannels for nanofluidic manipulation*. Nat. Mater., 2007. **6**(6): p. 424-428.
76. Yim, E.K.F., et al., *Nanopattern-induced changes in morphology and motility of smooth muscle cells*. Biomaterials, 2005. **26**(26): p. 5405-5413.
77. Hu, J., et al., *Enhanced Cell Adhesion and Alignment on Micro-Wavy Patterned Surfaces*. PLoS ONE, 2014. **9**(8): p. e104502.
78. Florijn, B., C. Coullais, and M. van Hecke, *Programmable Mechanical Metamaterials*. Physical Review Letters, 2014. **113**(17): p. 175503.

79. Tang, Y., et al., *Programmable Kiri-Kirigami Metamaterials*. *Advanced Materials*, 2017. **29**(10): p. 1604262.
80. Shan, S., et al., *Multistable Architected Materials for Trapping Elastic Strain Energy*. *Adv. Mater.*, 2015. **27**(29): p. 4296-4301.
81. Ni, X., *Activation of conductive pathways via deformation-induced instabilities*. 2014, Massachusetts Institute of Technology.
82. Han, Y., et al., *Geometric frustration in buckled colloidal monolayers*. *Nature*, 2008. **456**(7224): p. 898-903.
83. Yoon, H., et al., *Lateral Buckling of High Aspect Ratio Janus Nanowalls*. *Adv. Funct. Mater.*, 2012. **22**(17): p. 3723-3728.
84. Li, J., et al., *Transforming One-Dimensional Nanowalls to Long-Range Ordered Two-Dimensional Nanowaves: Exploiting Buckling Instability and Nanofibers Effect in Holographic Lithography*. *Advanced Functional Materials*, 2014. **24**(16): p. 2361-2366.
85. Singamaneni, S., M.E. McConney, and V.V. Tsukruk, *Swelling-Induced Folding in Confined Nanoscale Responsive Polymer Gels*. *ACS Nano*, 2010. **4**(4): p. 2327-2337.
86. Hauser, A.W., et al., *Photothermally Reprogrammable Buckling of Nanocomposite Gel Sheets*. *Angewandte Chemie International Edition*, 2015. **54**(18): p. 5434-5437.
87. Hirokawa, J., M. Ando, and N. Goto, *Waveguide-fed parallel plate slot array antenna*. *IEEE Transactions on Antennas and Propagation*, 1992. **40**(2): p. 218-223.
88. Linton, C.M. and D.V. Evans, *Acoustic scattering by an array of parallel plates*. *Wave Motion*, 1993. **18**(1): p. 51-65.
89. Liu, Y. and X. Zhang, *Metasurfaces for manipulating surface plasmons*. *Applied Physics Letters*, 2013. **103**(14): p. 141101.

90. Dejong, N.C. and A.M. Jacobi, *An experimental study of flow and heat transfer in parallel-plate arrays: local, row-by-row and surface average behavior*. International Journal of Heat and Mass Transfer, 1997. **40**(6): p. 1365-1378.
91. Wu, G., et al., *Directing the Deformation Paths of Soft Metamaterials with Prescribed Asymmetric Units*. Advanced Materials, 2015. **27**(17): p. 2747-2752.
92. Cao, B., et al., *Buckling into single-handed chiral structures from pH-sensitive hydrogel membranes*. Extreme Mech. Lett., 2016. **7**: p. 49–54.
93. Li, J., et al., *Transforming One-Dimensional Nanowalls to Long-Range Ordered Two-Dimensional Nanowaves: Exploiting Buckling Instability and Nanofibers Effect in Holographic Lithography*. Adv. Funct. Mater., 2014. **24**(16): p. 2361-2366.
94. Wu, G., Y. Xia, and S. Yang, *Buckling, symmetry breaking, and cavitation in periodically micro-structured hydrogel membranes*. Soft Matter, 2014. **10**(9): p. 1392-1399.
95. Guvendiren, M., S. Yang, and J.A. Burdick, *Swelling-Induced Surface Patterns in Hydrogels with Gradient Crosslinking Density*. Adv. Funct. Mater., 2009. **19**(19): p. 3038-3045.
96. Yazdchi, K. and A.R. Gowhari Anaraki, *Carrying capacity of edge-cracked columns under concentric vertical loads*. Acta Mechanica, 2008. **198**(1): p. 1-19.
97. Saif, M.T.A., *On a tunable bistable MEMS-theory and experiment*. Journal of Microelectromechanical Systems, 2000. **9**(2): p. 157-170.
98. Qiu, J., J.H. Lang, and A.H. Slocum. *A centrally-clamped parallel-beam bistable MEMS mechanism*. in *Technical Digest. MEMS 2001. 14th IEEE International Conference on Micro Electro Mechanical Systems (Cat. No.01CH37090)*. 2001.
99. Alizadeh, A., et al., *Dynamics of Ice Nucleation on Water Repellent Surfaces*. Langmuir, 2012. **28**(6): p. 3180-3186.

100. Thomas, A.V., et al., *Controlled Crumpling of Graphene Oxide Films for Tunable Optical Transmittance*. *Advanced Materials*, 2015. **27**(21): p. 3256-3265.
101. <http://www.eia.gov/outlooks/ieo/>.
102. Baetens, R., B.P. Jelle, and A. Gustavsen, *Properties, requirements and possibilities of smart windows for dynamic daylight and solar energy control in buildings: A state-of-the-art review*. *Solar Energy Materials and Solar Cells*, 2010. **94**(2): p. 87-105.
103. Azens, A. and C. Granqvist, *Electrochromic smart windows: energy efficiency and device aspects*. *Journal of Solid State Electrochemistry*, 2003. **7**(2): p. 64-68.
104. Granqvist, C.G., et al., *Progress in chromogenics: New results for electrochromic and thermochromic materials and devices*. *Solar Energy Materials and Solar Cells*, 2009. **93**(12): p. 2032-2039.
105. Kim, P., et al., *Rational Design of Mechano-Responsive Optical Materials by Fine Tuning the Evolution of Strain-Dependent Wrinkling Patterns*. *Advanced Optical Materials*, 2013. **1**(5): p. 381-388.
106. Zang, J., et al., *Multifunctionality and control of the crumpling and unfolding of large-area graphene*. *Nat Mater*, 2013. **12**(4): p. 321-325.
107. Yang, S., K. Khare, and P.-C. Lin, *Harnessing Surface Wrinkle Patterns in Soft Matter*. *Adv. Funct. Mater.*, 2010. **20**(16): p. 2550-2564.
108. Chan, E.P., et al., *Surface Wrinkles for Smart Adhesion*. *Adv. Mater.*, 2008. **20**(4): p. 711-716.
109. Chung, J.Y., J.P. Youngblood, and C.M. Stafford, *Anisotropic wetting on tunable micro-wrinkled surfaces*. *Soft Matter*, 2007. **3**(9): p. 1163-1169.
110. Lin, P.-C. and S. Yang, *Mechanically switchable wetting on wrinkled elastomers with dual-scale roughness*. *Soft Matter*, 2009. **5**(5): p. 1011-1018.

111. Rand, C.J. and A.J. Crosby, *Friction of soft elastomeric wrinkled surfaces*. Journal of Applied Physics, 2009. **106**(6): p. 064913-064913-4.
112. Efimenko, K., et al., *Development and Testing of Hierarchically Wrinkled Coatings for Marine Antifouling*. ACS Applied Materials & Interfaces, 2009. **1**(5): p. 1031-1040.
113. Vukusic, P., J.R. Sambles, and C.R. Lawrence, *Structural colour: Color mixing in wing scales of a butterfly*. Nature, 2000. **404**(6777): p. 457-457.
114. Zi, J., et al., *Coloration strategies in peacock feathers*. Proceedings of the National Academy of Sciences, 2003. **100**(22): p. 12576-12578.
115. Liu, K., X. Yao, and L. Jiang, *Recent developments in bio-inspired special wettability*. Chemical Society Reviews, 2010. **39**(8): p. 3240-3255.
116. Parker, A.R. and C.R. Lawrence, *Water capture by a desert beetle*. Nature, 2001. **414**(6859): p. 33-34.
117. Comanns, P., et al., *Moisture harvesting and water transport through specialized microstructures on the integument of lizards*. Beilstein Journal of Nanotechnology, 2011. **2**: p. 204-214.
118. Zheng, Y., et al., *Directional water collection on wetted spider silk*. Nature, 2010. **463**(7281): p. 640-643.
119. Daniel, S., M.K. Chaudhury, and J.C. Chen, *Fast Drop Movements Resulting from the Phase Change on a Gradient Surface*. Science, 2001. **291**(5504): p. 633.
120. Daniel, S., M.K. Chaudhury, and P.G. de Gennes, *Vibration-Actuated Drop Motion on Surfaces for Batch Microfluidic Processes*. Langmuir, 2005. **21**(9): p. 4240-4248.
121. Liu, G., et al., *Water Droplet Motion Control on Superhydrophobic Surfaces: Exploiting the Wenzel-to-Cassie Transition*. Langmuir, 2011. **27**(6): p. 2595-2600.

122. Cao, C., et al., *Harnessing Localized Ridges for High-Aspect-Ratio Hierarchical Patterns with Dynamic Tunability and Multifunctionality*. *Advanced Materials*, 2014. **26**(11): p. 1763-1770.
123. Lee, W.-K., et al., *Controlled Three-Dimensional Hierarchical Structuring by Memory-Based, Sequential Wrinkling*. *Nano Letters*, 2015. **15**(8): p. 5624-5629.
124. Li, Y., et al., *Superhydrophobic surfaces from hierarchically structured wrinkled polymers*. *ACS applied materials & interfaces*, 2013. **5**(21): p. 11066-11073.
125. Lee, W.-K., et al., *Stretchable Superhydrophobicity from Monolithic, Three-Dimensional Hierarchical Wrinkles*. *Nano Letters*, 2016. **16**(6): p. 3774-3779.
126. Feng, L., et al., *Super-Hydrophobic Surfaces: From Natural to Artificial*. *Advanced Materials*, 2002. **14**(24): p. 1857-1860.
127. Fang, Y., et al., *Hydrophobicity mechanism of non-smooth pattern on surface of butterfly wing*. *Chinese Science Bulletin*, 2007. **52**(5): p. 711-716.
128. Bhushan, B., *Adhesion of multi-level hierarchical attachment systems in gecko feet*. *Journal of Adhesion Science and Technology*, 2007. **21**(12-13): p. 1213-1258.
129. Chen, X. and J.W. Hutchinson, *Herringbone Buckling Patterns of Compressed Thin Films on Compliant Substrates*. *Journal of Applied Mechanics*, 2004. **71**(5): p. 597-603.
130. Zhang, P., et al., *Grooved Organogel Surfaces towards Anisotropic Sliding of Water Droplets*. *Advanced Materials*, 2014. **26**(19): p. 3131-3135.
131. De Gennes, P.G., F. Brochard-Wyart, and D. Quéré, *Capillarity and wetting phenomena*. 2004: Springer-Verlag New York.
132. Béfahy, S., et al., *Thickness and Elastic Modulus of Plasma Treated PDMS Silica-like Surface Layer*. *Langmuir*, 2010. **26**(5): p. 3372-3375.
133. Chiche, A., C.M. Stafford, and J.T. Cabral, *Complex micropatterning of periodic structures on elastomeric surfaces*. *Soft Matter*, 2008. **4**(12): p. 2360-2364.

134. Yang, X., et al., *Bioinspired Fabrication of Free-Standing Conducting Films with Hierarchical Surface Wrinkling Patterns*. ACS Nano, 2016. **10**(3): p. 3801-3808.
135. Johnston, I.D., et al., *Mechanical characterization of bulk Sylgard 184 for microfluidics and microengineering*. Journal of Micromechanics and Microengineering, 2014. **24**(3): p. 035017.
136. Bayley, F.A., et al., *Wavefront kinetics of plasma oxidation of polydimethylsiloxane: limits for sub- μ m wrinkling*. Soft Matter, 2014. **10**(8): p. 1155-1166.
137. Barthlott, W. and C. Neinhuis, *Purity of the sacred lotus, or escape from contamination in biological surfaces*. Planta, 1997. **202**(1): p. 1-8.
138. Autumn, K., et al., *Adhesive force of a single gecko foot-hair*. Nature, 2000. **405**(6787): p. 681-685.
139. Gu, Z.-Z., et al., *Structural Color and the Lotus Effect*. Angewandte Chemie International Edition, 2003. **42**(8): p. 894-897.
140. Koch, K., et al., *Fabrication of artificial Lotus leaves and significance of hierarchical structure for superhydrophobicity and low adhesion*. Soft Matter, 2009. **5**(7): p. 1386-1393.
141. Cortese, B., et al., *Superhydrophobicity due to the hierarchical scale roughness of PDMS surfaces*. Langmuir, 2008. **24**(6): p. 2712-2718.
142. Lee, Y., et al., *Fabrication of Hierarchical Structures on a Polymer Surface to Mimic Natural Superhydrophobic Surfaces*. Advanced Materials, 2007. **19**(17): p. 2330-2335.
143. Shirtcliffe, N.J., et al., *Dual-Scale Roughness Produces Unusually Water-Repellent Surfaces*. Advanced Materials, 2004. **16**(21): p. 1929-1932.
144. Li, Y., et al., *Superhydrophobic bionic surfaces with hierarchical microsphere/SWCNT composite arrays*. Langmuir, 2007. **23**(4): p. 2169-2174.

145. Yoo, P.J. and H.H. Lee, *Complex Pattern Formation by Adhesion-Controlled Anisotropic Wrinkling*. Langmuir, 2008. **24**(13): p. 6897-6902.
146. Kim, H.S. and A.J. Crosby, *Solvent-Responsive Surface via Wrinkling Instability*. Advanced Materials, 2011. **23**(36): p. 4188-4192.
147. Chan, E.P. and A.J. Crosby, *Fabricating Microlens Arrays by Surface Wrinkling*. Advanced Materials, 2006. **18**(24): p. 3238-3242.
148. Prathapan, R., et al., *Decreasing the Wettability of Cellulose Nanocrystal Surfaces Using Wrinkle-Based Alignment*. ACS Applied Materials & Interfaces, 2017. **9**(17): p. 15202-15211.
149. Yin, J., et al., *Deterministic Order in Surface Micro-Topologies through Sequential Wrinkling*. Advanced Materials, 2012. **24**(40): p. 5441-5446.
150. Lin, G., et al., *Self-similar Hierarchical Wrinkles as a Potential Multifunctional Smart Window with Simultaneously Tunable Transparency, Structural Color, and Droplet Transport*. ACS Applied Materials & Interfaces, 2017. **9**(31): p. 26510-26517.
151. Roth-Nebelsick, A., et al., *Leaf surface structures enable the endemic Namib desert grass Stipagrostis sabulicola to irrigate itself with fog water*. Journal of The Royal Society Interface, 2012. **9**(73): p. 1965.
152. Zheng, Y., X. Gao, and L. Jiang, *Directional adhesion of superhydrophobic butterfly wings*. Soft Matter, 2007. **3**(2): p. 178-182.
153. Morita, M., et al., *Macroscopic-wetting anisotropy on the line-patterned surface of fluoroalkylsilane monolayers*. Langmuir, 2005. **21**(3): p. 911-918.
154. Chen, F., et al., *Anisotropic wetting on microstrips surface fabricated by femtosecond laser*. Langmuir, 2010. **27**(1): p. 359-365.
155. Xia, D. and S.R.J. Brueck, *Strongly anisotropic wetting on one-dimensional nanopatterned surfaces*. Nano letters, 2008. **8**(9): p. 2819-2824.

156. Zhang, F. and H.Y. Low, *Anisotropic wettability on imprinted hierarchical structures*. Langmuir, 2007. **23**(14): p. 7793-7798.
157. Tie, L., Z. Guo, and W. Liu, *Anisotropic wetting properties on various shape of parallel grooved microstructure*. Journal of Colloid and Interface Science, 2015. **453**(Supplement C): p. 142-150.
158. Lee, S.G., et al., *Tunable anisotropic wettability of rice leaf-like wavy surfaces*. Advanced Functional Materials, 2013. **23**(5): p. 547-553.
159. Shao, Z.-C., et al., *Curvature induced hierarchical wrinkling patterns in soft bilayers*. Soft Matter, 2016. **12**(38): p. 7977-7982.
160. Zhang, Z., et al., *Strain-controlled switching of hierarchically wrinkled surfaces between superhydrophobicity and superhydrophilicity*. Langmuir, 2012. **28**(5): p. 2753-2760.
161. Bittoun, E. and A. Marmur, *The role of multiscale roughness in the lotus effect: is it essential for super-hydrophobicity?* Langmuir, 2012. **28**(39): p. 13933-13942.
162. Wilder, E.A., et al., *Measuring the Modulus of Soft Polymer Networks via a Buckling-Based Metrology*. Macromolecules, 2006. **39**(12): p. 4138-4143.
163. Zhao, Y., et al., *Anisotropic wetting characteristics on submicrometer-scale periodic grooved surface*. Langmuir, 2007. **23**(11): p. 6212-6217.
164. Lee, S.G., et al., *Tunable Anisotropic Wettability of Rice Leaf-Like Wavy Surfaces*. Advanced Functional Materials, 2013. **23**(5): p. 547-553.
165. Marmur, A., *Wetting on hydrophobic rough surfaces: to be heterogeneous or not to be?* Langmuir, 2003. **19**(20): p. 8343-8348.
166. Fürstner, R., et al., *Wetting and self-cleaning properties of artificial superhydrophobic surfaces*. Langmuir, 2005. **21**(3): p. 956-961.
167. Wenzel, R., *Resistance of solid surfaces to wetting by water*. Ind Eng Chem Res, 1936. **28**: p. 988-994.

168. Cassie, A.B.D., *Contact angles*. Discussions of the Faraday Society, 1948. **3**(0): p. 11-16.
169. Dettre, R.H. and R.E. Johnson, *Contact Angle Hysteresis*, in *Contact Angle, Wettability, and Adhesion*. 1964, AMERICAN CHEMICAL SOCIETY. p. 136-144.
170. Hillborg, H. and U.W. Gedde, *Hydrophobicity changes in silicone rubbers*. IEEE Transactions on Dielectrics and Electrical insulation, 1999. **6**(5): p. 703-717.
171. Hong, W., X. Zhao, and Z. Suo, *Formation of creases on the surfaces of elastomers and gels*. Applied Physics Letters, 2009. **95**(11): p. 111901.
172. Ben Amar, M. and P. Ciarletta, *Swelling instability of surface-attached gels as a model of soft tissue growth under geometric constraints*. Journal of the Mechanics and Physics of Solids, 2010. **58**(7): p. 935-954.
173. Ebata, Y., A.B. Croll, and A.J. Crosby, *Wrinkling and strain localizations in polymer thin films*. Soft Matter, 2012. **8**(35): p. 9086-9091.
174. Zang, J., et al., *Localized ridge wrinkling of stiff films on compliant substrates*. Journal of the Mechanics and Physics of Solids, 2012. **60**(7): p. 1265-1279.
175. Brau, F., et al., *Multiple-length-scale elastic instability mimics parametric resonance of nonlinear oscillators*. Nat Phys, 2011. **7**(1): p. 56-60.
176. Verho, T., et al., *Reversible switching between superhydrophobic states on a hierarchically structured surface*. Proceedings of the National Academy of Sciences, 2012. **109**(26): p. 10210-10213.
177. Long, J., et al., *Thermodynamic modeling of contact angles on rough, heterogeneous surfaces*. Advances in colloid and interface science, 2005. **118**(1): p. 173-190.
178. Koch, K., et al., *Surface microstructures of daisy florets (Asteraceae) and characterization of their anisotropic wetting*. Bioinspiration & Biomimetics, 2013. **8**(3): p. 036005.

179. Kubiak, K.J. and T.G. Mathia, *Anisotropic Wetting of Hydrophobic and Hydrophilic Surfaces—Modelling by Lattice Boltzmann Method*. Procedia Engineering, 2014. **79**(Supplement C): p. 45-48.
180. Rahmawan, Y., et al., *Wrinkled, dual-scale structures of diamond-like carbon (DLC) for superhydrophobicity*. Langmuir, 2009. **26**(1): p. 484-491.
181. Guadarrama-Cetina, J., et al., *Dew condensation on desert beetle skin*. Eur. Phys. J. E, 2014. **37**(11).
182. Zhai, L., et al., *Patterned superhydrophobic surfaces: Toward a synthetic mimic of the Namib Desert beetle*. Nano Lett., 2006. **6**(6): p. 1213-1217.
183. Dorrer, C. and J. R  he, *Mimicking the stenocara beetle-dewetting of drops from a patterned superhydrophobic surface*. Langmuir, 2008. **24**(12): p. 6154-6158.
184. Choi, J.H., et al., *Hydrophilic Dots on Hydrophobic Nanopatterned Surfaces as a Flexible Gas Barrier*. Langmuir, 2009. **25**(12): p. 7156-7160.
185. Garrod, R.P., et al., *Mimicking a stenocara beetle's back for microcondensation using plasmachemical patterned superhydrophobic-superhydrophilic surfaces*. Langmuir, 2007. **23**(2): p. 689-693.
186. Lee, A., et al., *Water harvest via dewing*. Langmuir, 2012. **28**(27): p. 10183-10191.
187. Her, E.K., et al., *Bioinspired steel surfaces with extreme wettability contrast*. Nanoscale, 2012. **4**(9): p. 2900-2905.
188. Lai, Y.K., et al., *Bioinspired Patterning with Extreme Wettability Contrast on TiO₂ Nanotube Array Surface: A Versatile Platform for Biomedical Applications*. Small, 2013. **9**(17): p. 2945-2953.
189. Bai, H., et al., *Efficient Water Collection on Integrative Bioinspired Surfaces with Star-Shaped Wettability Patterns*. Adv. Mater., 2014. **26**(29): p. 5025-5030.

190. Choo, S., H.J. Choi, and H. Lee, *Water-collecting behavior of nanostructured surfaces with special wettability*. Applied Surface Science, 2015. **324**: p. 563-568.
191. Narhe, R.D. and D.A. Beysens, *Water condensation on a super-hydrophobic spike surface*. EPL (Europhysics Letters), 2006. **75**(1): p. 98.
192. Rykaczewski, K. and J.H.J. Scott, *Methodology for Imaging Nano-to-Microscale Water Condensation Dynamics on Complex Nanostructures*. ACS Nano, 2011. **5**(7): p. 5962-5968.
193. Chen, X., et al., *Nanograssed Micropyramidal Architectures for Continuous Dropwise Condensation*. Advanced Functional Materials, 2011. **21**(24): p. 4617-4623.
194. Schweikart, A., et al., *Nanoparticle assembly by confinement in wrinkles: experiment and simulations*. Soft Matter, 2010. **6**(23): p. 5860-5863.
195. Xiu, Y., et al., *Biomimetic Creation of Hierarchical Surface Structures by Combining Colloidal Self-Assembly and Au Sputter Deposition*. Langmuir, 2006. **22**(23): p. 9676-9681.

APPENDIX A:

MATLAB CODE FOR PERIODIC BOUNDARY CONDITION

```
function PBC_3D_XY_Yesedge_for_wrinkling(fname ,fnnew)
% example: (original file loc, new file loc, part name)
% ('I:\AbaqusTemp\frommodel.inp', 'E:\ Ash\ Abaqus
\pbc\ input .inp ')
% Open file for reading
part='part -1-1';
fid1=fopen(fname ,'r'); % input
fid =fopen(fnnew ,'wt'); % output
if (fid1 < 0)
    error('could not open file %s',fname );
end
% Find the end of header
key = '*Node ';
while 1
    readin = fgetl(fid1 );
    len = length(readin );
    if len ~=5
        fprintf(fid ,readin ); %copy this to new file
        fprintf(fid ,'\n'); %copy this to new file
    elseif and(readin(len )== key(len),len ==5)
        break
    end
end
% Store nodes and their positions
data =
textscan(fid1 ,'%d %f %f %f','delimiter',' ','bufSize',
265000000);
node=double(data {1 ,1});
xpos=data {1 ,2};
sortrows(xpos);
ypos=data {1 ,3};
sortrows(ypos);
zpos=data {1 ,4};
sortrows(zpos);
Allnodes=[node,xpos,ypos,zpos];
% Find maximum dimensions of prism
xmax=max(xpos );
xmin=min(xpos );
ymax=max(ypos );
```

```

ymin=min(ypos );
zmax=max(zpos );
zmin=min(zpos );
% The following procedures sort through the node sets
% to select nodes that are found on faces, edges, and
% corners
%B--back,b--bottom
% Define the face nodes
left=Allnodes(Allnodes(:,2)==xmin&Allnodes(:,3)~=ymax&A
llnodes(:,3)~=ymin&Allnodes(:,4)~=zmax&Allnodes(:,4)~=z
min,:);
left=sortrows(left,[3,4]);
right=Allnodes(Allnodes(:,2)==xmax&Allnodes(:,3)~=ymax&
Allnodes(:,3)~=ymin&Allnodes(:,4)~=zmax&Allnodes(:,4)~=
zmin,:);
right=sortrows(right,[3,4]);
front=Allnodes(Allnodes(:,2)~=xmin&Allnodes(:,2)~=xmax&
Allnodes(:,3)==ymin&Allnodes(:,4)~=zmax&Allnodes(:,4)~=
zmin,:);
front=sortrows(front,[2,4]);
back=Allnodes(Allnodes(:,2)~=xmin&Allnodes(:,2)~=xmax&A
llnodes(:,3)==ymax&Allnodes(:,4)~=zmax&Allnodes(:,4)~=z
min,:);
back=sortrows(back,[2,4]);
top=Allnodes(Allnodes(:,2)~=xmin&Allnodes(:,2)~=xmax&A
llnodes(:,3)~=ymax&Allnodes(:,3)~=ymin&Allnodes(:,4)==zm
ax,:);
top=sortrows(top,[2,3]);
bottom=Allnodes(Allnodes(:,2)~=xmin&Allnodes(:,2)~=xmax
&Allnodes(:,3)~=ymax&Allnodes(:,3)~=ymin&Allnodes(:,4)=
=zmin,:);
bottom=sortrows(bottom,[2,3]);
%Define edge nodes
FL=Allnodes(Allnodes(:,2)==xmin&Allnodes(:,3)==ymin&All
nodes(:,4)~=zmax&Allnodes(:,4)~=zmin,:);
FL=sortrows(FL,4);
FR=Allnodes(Allnodes(:,2)==xmax&Allnodes(:,3)==ymin&All
nodes(:,4)~=zmax&Allnodes(:,4)~=zmin,:);
FR=sortrows(FR,4);
BL=Allnodes(Allnodes(:,2)==xmin&Allnodes(:,3)==ymax&All
nodes(:,4)~=zmax&Allnodes(:,4)~=zmin,:);
BL=sortrows(BL,4);

```

```

BR=Allnodes (Allnodes (:,2)==xmax&Allnodes (:,3)==ymax&All
nodes (:,4)~=zmax&Allnodes (:,4)~=zmin,:);
BR=sortrows (BR,4);
%
BT=Allnodes (Allnodes (:,2)~=xmin&Allnodes (:,2)~=xmax&All
nodes (:,3)==ymax&Allnodes (:,4)==zmax,:);
BT=sortrows (BT,2);
FT=Allnodes (Allnodes (:,2)~=xmin&Allnodes (:,2)~=xmax&All
nodes (:,3)==ymin&Allnodes (:,4)==zmax,:);
FT=sortrows (FT,2);
Bb=Allnodes (Allnodes (:,2)~=xmin&Allnodes (:,2)~=xmax&All
nodes (:,3)==ymax&Allnodes (:,4)==zmin,:);
Bb=sortrows (Bb,2);
Fb=Allnodes (Allnodes (:,2)~=xmin&Allnodes (:,2)~=xmax&All
nodes (:,3)==ymin&Allnodes (:,4)==zmin,:);
Fb=sortrows (Fb,2);
%
LT=Allnodes (Allnodes (:,2)==xmin&Allnodes (:,3)~=ymax&All
nodes (:,3)~=ymin&Allnodes (:,4)==zmax,:);
LT=sortrows (LT,3);
RT=Allnodes (Allnodes (:,2)==xmax&Allnodes (:,3)~=ymax&All
nodes (:,3)~=ymin&Allnodes (:,4)==zmax,:);
RT=sortrows (RT,3);
Lb=Allnodes (Allnodes (:,2)==xmin&Allnodes (:,3)~=ymax&All
nodes (:,3)~=ymin&Allnodes (:,4)==zmin,:);
Lb=sortrows (Lb,3);
Rb=Allnodes (Allnodes (:,2)==xmax&Allnodes (:,3)~=ymax&All
nodes (:,3)~=ymin&Allnodes (:,4)==zmin,:);
Rb=sortrows (Rb,3);
%Define corners
BLT=Allnodes (Allnodes (:,2)==xmin&Allnodes (:,3)==ymax&Al
lnodes (:,4)==zmax,:);
BRT=Allnodes (Allnodes (:,2)==xmax&Allnodes (:,3)==ymax&Al
lnodes (:,4)==zmax,:);
FLT=Allnodes (Allnodes (:,2)==xmin&Allnodes (:,3)==ymin&Al
lnodes (:,4)==zmax,:);
FRT=Allnodes (Allnodes (:,2)==xmax&Allnodes (:,3)==ymin&Al
lnodes (:,4)==zmax,:);
BLb=Allnodes (Allnodes (:,2)==xmin&Allnodes (:,3)==ymax&Al
lnodes (:,4)==zmin,:);
BRb=Allnodes (Allnodes (:,2)==xmax&Allnodes (:,3)==ymax&Al
lnodes (:,4)==zmin,:);

```

```

FLb=Allnodes (Allnodes (:,2)==xmin&Allnodes (:,3)==ymin&Al
lnodes (:,4)==zmin,:);
FRb=Allnodes (Allnodes (:,2)==xmax&Allnodes (:,3)==ymin&Al
lnodes (:,4)==zmin,:);
%to find *end instance
while 1
readin = fgetl(fid1 );
len = length(readin );
if and(readin(len)=='e',len==13)
fprintf(fid ,readin ); %copy this to new file
fprintf(fid ,'\n'); %copy this to new file
break
end
end
%write faces
fprintf(fid , '*Node , nset=FakeDefNodes \n');
fprintf(fid , '100000, 0., 0. \n');
fprintf(fid , '*Nset , nset=left , instance
= %s ,unsorted\n ',part );
n=0;
for k=1: length(left(:,1))
    if n==14
        fprintf(fid,'%d\n',left(k));
        n=0;
    else
        fprintf(fid , '%d , ',left(k));
        n=n+1;
    end
end
fprintf(fid,'\n');
fprintf(fid , '*Nset , nset=right , instance
= %s ,unsorted \n ',part );
n=0;
for k=1: length(right(:,1))
    if n==14
        fprintf(fid , '%d\n ',right(k));
        n=0;
    else
        fprintf(fid , '%d, ',right(k));
        n=n+1;
    end
end
end
end

```

```

fprintf(fid, '\n');
fprintf(fid, '*Nset , nset=back , instance
= %s,unsorted \n',part );
n=0;
for k=1: length(back(:,1))
    if n==14
        fprintf(fid, '%d\n',back(k));
        n=0;
    else
        fprintf(fid, '%d , ',back(k));
        n=n+1;
    end
end
fprintf(fid, '\n');
fprintf(fid, '*Nset , nset=front , instance
= %s,unsorted \n',part );
n=0;
for k=1: length(front(:,1))
    if n==14
        fprintf(fid, '%d\n',front(k));
        n=0;
    else
        fprintf(fid, '%d , ',front(k));
        n=n+1;
    end
end
fprintf(fid, '\n');
fprintf(fid, '*Nset , nset=top , instance = %s,unsorted
\n',part );
n=0;
for k=1: length(top(:,1))
    if n==14
        fprintf(fid, '%d\n ',top(k));
        n=0;
    else
        fprintf(fid, '%d , ',top(k));
        n=n+1;
    end
end
fprintf(fid, '\n');
fprintf(fid, '*Nset , nset=bottom , instance
= %s,unsorted \n',part );

```

```

n=0;
for k=1: length(bottom(:,1))
if n==14
    fprintf(fid , '%d\n ',bottom(k));
    n=0;
else
    fprintf(fid , '%d, ',bottom(k));
    n=n+1;
end
end
fprintf(fid, '\n');
%write edges
fprintf(fid , '*Nset , nset=BL , instance
= %s ,unsorted\n',part );
n=0;
for k=1: length(BL(:,1))
if n==14
    fprintf(fid , '%d\n ',BL(k));
    n=0;
else
    fprintf(fid , '%d, ',BL(k));
    n=n+1;
end
end
fprintf(fid, '\n');
fprintf(fid , '*Nset , nset=BR , instance = %s,unsorted
\n',part );
n=0;
for k=1: length(BR(:,1))
if n==14
    fprintf(fid , '%d\n ',BR(k));
    n=0;
else
    fprintf(fid , '%d, ',BR(k));
    n=n+1;
end
end
fprintf(fid, '\n');
fprintf(fid , '*Nset , nset=FR , instance = %s,unsorted
\n',part );
n=0;
for k=1: length(FR(:,1))

```

```

if n==14
    fprintf(fid , '%d\n ',FR(k));
    n=0;
else
    fprintf(fid , '%d, ',FR(k));
    n=n+1;
end
end
fprintf(fid, '\n');
fprintf(fid , '*Nset , nset=FL , instance = %s,unsorted
\n',part );
n=0;
for k=1: length(FL(:,1))
if n==14
    fprintf(fid , '%d\n ',FL(k));
    n=0;
else
    fprintf(fid , '%d, ',FL(k));
    n=n+1;
end
end
fprintf(fid, '\n');
fprintf(fid , '*Nset , nset=BT , instance = %s,unsorted
\n',part );
n=0;
for k=1: length(BT(:,1))
if n==14
    fprintf(fid , '%d\n ',BT(k));
    n=0;
else
    fprintf(fid , '%d, ',BT(k));
    n=n+1;
end
end
fprintf(fid, '\n');
fprintf(fid , '*Nset , nset=FT , instance = %s,unsorted
\n',part );
n=0;
for k=1: length(FT(:,1))
if n==14
    fprintf(fid , '%d\n ',FT(k));
    n=0;

```

```

else
    fprintf(fid , '%d, ', FT(k));
    n=n+1;
end
end
fprintf(fid, '\n');
fprintf(fid , '*Nset , nset=RT , instance = %s,unsorted
\n',part );
n=0;
for k=1: length(RT(:,1))
if n==14
    fprintf(fid , '%d\n ', RT(k));
    n=0;
else
    fprintf(fid , '%d, ', RT(k));
    n=n+1;
end
end
fprintf(fid, '\n');
fprintf(fid , '*Nset , nset=LT , instance = %s,unsorted
\n',part );
n=0;
for k=1: length(LT(:,1))
if n==14
    fprintf(fid , '%d\n ', LT(k));
    n=0;
else
    fprintf(fid , '%d, ', LT(k));
    n=n+1;
end
end
fprintf(fid, '\n');
fprintf(fid , '*Nset , nset=Fb , instance = %s,unsorted
\n',part );
n=0;
for k=1: length(Fb(:,1))
if n==14
    fprintf(fid , '%d\n ', Fb(k));
    n=0;
else
    fprintf(fid , '%d, ', Fb(k));
    n=n+1;
end
end

```

```

end
end
fprintf(fid, '\n');
fprintf(fid, '*Nset , nset=Bb , instance = %s,unsorted
\n',part );
n=0;
for k=1: length(Bb(:,1))
if n==14
    fprintf(fid, '%d\n ',Bb(k));
    n=0;
else
    fprintf(fid, '%d, ',Bb(k));
    n=n+1;
end
end
fprintf(fid, '\n');
fprintf(fid, '*Nset , nset=Lb , instance = %s,unsorted
\n',part );
n=0;
for k=1: length(Lb(:,1))
if n==14
    fprintf(fid, '%d\n ',Lb(k));
    n=0;
else
    fprintf(fid, '%d, ',Lb(k));
    n=n+1;
end
end
fprintf(fid, '\n');
fprintf(fid, '*Nset , nset=Rb , instance = %s,unsorted
\n',part );
n=0;
for k=1: length(Rb(:,1))
if n==14
    fprintf(fid, '%d\n ',Rb(k));
    n=0;
else
    fprintf(fid, '%d, ',Rb(k));
    n=n+1;
end
end
end
fprintf(fid, '\n');

```

```

%write corners
fprintf(fid , '*Nset , nset=BLT , instance
= %s ,unsorted\n',part );
for k=1: length(BLT(:,1))
fprintf(fid , '%d , ',BLT(k));
end
fprintf(fid,'\n');
fprintf(fid , '*Nset , nset=BRT , instance = %s,unsorted
\n',part );
for k=1: length(BRT(:,1))
fprintf(fid , '%d , ',BRT(k));
end
fprintf(fid,'\n');
fprintf(fid , '*Nset , nset=FRT , instance = %s,unsorted
\n',part );
for k=1: length(FRT(:,1))
fprintf(fid , '%d , ',FRT(k));
end
fprintf(fid,'\n');
fprintf(fid , '*Nset , nset=FLT , instance = %s,unsorted
\n',part );
for k=1: length(FLT(:,1))
fprintf(fid , '%d , ',FLT(k));
end
fprintf(fid,'\n');
fprintf(fid , '*Nset , nset=BLb , instance
= %s ,unsorted\n',part );
for k=1: length(BLb(:,1))
fprintf(fid , '%d , ',BLb(k));
end
fprintf(fid,'\n');
fprintf(fid , '*Nset , nset=BRb , instance = %s,unsorted
\n',part );
for k=1: length(BRb(:,1))
fprintf(fid , '%d , ',BRb(k));
end
fprintf(fid,'\n');
fprintf(fid , '*Nset , nset=FRb , instance = %s,unsorted
\n',part );
for k=1: length(FRb(:,1))
fprintf(fid , '%d , ',FRb(k));
end

```

```

fprintf(fid, '\n');
fprintf(fid, '*Nset , nset=FLb , instance = %s,unsorted
\n',part );
for k=1: length(FLb(:,1))
fprintf(fid, '%d , ',FLb(k));
end
fprintf(fid, '\n');

%equation
fprintf(fid, '*Equation\n');
fprintf(fid, '3\n');
fprintf(fid, 'right,1,1\n');
fprintf(fid, 'left,1,-1\n');
fprintf(fid, '100000,1,-1\n');
fprintf(fid, '2\n');
fprintf(fid, 'right,2,1\n');
fprintf(fid, 'left,2,-1\n');
fprintf(fid, '2\n');
fprintf(fid, 'right,3,1\n');
fprintf(fid, 'left,3,-1\n');
fprintf(fid, '2\n');
fprintf(fid, 'back,1,1\n');
fprintf(fid, 'front,1,-1\n');
fprintf(fid, '3\n');
fprintf(fid, 'back,2,1\n');
fprintf(fid, 'front,2,-1\n');
fprintf(fid, '100000,2,-1\n');
fprintf(fid, '2\n');
fprintf(fid, 'back,3,1\n');
fprintf(fid, 'front,3,-1\n');
%
fprintf(fid, '2\n');
fprintf(fid, 'BL,1,1\n');
fprintf(fid, 'FL,1,-1\n');
fprintf(fid, '3\n');
fprintf(fid, 'BL,2,1\n');
fprintf(fid, 'FL,2,-1\n');
fprintf(fid, '100000,2,-1\n');
fprintf(fid, '2\n');
fprintf(fid, 'BL,3,1\n');
fprintf(fid, 'FL,3,-1\n');
fprintf(fid, '2\n');

```

```

fprintf(fid, 'FR,2,1\n');
fprintf(fid, 'FL,2,-1\n');
fprintf(fid, '2\n');
fprintf(fid, 'FR,3,1\n');
fprintf(fid, 'FL,3,-1\n');
fprintf(fid, '3\n');
fprintf(fid, 'FR,1,1\n');
fprintf(fid, 'FL,1,-1\n');
fprintf(fid, '100000,1,-1\n');
fprintf(fid, '3\n');
fprintf(fid, 'BR,1,1\n');
fprintf(fid, 'FL,1,-1\n');
fprintf(fid, '100000,1,-1\n');
fprintf(fid, '3\n');
fprintf(fid, 'BR,2,1\n');
fprintf(fid, 'FL,2,-1\n');
fprintf(fid, '100000,2,-1\n');
fprintf(fid, '2\n');
fprintf(fid, 'BR,3,1\n');
fprintf(fid, 'FL,3,-1\n');
%
fprintf(fid, '2\n');
fprintf(fid, 'BT,1,1\n');
fprintf(fid, 'FT,1,-1\n');
fprintf(fid, '3\n');
fprintf(fid, 'BT,2,1\n');
fprintf(fid, 'FT,2,-1\n');
fprintf(fid, '100000,2,-1\n');
fprintf(fid, '2\n');
fprintf(fid, 'BT,3,1\n');
fprintf(fid, 'FT,3,-1\n');
fprintf(fid, '3\n');
fprintf(fid, 'RT,1,1\n');
fprintf(fid, 'LT,1,-1\n');
fprintf(fid, '100000,1,-1\n');
fprintf(fid, '2\n');
fprintf(fid, 'RT,2,1\n');
fprintf(fid, 'LT,2,-1\n');
fprintf(fid, '2\n');
fprintf(fid, 'RT,3,1\n');
fprintf(fid, 'LT,3,-1\n');
%
```

```

fprintf(fid, '3\n');
fprintf(fid, 'Rb,1,1\n');
fprintf(fid, 'Lb,1,-1\n');
fprintf(fid, '100000,1,-1\n');
fprintf(fid, '2\n');
fprintf(fid, 'Rb,2,1\n');
fprintf(fid, 'Lb,2,-1\n');
fprintf(fid, '2\n');
fprintf(fid, 'Rb,3,1\n');
fprintf(fid, 'Lb,3,-1\n');
fprintf(fid, '2\n');
fprintf(fid, 'Bb,1,1\n');
fprintf(fid, 'Fb,1,-1\n');
fprintf(fid, '3\n');
fprintf(fid, 'Bb,2,1\n');
fprintf(fid, 'Fb,2,-1\n');
fprintf(fid, '100000,2,-1\n');
fprintf(fid, '2\n');
fprintf(fid, 'Bb,3,1\n');
fprintf(fid, 'Fb,3,-1\n');

fprintf(fid, '2\n');
fprintf(fid, 'BLb,1,1\n');
fprintf(fid, 'FLb,1,-1\n');
fprintf(fid, '3\n');
fprintf(fid, 'BLb,2,1\n');
fprintf(fid, 'FLb,2,-1\n');
fprintf(fid, '100000,2,-1\n');
fprintf(fid, '2\n');
fprintf(fid, 'BLb,3,1\n');
fprintf(fid, 'FLb,3,-1\n');
fprintf(fid, '3\n');
fprintf(fid, 'FRb,1,1\n');
fprintf(fid, 'FLb,1,-1\n');
fprintf(fid, '100000,1,-1\n');
fprintf(fid, '2\n');
fprintf(fid, 'FRb,2,1\n');
fprintf(fid, 'FLb,2,-1\n');
fprintf(fid, '2\n');
fprintf(fid, 'FRb,3,1\n');
fprintf(fid, 'FLb,3,-1\n');
fprintf(fid, '3\n');

```

```

fprintf(fid, 'BRb,1,1\n');
fprintf(fid, 'FLb,1,-1\n');
fprintf(fid, '100000,1,-1\n');
fprintf(fid, '3\n');
fprintf(fid, 'BRb,2,1\n');
fprintf(fid, 'FLb,2,-1\n');
fprintf(fid, '100000,2,-1\n');
fprintf(fid, '2\n');
fprintf(fid, 'BRb,3,1\n');
fprintf(fid, 'FLb,3,-1\n');
%
%
fprintf(fid, '2\n');
fprintf(fid, 'BLT,1,1\n');
fprintf(fid, 'FLT,1,-1\n');
fprintf(fid, '3\n');
fprintf(fid, 'BLT,2,1\n');
fprintf(fid, 'FLT,2,-1\n');
fprintf(fid, '100000,2,-1\n');
fprintf(fid, '2\n');
fprintf(fid, 'BLT,3,1\n');
fprintf(fid, 'FLT,3,-1\n');
fprintf(fid, '3\n');
fprintf(fid, 'FRT,1,1\n');
fprintf(fid, 'FLT,1,-1\n');
fprintf(fid, '100000,1,-1\n');
fprintf(fid, '2\n');
fprintf(fid, 'FRT,2,1\n');
fprintf(fid, 'FLT,2,-1\n');
fprintf(fid, '2\n');
fprintf(fid, 'FRT,3,1\n');
fprintf(fid, 'FLT,3,-1\n');
fprintf(fid, '3\n');
fprintf(fid, 'BRT,1,1\n');
fprintf(fid, 'FLT,1,-1\n');
fprintf(fid, '100000,1,-1\n');
fprintf(fid, '3\n');
fprintf(fid, 'BRT,2,1\n');
fprintf(fid, 'FLT,2,-1\n');
fprintf(fid, '100000,2,-1\n');
fprintf(fid, '2\n');
fprintf(fid, 'BRT,3,1\n');

```

```

fprintf(fid, 'FLT,3,-1\n');

fprintf(fid, '2\n');
fprintf(fid, 'BT,4,1\n');
fprintf(fid, 'FT,4,-1\n');
fprintf(fid, '2\n');
fprintf(fid, 'RT,5,1\n');
fprintf(fid, 'LT,5,-1\n');
fprintf(fid, '2\n');
fprintf(fid, 'FRT,4,1\n');
fprintf(fid, 'FLT,4,-1\n');
fprintf(fid, '2\n');
fprintf(fid, 'FRT,5,1\n');
fprintf(fid, 'FLT,5,-1\n');
fprintf(fid, '2\n');
fprintf(fid, 'BLT,4,1\n');
fprintf(fid, 'FLT,4,-1\n');
fprintf(fid, '2\n');
fprintf(fid, 'BLT,5,1\n');
fprintf(fid, 'FLT,5,-1\n');
fprintf(fid, '2\n');
fprintf(fid, 'BRT,4,1\n');
fprintf(fid, 'FLT,4,-1\n');
fprintf(fid, '2\n');
fprintf(fid, 'BRT,5,1\n');
fprintf(fid, 'FLT,5,-1\n');

fclose(fid1 );
fclose(fid);
disp('complete')
end

```

APPENDIX B:

MATLAB CODE FOR CALCULATING GIBSON FREE ENERGY OF A WATER DROPLET ON HIERARCHICAL WRINKLING SURFACE

```
clear;
clc;
%In this code complex version hierarchical equation is
used for both fsl and fl
% unit:um
A_l=24.8;
lambda_l=24.8;
A_s=0;
lambda_s=0.8;
%notice lambda_l has to be integer times of lambda_s
pi=3.1416;
[h,theta] = meshgrid(0.8:-
0.05:0.05,90/180*pi:10*pi/180:170/180*pi);
[m,n]=size(h);
fl=zeros(size(h));
fsl=zeros(size(h));
l1l=@(tt)sqrt((1-
4*A_s*(pi^2)/lambda_s.*cos((2*pi/lambda_s*tt)-
pi/2)*A_l.*cos((2*pi/lambda_l*tt)-
pi/2)/lambda_l.*(1+4*A_l^2*(pi^2)/(lambda_l^2)).*cos((2*
pi/lambda_l*tt)-pi/2).^2).^(-1/2)...
+4*A_s*sin((2*pi/lambda_s*tt)-
pi/2)*A_l*(pi^2)/(lambda_l^2).*sin((2*pi/lambda_l*tt)-
pi/2).*(1+4*A_l^2*(pi^2)/(lambda_l^2)).*cos((2*pi/lambda
_l*tt)-pi/2).^2).^(-1/2)...
-16*A_s*sin((2*pi/lambda_s*tt)-
pi/2)*A_l^3*(pi^4).*cos((2*pi/lambda_l*tt)-
pi/2).^2/(lambda_l^4).*(1+4*A_l^2*(pi^2)/(lambda_l^2)).*
cos((2*pi/lambda_l*tt)-pi/2).^2).^(-
3/2).*sin((2*pi/lambda_l*tt)-pi/2)).^2....
+(2*A_l*pi/lambda_l.*cos((2*pi/lambda_l*tt)-pi/2)...
+2*A_s*pi/lambda_s.*cos((2*pi/lambda_s*tt)-
pi/2).*(1+4*A_l^2*(pi^2)/(lambda_l^2)).*cos((2*pi/lambda
_l*tt)-pi/2).^2).^(-1/2)...
+8*A_s.*sin((2*pi/lambda_s*tt)-
pi/2).*(1+4*A_l^2*(pi^2)/(lambda_l^2)).*cos((2*pi/lambda
_l*tt)-pi/2).^2).^(-3/2)*A_l^2
```

```

*(pi^3)/(lambda_1^3).*cos((2*pi/lambda_1*tt)-
pi/2).*sin((2*pi/lambda_1*tt)-pi/2)).^2);
for i=1:1:m
    for j=1:1:n
        [i j]
t=findallzeros(@shape_2,[0
lambda_1],h(i,j),A_1,A_s,lambda_1,lambda_s);
t=sort(t);
a=t-A_s*sin(2*pi/lambda_s*t-
pi/2)*A_1*2*pi/lambda_1.*cos(2*pi/lambda_1*t-pi/2)...
./sqrt(1+(A_1*2*pi/lambda_1*cos(2*pi/lambda_1*t-
pi/2)).^2);
a1=[0 a];
a2=[a lambda_1];
a3=a2-a1;
a4=a3(1:2:end);
f1(i,j)= sum(a4)/lambda_1;
line=0;
t1=t(1:2:end);
t2=t(2:2:end);
if length(t1)~=length(t2)
    disp('error:length(t1)~=length(t2)');
    fsl(i,j)=0;
else
for k=1:1:length(t1)
    line1=integral(@(tt) lll(tt),t1(k),t2(k));
    line=line+line1;
end
fsl(i,j)=line/lambda_1;
end
    end
end
% %cal G
% for thetay=80/180*3.14:10/180*3.14:120/180*3.14
thetay=86/180*3.14;
omega=fsl*cos(thetay)-f1;
% F=1./(2*theta-sin(2*theta));
% G=sqrt(F).*(theta-omega.*sin(theta));
F=(2-3*cos(theta)+(cos(theta)).^3).^(-2/3);
G=F.*(2-2*cos(theta)-omega.*(sin(theta)).^2);
% plot(h,G)
% hold all

```

```

% end
surf(h,theta/3.14*180,G,'EdgeColor','none','LineStyle',
'none')
xlabel('h');
% ylabel('theta');
ylabel('G');
% zlabel('G');

function x =
findallzeros( fhandle,interval,h,A_l,A_s,lambda_l,lambda_
a_s)
%
%  attempts to find multiple roots of a function.
%
%  fhandle = function handle, prefix by @

    x = [ ] ;
    xguess=min(interval);
    xend=max(interval);
    while xguess<xend
        if
abs(feval(fhandle,xguess,[ ],h,A_l,A_s,lambda_l,lambda_
s))<=1e-16,
            xroot=xguess;
        else
            [xroot,val,flag] =
fzero(fhandle,xguess,[ ],x,h,A_l,A_s,lambda_l,lambda_s);
            if flag <= 0
                return
            end
        end
        if xroot>=min(interval)&&xroot<=max(interval)
            x=[x,xroot];
        end
        xguess=xguess+0.1;
    end
end

```